SAND2005-5940
Unlimited Release
Printed September 2005

Computational modeling of fracture and fragmentation in geomaterials

R.A. Regueiro[§¶] A.F. Fossum[†] R.P. Jensen[†]
C.D. Foster[‡] M.T. Manzari[*] R.I. Borja[‡]

Abstract

Modeling fracture and fragmentation in geomaterials due to various loading and environmental conditions is a challenging problem and requires the latest in experimental, constitutive modeling, and computational solution method technology. At Sandia, current geomaterial constitutive models and computational methods are incapable of predictively modeling the transition of continuous rock-like material to fragmented rock material within the context of coupled solid-fluid-mechanical physics. To address this need, we proposed to develop a physically-based geomaterial constitutive model and computational method that can predictively model this transition.

Two problems that would be better understood with such a modeling capability are the defeat of Hard and Deeply Buried Targets (HDBT) and the long term performance of deep geologic nuclear waste repositories. It would be useful to be able to predict the behavior of these buried structures when subjected to extreme dynamic loading conditions such as high velocity penetration events, explosive blasts, or seismic events. At present, the mechanics of rock penetration are poorly understood, and there are no empirical data that can be used to forecast long term performance (over 1000s of years) of deep geologic nuclear waste repositories. With the computational analysis tool developed by this and future projects to evaluate potential failure scenarios of nuclear waste repositories, the Department of Energy's (DOE's) efforts to obtain Nuclear Regulatory Commission (NRC) approval could become easier. In addition to modeling the defeat of HDBT and the long term performance of nuclear waste repositories, the resulting computational analysis tool will be useful for modeling fracture and fragmentation in geomaterials such as concrete, rock, frozen soil, and heavily overconsolidated clay encountered in foundation construction and performance, tunneling construction, oil and natural gas production, and depleted reservoirs used for subsurface sequestration of greenhouse gases.

Keywords: constitutive modeling; geomaterials; failure mechanics; embedded discontinuity; cohesive surface model; coupled DEM/FEM.

¶Science-Based Materials Modeling Department
Sandia National Laboratories
P.O. Box 969
Livermore, CA 94551

†Geomechanics Department
Sandia National Laboratories
P.O. Box 5800
Albuquerque, NM 87158

‡Department of Civil and Environmental Engineering
Stanford University
Terman Engineering Center M42
Stanford, California 94305-4020

*Department of Civil and Environmental Engineering
George Washington University
801 22nd Street, NW
Washington, DC 20052

§Department of Civil, Environmental, and Architectural Engineering
University of Colorado at Boulder
1111 Engineering Dr.
428 UCB, ECOT 441
Boulder, CO 80309-0428

Contents

List of Figures

Chapter 1

Introduction

Authors: R.A. Regueiro, A.F. Fossum, R.P. Jensen

As a means of introduction, we provide an overview of the type of problem we are attempting to solve, our approach to solving it, what we have achieved so far, what research is ongoing, and what we determined during the project must be left for future work. All finite element implementations have been carried out and are continuing to be developed in the open-source, C++ software program Tahoe (tahoe.ca.sandia.gov), while all discrete element implementations have been carried out in the Distinct Motion Code (DMC) developed at Sandia [46].

1.1 Type of problem to solve

To destroy a hard underground structure such as a tunnel or cave, an explosive must be detonated beneath the ground surface with sufficient depth that the ensuing shock waves travel through inhomogeneous and often anisotropic earth materials (that are fully or partially saturated with fluid) to reach the target with sufficient amplitude to defeat it (cf. Fig.1.1). Analyzing such an event requires the ability to predict a projectile's penetration depth, the shock wave propagation, and the shock-structure interaction once the shock wave reaches the target. The solution of such a problem requires high performance computing (HPC), state-of-the-art geomaterial models, coupled solid-fluid-mechanical governing equations, the ability to model continua and discontinua, critical damage criteria, and a knowledge of the in-situ statistical geomaterial properties. To be able to predict the long term peformance of deep geologic nuclear waste repositories, a similar knowledge base and computational capability are required. There is concern that in the event of an earthquake, rockfall/rockburst could impede the operations of the repository or damage the waste packages causing a system failure.

The sheer magnitude of such a research undertaking precludes obtaining all of the requisite technology from a single project. Rather, we propose to focus on the issue of transitioning from a continuous rock-like material to fragmented rock material within the context of coupled solid-fluid-mechanical physics. That such an innovative modeling capability is necessary has been made evident by three problems: 1) our inability to predict the path and depth of penetration observed during penetrator field tests, 2) our inability to predict tunnel collapse observed during shock wave interaction with a buried target, and 3) our inability to predict rock failure during deep underground construction and potential seismic loading of nuclear waste repositories.

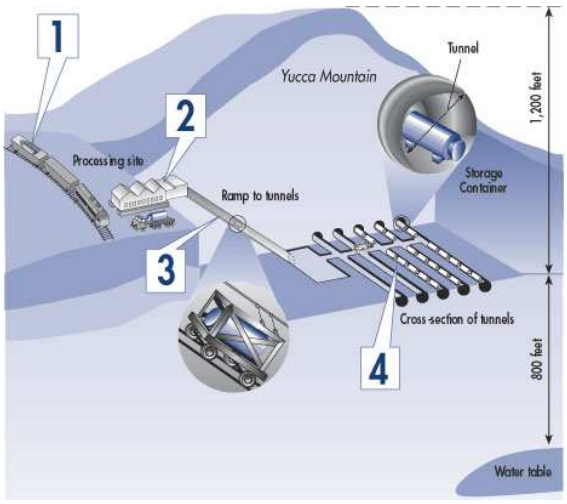

nuclear waste repositories

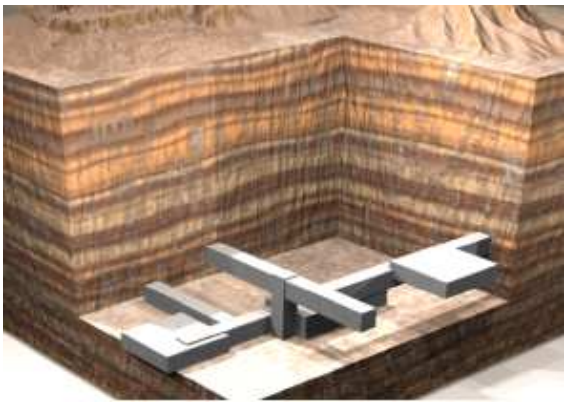

Hard and Deeply Buried Targets (HDBT)

Figure 1.1. Deep underground problems.

Modeling fracture and fragmentation in geomaterials for this class of geomechanical problems requires detailed experimental investigation of the underlying mechanisms of geomaterial fracture and fragmentation, an understanding of the coupled physics environment and the geomaterial response within this environment, proper pre-fracture constitutive response accounting for the transition from onset of localized deformation to macro-cracking, an appropriate fracture/bifurcation criterion and post-bifurcation constitutive response, and sophisticated numerical techniques to propagate (and branch) fracture surfaces leading to fragmentation. To be predictive, constitutive models must be well-posed and physically representative, and numerical simulations must be tractable and independent of spatial discretization (refinement and alignment, i.e. mesh-independent). At the field scale (meters to kilometers), two modeling approaches can be taken: 1) appropriate up-scaling of laboratory-scale-motivated models to field-scale models (not addressed by this project), and 2) finite element meshing of field-scale inhomogeneities, such as strata and rock joints, along with appropriate assignment of geomaterial properties. With a computational tool to simulate potential nuclear waste repository damage due to a seismic event and the defeat of HDBTs, effects of various in-situ geologic characteristics can be analyzed, i.e. propagating

potential uncertainties in our knowledge of in-situ characteristics via a deterministic simulation tool. For example, the Yucca mountain repository site is very well characterized (http://www.ocrwm.doe.gov/ymp/index.shtml), whereas the geologic characteristics around a HDBT are not.

1.2 Approach

Our approach to modeling the transition from continuous to discontinuous geomaterial deformation response may be summarized by the schematic given in Fig.1.2. We use a realistic geomaterial constitutive model (the Sandia GeoModel [20]) to model stage 1 homogeneous deformation up until onset of localized deformation is detected at stage 2. Experimentally, the onset of localized deformation and ensuing post-bifurcation softening responses can be studied by applying true triaxial compression stress conditions to parallelipipeds of rock (cf. Fig.1.4) and sand (cf. Fig1.3). The GeoModel is formulated with strong and weak discontinuity kinematics, deriving bifurcation criteria and post-bifurcation traction-displacement relations. A strong discontinuity is a jump in displacement while a weak discontinuity is a jump in displacement gradient (strain) [62]. To model propagation of a strong discontinuity, a post-bifurcation model is implemented via an assumed enhanced strain variational formulation, embedding the bifurcated response within the standard finite element response. To handle the transition to stage 4, large crack displacements will be accounted for through re-meshing and the introduction of contacting free surfaces along geometries determined by the material model (work not yet done).

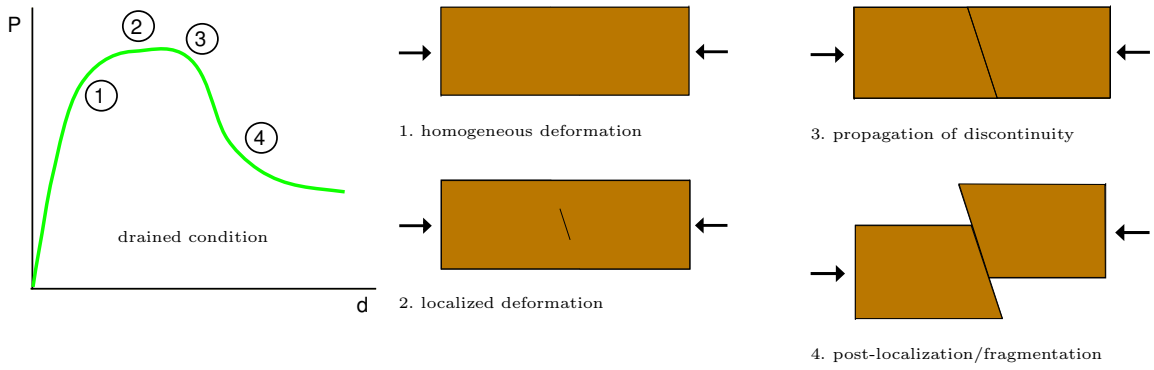

Figure 1.2. Concept of modeling transition from continuous to discontinuous geomaterial deformation response.

A coupled Discrete Element Method (DEM) and Finite Element Method (FEM) can then model fragments cut by the re-mesh step, making the contact search between fragments more computationally efficient than using solely an FEM approach. Details are given in Chapt.7.

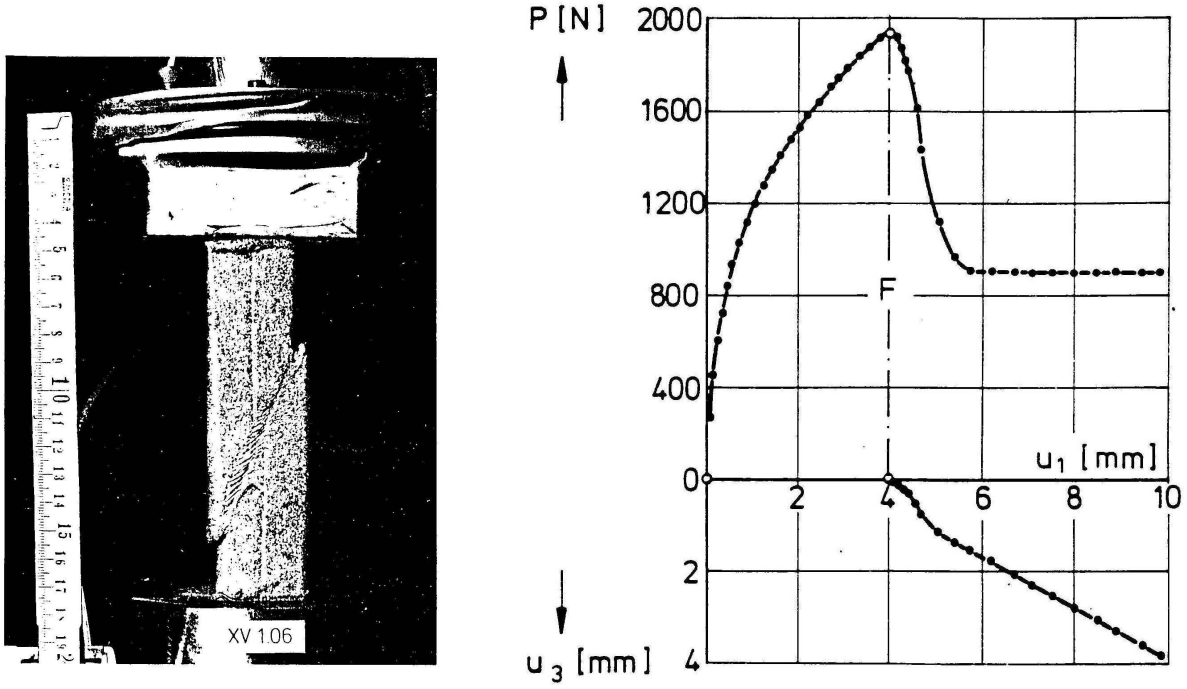

Figure 1.3. Shear banding in dense sand followed by reduction in load carrying capacity of sand specimen [70, 69].

Note that for this project, DEM is used to model fragments discretely as opposed to being used as a micromechanical geomaterial constitutive model, wherein the individual soil or sandstone particles are modeled discretely. This concept is demonstrated in Fig.1.5. For the nuclear waste repository example, a wave produced by a seismic event would propagate until it passes through the tunnel that contains the nuclear waste containment vessel. If the wave acceleration is high enough, it could cause rockfall/rockburst in the tunnel, whereby the falling rock could puncture the containment vessel, leading to shorter safe storage life of the spent nuclear material. Similarly, for the HDBT problem, if the shock wave produced by an earth penetrator is high enough—depending on the depth of the target, its reinforcement or lack thereof, in-situ geological conditions, etc.—rockfall/rockburst could occur in the HDBT.

1.2.1 Discussion of existing models and other potential approaches

Current computational capability for modeling fracture and fragmentation in geomaterials is neither predictive nor independent of spatial discretization. For many Sandia finite element failure analyses, elements are deleted whose stress has reached a specified failure criterion. This deleted mesh volume decreases as the mesh is refined, and as a result the dissipated energy likewise decreases. Mesh-dependent simulations like these have no useful approxi-

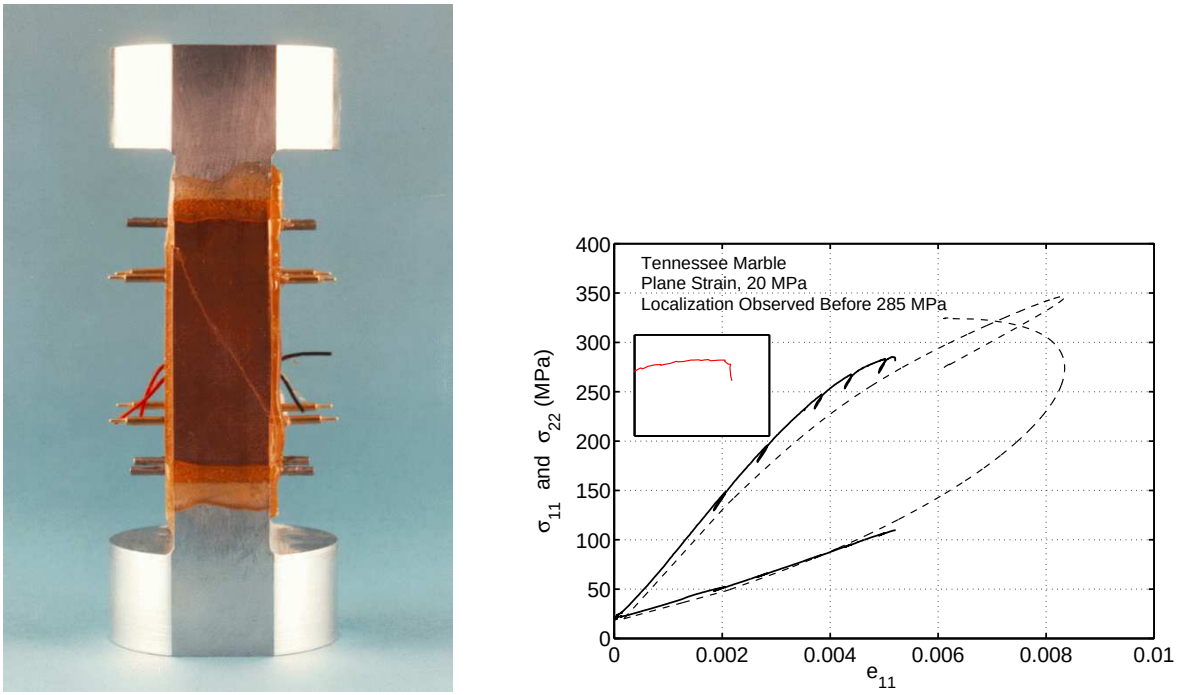

Figure 1.4. Onset of cracking in Tennessee Marble [26].

mation capability. It is well-documented in the literature that mesh-dependence has two causes: 1) ill-posed constitutive equations leading to ill-posed governing partial differential equations (PDE), and 2) inadequate numerical implementation techniques such as the standard finite element method for post-failure response. There are numerous constitutive models for modeling localized deformation leading to free surface formation in geomaterials using nonlocal models and/or bifurcated response models. Nonlocal models for geomaterials typically introduce material length scales to regularize the constitutive model in order to have a well-posed governing PDE and hence mesh-independent simulations. These nonlocal models include spatial gradients of internal state variables and their associated boundary conditions, or they include weighting function integrals of certain internal state variables over domains defined by the length scale. When modeling geomaterials at the laboratory scale (centimeters), physically-based nonlocal models may be needed in order to calculate accurately the onset of localized deformation and transition to macro-cracking. The onset of localized deformation in geomaterials, when analyzed at the micrometer to millimeter scale, can exhibit nonlocal effects such that the deformation at a material point depends spatially on its neighboring material deformation. Local continuum models do not account for these spatial/length-scale effects. It is possible at the field scale (meters to kilometers), we may be able to ignore these nonlocal effects, but we have yet to confirm this assumption. Nonlocal and generalized continuum inelasticity models for geomaterials need further investigatation and are beyond the scope of this report. On that note, however, the start of one such investigation has been supported by the project and is summarized in [39]. Besides

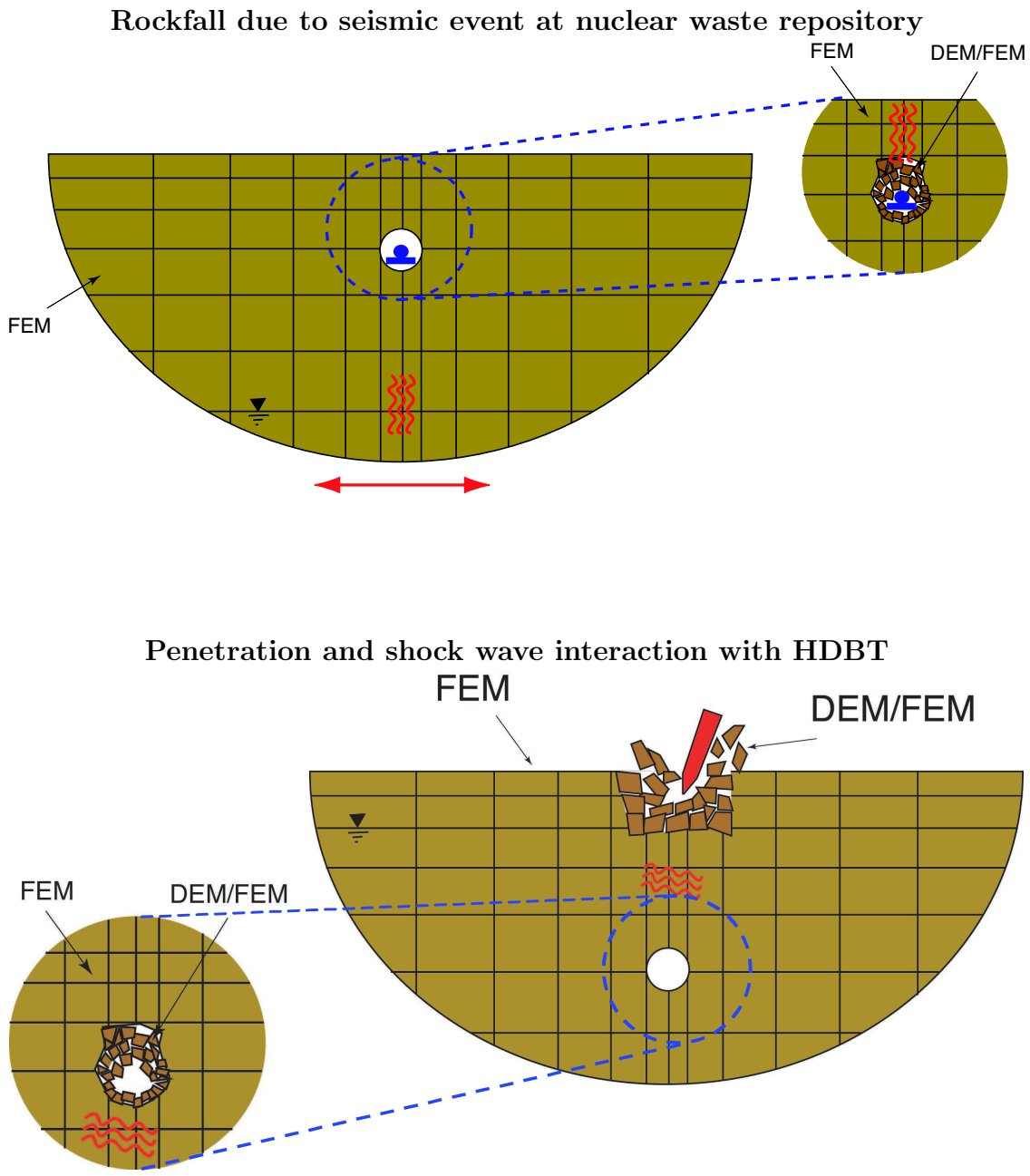

Figure 1.5. Concept of coupled DEM/FEM for modeling rockfall/rockburst for nuclear waste repositories and HDBTs.

nonlocal models, some bifurcated response models also contain a material length scale, and they assume a pre-bifurcation (pre-failure) material response using standard local continuum constitutive models, a bifurcation criterion to determine onset of localized deformation (and fracture), and a post-bifurcation traction-displacement constitutive relation to govern

post-bifurcation response. Examples of such models are the cohesive zone approach [24] and the strong discontinuity approach [62]. We have chosen to use a bifurcated response model that is well-posed (and hence leads to nearly mesh-independent simulations), specifically the Sandia Geomodel [20] formulated with strong and weak discontinuity kinematics.

Various computational techniques are available for implementing bifurcated response models. Here, we summarize and compare a few techniques, including our approach, based on a variational statement of equilibrium (i.e., finite element and meshfree methods).

- **Our Approach (Strong Discontinuity Plasticity / Enhanced Strain Finite Element / Re-Mesh Contacting Free Surfaces / Coupled DEM/FEM for fragmentation):** Rate-dependent, anisotropic, single-surface, geomaterial plasticity model formulated with strong discontinuity kinematics; 3D assumed enhanced strain finite element implementation of strong discontinuity; adaptive re-meshing and insertion of contacting free surfaces to account for large slip and crack-opening displacements; coupled DEM/FEM for modeling fragments cut by re-meshing. **Advantages:** nearly mesh-independent; computationally efficient; account for large crack displacements and fragmentation. **Disadvantages:** crack displacement not continuous between elements and does not resolve stress at crack tip.

- **Strong Discontinuity Plasticity / Meshfree:** Use meshfree method instead of enhanced strain finite element method. **Advantages:** may not need to re-mesh as early in deformation history since meshfree method allows for large distortion of the underlying discretization grid. **Disadvantages:** relatively more expensive, but we plan to consider this approach for future work.

- **Cohesive Zone / Finite Element Method:** use cohesive zone models and cohesive surface elements along continuum element faces [31]. **Advantages:** no bifurcation criterion needed since cohesive zone elements (with inherent cohesive strength) are introduced at each element interface. **Disadvantages:** if elasto-plastic, mesh dependent with regard to refinement and alignment and does not replicate continuous rock-like materials. If rigid-plastic, some sensitivity to mesh alignment.

- **Cohesive Zone / Meshfree:** similar to Strong Discontinuity Plasticity / Meshfree approach; we will consider this approach when considering meshfree methods [31].

- **Extended Finite Element Method (X-FEM):** embed linear elastic, analytical solution at crack tip into X-FEM ([40] and references therein). **Advantages:** continuous crack displacements across element edges potentially providing improved robustness; resolve stress around crack tip. **Disadvantages:** requires analytical solution at crack tip; more expensive because requires additional global degrees of freedom as crack propagates. Extension to 3D requires level sets and potentially more computation time than an embedded discontinuity approach.

1.3 Accomplishments

Accomplishments that will be discussed in more detail in this report are briefly mentioned here. For the reason of providing a potentially more robust bifurcation analysis, an implicit integration of a simplified Sandia GeoModel was carried out [22] and is summarized in Chapt.2. In order to determine loss of ellipticity of the acoustic tensor, a numerical 3D bifurcation algorithm for small deformations was implemented in Tahoe and is discussed in Chapt.3. Also in this chapter is a more extensive bifurcation analysis of the GeoModel. With regard to a post-bifurcation, traction-displacement constitutive law, an elastic-plastic and rigid-plastic cohesive zone model for geomaterials is described in Chapt.4, along with its implementation using a cohesive surface element in Tahoe . For a similar rigid-plastic cohesive zone model, an enhanced strain, embedded discontinuity 3D element implementation is discussed in Chapt.6. Chapter 7 describes the DEM/FEM coupling procedure, presenting results for one way coupling.

1.4 Ongoing research

We are working on the discontinuity tracing algorithm for the embedded discontinuity element (EDE) in three dimensions. Bifurcation conditions for the Sandia GeoModel under locally undrained conditions are being formulated. Also, a two-way DEM/FEM coupling procedure is being developed.

1.5 Future work

Work that we plan to accomplish in the future (cf. Chapt.9):

1. Implement the rigid-plastic geomaterial cohesive zone model using Lagrange multipliers rather than a penalty parameter.

2. Complete a two-way DEM/FEM coupled implementation.

3. Formulate and implement fully coupled solid-fluid mechanical governing equations with strong and weak discontinuities in three-dimensions.

4. In terms of developing a universal bifurcation criterion for rate-sensitive and rate-insensitive constitutive models, we will investigate the evaluation of cohesive zone

yield criteria at various angles within a body. For rate-sensitive materials, bifurcation to localized deformation is not determined by loss of ellipticity as viscous effects regularize the governing equations (cf. Fig.3.7). Perhaps an embedded cohesive zone yield criterion that is rate-sensitive can provide a universal bifurcation criterion for rate-sensitive and rate-insensitive material models.

5. For materials and applications for which localized deformation zones require a weak discontinuity representation (i.e., finite shear band thickness), the embedded weak discontinuity finite element implementation will be considered. Weak discontinuities are more complicated because in order to achieve mesh-independent finite element simulations, several cases must be considered. The element domain may lie completely within the shear band, partially within the shear band, or the shear band may be completely embedded within the finite element. On the other hand, strong discontinuities have measure zero (i.e., have zero thickness, in theory), and hence the discontinuity may always be embedded in a finite element.

6. A major goal of all future work is to extend all formulations and implementations to finite deformations.

7. Of utmost importance is to coordinate our modeling with laboratory experiments and field case studies in order to transfer the modeling and simulation technology to industry users via Tahoe and DMC.

This page intentionally left blank.

Chapter 2

Overview of simplified Sandia GeoModel and its implicit numerical integration

Authors: C.D. Foster, R.A. Regueiro, A.F. Fossum, R.I. Borja

The Sandia GeoModel [20] is a constitutive model that we want to use to model homogeneous deformation of geologic materials up until the point of failure, at which time a post-localization constitutive model and numerical method (such as Cohesive Surface Element in Chapt. 5 and Embedded Discontinuity Element in Chapt. 6) will attempt to model the propagation of cracks until the material is fragmented and then modeled using DEM as discussed in Chapt. 7. Given numerical instabilities resulting from ill-posedness of the governing equation close to when loss of ellipticity is detected (cf. Chapt. 3), it is desirable to have an implicit numerical integration of the constitutive model, which this chapter reports. The contents of this chapter may also be found in the paper [22].

2.1 Introduction

The mechanical behavior of rocks and concrete can involve one or several interacting micromechanical processes. In low-porosity rocks, typically the macroscopic behavior is elastic, followed by dilatancy and shear localization with loss of strength. The dilatational behavior is associated with the onset of microcrack growth [17], [21]. Porous rocks exhibit more varied behavior. At low mean stresses, they often exhibit compaction, followed by significant prefailure dilatation before shear failure. The dilatation can be a result of microcrack growth as above, but also grain rotation and sliding. At higher mean stresses, the material undergoes inelastic compaction resulting from pore collapse, accompanied by strain hardening. On

continued loading, the material may still fail in shear.

To capture these behaviors, we will need fairly advanced constitutive models. Such models can be computationally expensive to numerically integrate. Since yield surfaces and evolution equations are not simple, the evaluations of these functions can be computationally intensive. The ability to minimize the number of function evaluations can save significant run-time costs.

Many of these materials, though certainly not all, are elastically isotropic or approximately so. This restriction can be useful in reducing computation time. For models that also have an isotropic yield function and are isotropically hardening, spectral decomposition can reduce the number of function evaluations and the number of equations to be solved. Tamagnini et al. [66] and Borja et al. [9] have recently used this approach for three-invariant models for geomaterials. The algorithm is not new, however. Simo [58] [60] [59] used spectral directions to enable a return-mapping algorithm for finite deformation plasticity.

The spectral decomposition involves the determination of the eigenvalues and eigenvectors of the stress tensor, which we will refer to as the principal values and principal directions of the tensor. Hence, the stress tensor can be written as

$$\boldsymbol{\sigma} = \sum_{A=1}^{3} \sigma_A \boldsymbol{m}^{(A)} \tag{2.1}$$

where σ_A are the eigenvalues of the stress tensor,

$$\boldsymbol{m}^{(A)} = \boldsymbol{n}^{(A)} \otimes \boldsymbol{n}^{(A)} \qquad \texttt{(no sum)} \tag{2.2}$$

and $\boldsymbol{n}^{(A)}$ are the corresponding eigenvectors.

For isotropic hardening and elasticity, the elastic strain, plastic strain rate, and stress tensors are coaxial, i.e. they share the same principal directions. Hence the spectral decomposition of the elastic strain tensor can be taken as an alternative to the spectral decomposition of the stress tensor.

This decomposition can be put to use in two ways. First, for isotropically hardening models, the trial stress $\boldsymbol{\sigma}^{\text{tr}}_{n+1}$ and converged stress $\boldsymbol{\sigma}_{n+1}$ at time t_{n+1} have the same principal directions. If we decompose the trial stress, we automatically know the principal directions of the converged stress. Then there are only three unknowns, the principal values, needed to determine the full stress state. This number is half the six unknowns needed to determine

the stress tensor using traditional algorithms. Since typically we are dealing with relatively complicated constitutive models with non-linear hardening, these can be solved for using a Newton-Raphson iteration. By reducing the number of equations by three, this algorithm is made more efficient.

Second, the spectral directions can be used to generate the consistent tangent with great efficiency. This formulation relies on the coaxiality of the stress and plastic strain increment, however, a property that is lost when we introduce kinematic hardening.

This paper presents an algorithm for the implicit numerical integration of models that have kinematic hardening or combined isotropic and kinematic hardening using the spectral decomposition of the relative stress (difference between the stress and a back stress; cf. Eq.(2.29)). To the authors' knowledge, this algorithm is novel. Traditionally, these models have been integrated implicitly without spectral decomposition [28] [52] [34] [33] [38] [19] [37] [29] [36] [1], a potentially more computationally costly alternative to the algorithm presented in this paper.

2.1.1 Notation

The summation convention, or Einstein's notation, will be used throughout the paper where not explicitly stated otherwise by the note `(no sum)`. For example, $\sigma_{ii} = \sigma_{11} + \sigma_{22} + \sigma_{33}$. In the previous section, Eq.(2.1) could be written without the summation symbol and still have the same meaning. Equation (2.2) does not have an implied sum only because it is explicitly indicated. Vector and tensor quantities will be written in symbolic form using boldface. Scalar quantities will not be boldface. Vector and tensor products are defined as follows: 1) The symbol '$\cdot$' implies the contraction over the inner index of two vectors or tensors. For example, for vectors $\boldsymbol{a}$ and $\boldsymbol{b}$, $\boldsymbol{a} \cdot \boldsymbol{b} = a_i b_i$, and for tensors $\boldsymbol{\alpha}$ and $\boldsymbol{\beta}$, $(\boldsymbol{\alpha} \cdot \boldsymbol{\beta})_{ij} = \alpha_{ik}\beta_{kj}$. 2) Similarly, the symbol ':' represents the contraction of the innermost two indices of two tensor quantities. For example, $\boldsymbol{\alpha} : \boldsymbol{\beta} = \alpha_{ij}\beta_{ij}$ or $(\boldsymbol{C} : \boldsymbol{\epsilon})_{ij} = C_{ijkl}\epsilon_{kl}$. 3) The symbol symbol '$\otimes$' denotes an outer or tensor product, with no contraction on any of the indices, such that $(\boldsymbol{a} \otimes \boldsymbol{b})_{ij} = a_i b_j$ and $(\boldsymbol{\alpha} \otimes \boldsymbol{\beta})_{ijkl} = \alpha_{ij}\beta_{kl}$.

2.2 Infinitesimal Elastoplasticity

The geomaterial model is formulated within the framework of infinitesimal elastoplasticity and hence is only valid when the displacements and rotations are small. Under these conditions, the strain can be approximated by the infinitesimal strain tensor $\boldsymbol{\epsilon}$

$$\boldsymbol{\epsilon} = \boldsymbol{\nabla}^s \boldsymbol{u} = \frac{1}{2}(\boldsymbol{\nabla}\boldsymbol{u} + (\boldsymbol{\nabla}\boldsymbol{u})^t) \tag{2.3}$$

where $\boldsymbol{u}$ is the displacement vector, $(\bullet)^t$ is the transpose operator, and $(\bullet)^s$ denotes the symmetric part of the tensor. We also assume an additive decomposition of the strain tensor into elastic and plastic parts

$$\boldsymbol{\epsilon} = \boldsymbol{\epsilon}^e + \boldsymbol{\epsilon}^p \tag{2.4}$$

Assuming that a Helmholtz free energy density function $\psi(\boldsymbol{\epsilon}^e, \boldsymbol{\zeta})$ for isothermal conditions depends on the elastic strain $\boldsymbol{\epsilon}^e$ and the vector of strain-like internal state variables $\boldsymbol{\zeta}$ (which will evolve with plastic flow), and following the standard thermodynamic arguments of Coleman and Noll [12] [11], the Clausius-Duhem inequality (dissipation density $\mathcal{D}$) then reads

$$\mathcal{D} \;:=\; \boldsymbol{\sigma} : \dot{\boldsymbol{\epsilon}}^p \;-\; \boldsymbol{q} \cdot \dot{\boldsymbol{\zeta}} \geq\; 0 \tag{2.5}$$

where the stress $\boldsymbol{\sigma}$ and vector of stress-like internal state variables $\boldsymbol{q}$ are determined by

$$\boldsymbol{\sigma} = \rho \frac{\partial \psi}{\partial \boldsymbol{\epsilon}^e} \;; \quad \boldsymbol{q} := \rho \frac{\partial \psi}{\partial \boldsymbol{\zeta}} \tag{2.6}$$

where ρ is the mass density. The variables $\boldsymbol{\sigma}$ and $\boldsymbol{\epsilon}^e$, and $\boldsymbol{q}$ and $\boldsymbol{\zeta}$, are thermodynamically conjugate.

Assuming linear elasticity and linear dependence of $\boldsymbol{q}$ on $\boldsymbol{\zeta}$, the isothermal free energy function is written in quadratic form as

$$\rho\psi(\boldsymbol{\epsilon}^e, \boldsymbol{\zeta}) = \frac{1}{2}\boldsymbol{\epsilon}^e : \boldsymbol{c}^e : \boldsymbol{\epsilon}^e \;+\; \frac{1}{2}\boldsymbol{\zeta} \cdot \boldsymbol{M} \cdot \boldsymbol{\zeta} \;, \tag{2.7}$$

and the resulting constitutive equations in rate form are

$$\dot{\boldsymbol{\sigma}} \;=\; \boldsymbol{c}^e : \dot{\boldsymbol{\epsilon}}^e \;=\; \boldsymbol{c}^e : (\dot{\boldsymbol{\epsilon}} - \dot{\boldsymbol{\epsilon}}^p) \;; \quad \dot{\boldsymbol{q}} \;=\; \boldsymbol{M} \cdot \dot{\boldsymbol{\zeta}} \tag{2.8}$$

where $\boldsymbol{c}^e$ is a constant fourth-order elasticity tensor and $\boldsymbol{M}$ a constant hardening tensor.

Based on the assumptions of the mathematical theory of plasticity, the behavior is elastic at a given stress state if a given convex yield function, $f(\boldsymbol{\sigma}, \boldsymbol{q})$, is less than zero. Plastic flow can only occur when $f = 0$, and values of $\boldsymbol{\sigma}$ and $\boldsymbol{q}$ that result in $f > 0$ are inadmissible. For a given set of internal state variables, we refer to $\{\boldsymbol{\sigma} : f(\boldsymbol{\sigma}, \boldsymbol{q}) = 0\}$ as the *yield surface*.

We assume also the existence of a plastic potential function g that dictates the direction of plastic flow via the equation

$$\dot{\boldsymbol{\epsilon}}^p = \dot{\gamma} \frac{\partial g}{\partial \boldsymbol{\sigma}} \tag{2.9}$$

where $\dot{\gamma}$ is the consistency parameter. If $g = f$, the model is associative in its plasticity. We assume also that the evolution of the internal state variables is related to $\dot{\gamma}$ via a set of hardening functions

$$\dot{\boldsymbol{\zeta}} := \dot{\gamma} \boldsymbol{h}(\boldsymbol{\sigma}, \boldsymbol{q}) \Longrightarrow \dot{\boldsymbol{q}} = \dot{\gamma} \boldsymbol{M} \cdot \boldsymbol{h}(\boldsymbol{\sigma}, \boldsymbol{q}) = \dot{\gamma} \boldsymbol{h}^q(\boldsymbol{\sigma}, \boldsymbol{q}) \tag{2.10}$$

Using Eq.(2.10) and the consistency condition

$$0 = \dot{f} = \frac{\partial f}{\partial \boldsymbol{\sigma}} : \dot{\boldsymbol{\sigma}} + \frac{\partial f}{\partial \boldsymbol{q}} \cdot \dot{\boldsymbol{q}} \,, \tag{2.11}$$

we can solve for the consistency parameter

$$\dot{\gamma} \;=\; \frac{(\partial f / \partial \boldsymbol{\sigma}) : \boldsymbol{c}^e : \dot{\boldsymbol{\epsilon}}}{(\partial f / \partial \boldsymbol{\sigma}) : \boldsymbol{c}^e : (\partial g / \partial \boldsymbol{\sigma}) - (\partial f / \partial \boldsymbol{q}) \cdot \boldsymbol{h}^q} \;=\; \frac{1}{\chi} \frac{\partial f}{\partial \boldsymbol{\sigma}} : \boldsymbol{c}^e : \dot{\boldsymbol{\epsilon}} \tag{2.12}$$

We substitute (2.12) into (2.9) and $(2.8)_1$ to solve for the continuum tangent modulus as

$$\dot{\boldsymbol{\sigma}} \;=\; \left(\boldsymbol{c}^e - \frac{1}{\chi} \boldsymbol{c}^e : \frac{\partial g}{\partial \boldsymbol{\sigma}} \otimes \frac{\partial f}{\partial \boldsymbol{\sigma}} : \boldsymbol{c}^e \right) : \dot{\boldsymbol{\epsilon}} \;=\; \boldsymbol{c}^{ep} : \dot{\boldsymbol{\epsilon}} \tag{2.13}$$

2.3 Stress Invariants

Since the model is isotropic in its elasticity, the yield function can be expressed in terms of invariants. Using invariants guarantees that the material will behave in the same manner regardless of loading direction. For a 3-by-3 symmetric matrix, there are three independent invariants. The ones we will use are:

$$I_1 = \mathrm{tr}(\boldsymbol{\sigma}) \tag{2.14}$$

$$J_2 = \frac{1}{2}\left(\boldsymbol{\sigma} - \frac{I_1}{3}\mathbf{1}\right) : \left(\boldsymbol{\sigma} - \frac{I_1}{3}\mathbf{1}\right) = \frac{1}{2}\boldsymbol{s} : \boldsymbol{s} \tag{2.15}$$

$$J_3 = \det(\boldsymbol{s}) \tag{2.16}$$

where $\mathrm{tr}(\boldsymbol{\sigma}) = \sigma_{ii}$. Notice that I_1 is simply three times the mean stress. J_2 can be thought of as a generalized measure of the shear stress acting on all planes, and J_3 reflects the behavioral feature in triaxial extension and triaxial compression. This last point will be discussed in more detail in Section 2.4.2.

2.4 Geomaterial model

Moduli, yield and plastic potential functions, and hardening functions are defined in this section to specify a geomaterial constitutive model. Limited physical motivation is presented since this paper focuses on implicit numerical integration of the model. The reader is referred to [21] [20] for further motivation of the model.

2.4.1 Constitutive equations

We assume the elastic response is isotropic, such that $\boldsymbol{c}^e$ has the form

$$\boldsymbol{c}^e = \lambda \mathbf{1} \otimes \mathbf{1} + 2\mu \boldsymbol{I} \tag{2.17}$$

where $\mathbf{1}$ is the second order identity tensor, $(\mathbf{1})_{ij} = \delta_{ij}$, $\boldsymbol{I}$ is the fourth-order symmetric identity tensor, $(\boldsymbol{I})_{ijkl} = \frac{1}{2}(\delta_{ik}\delta_{jl} + \delta_{il}\delta_{jk})$, λ and μ are the Lamé constants, and δ_{ij} is the Kronecker delta.

For the internal state variables we define

$$\boldsymbol{q} := \left\{ \begin{array}{c} \boldsymbol{\alpha} \\ \kappa \end{array} \right\} \quad ; \qquad \boldsymbol{M} := \left[\begin{array}{cc} c^{\alpha}\boldsymbol{I} & \boldsymbol{0} \\ \boldsymbol{0} & c^{\kappa} \end{array} \right] \tag{2.18}$$

where $\boldsymbol{\alpha}$ is the back stress associated with deviatoric plasticity and cyclic loading, κ the isotropic stress-like internal state variable associated with compaction hardening, and c^{α} and c^{κ} are hardening parameters for $\boldsymbol{\alpha}$ and κ, respectively.

2.4.2 Yield function

The yield surface for the model has several components to capture the various behaviors described in the introduction. At its core is an exponential shear failure function

$$F_f(I_1) = A - C\exp(BI_1) - \theta I_1 \tag{2.19}$$

where A, B, C, and θ are all non-negative material parameters that are fit to the failure data, more exactly to experimental peak stress for various confining pressures. This function captures the pressure-dependence of the shear strength of these materials. The shear strength increases with more compressive mean stresses (Fig. 2.1), without the linear dependence associated with a simpler Mohr-Coulomb or Drucker-Prager approximation. These latter two models tend to overpredict shear strength at high pressures. The parameter θ is the asymptotic slope of this surface, recognizing that the pressure may still have some effect, though lesser, at highly compressive mean stresses. The initial yield surface is offset from the failure surface by a material parameter N, hence the first approximation of the yield function can be written as

$$f_1 = \sqrt{J_2} - (F_f - N) \tag{2.20}$$

or

$$\tilde{f}_1 = J_2 - (F_f - N)^2 \tag{2.21}$$

These two functions are negative, zero, and positive in the same regions. For implementation purposes, the second form will be easier and more efficient.

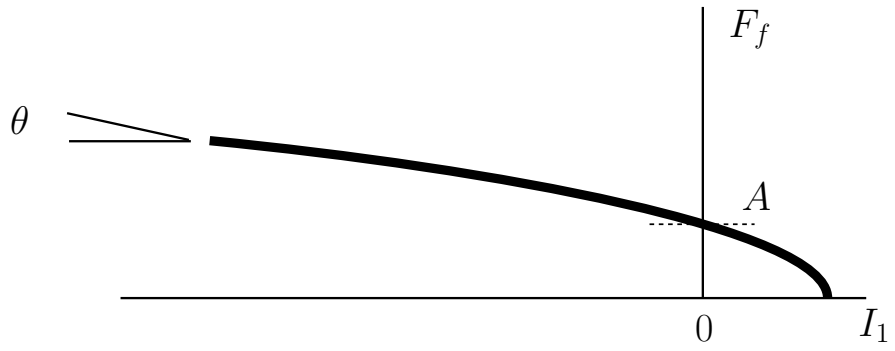

Figure 2.1. Shear failure surface F_f.

The next step is to multiply the second term in Eq.(2.21) by an elliptical cap function to account for yielding in compression.

$$f_2 \;=\; J_2 - F_c(F_f - N)^2 \tag{2.22}$$

where

$$F_c(I_1) \;=\; 1 - H(\kappa - I_1)\left(\frac{I_1 - \kappa}{X - \kappa}\right)^2 \tag{2.23}$$

$$X(\kappa) \;=\; \kappa - RF_f(\kappa) \tag{2.24}$$

and $H(x)$ is the Heaviside function. The effect of this function is that at some value of the mean stress, κ, the yield surface f_2 begins to deviate from the shear yield surface, and as the mean stress decreases (becomes more compressive/negative) the shear strength decreases, until a point X is reached, where there is no shear strength (Fig. 2.2). Hence, a smooth cap is created for the yield surface (Fig. 2.3). X is calculated such that the distance between κ and X is proportional to $F_f(\kappa)$, with the constant of proportionality being the material parameter R. κ is an internal state variable and will be allowed to harden. X is also an internal state variable, but is completely dependent on κ, which is the variable we will track.

Geomaterials also have a noticeably weaker strength in triaxial extension compared to triaxial compression. That is, at a given mean stress, the material will fail sooner if the principal stress that is farthest from the mean stress is so in a tensile direction rather than a compressive direction. To capture this effect, we use the Lode angle

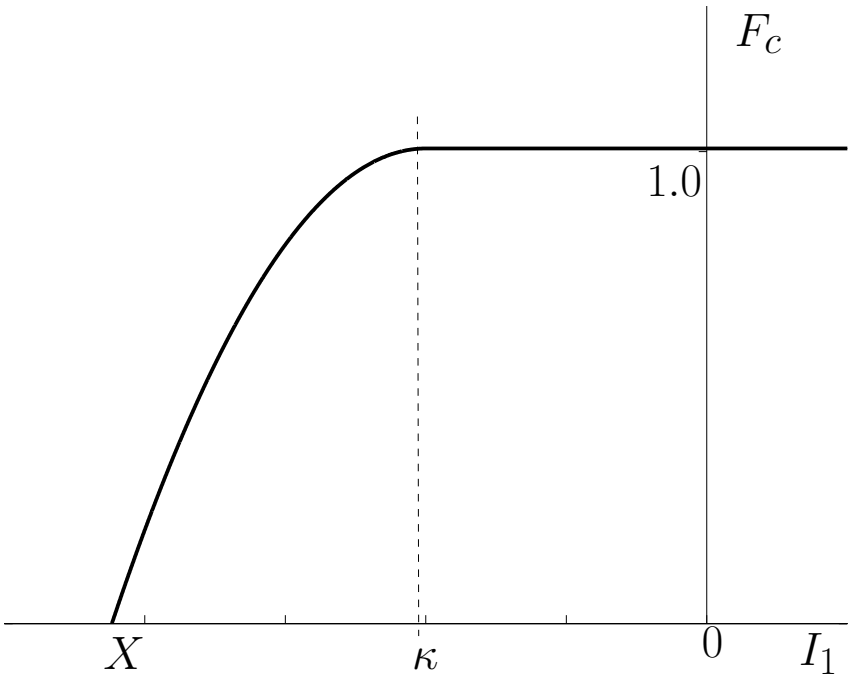

Figure 2.2. Cap function F_c.

$$\beta = \frac{-1}{3}\sin^{-1}\left(\frac{3\sqrt{3}J_3}{2(J_2)^{3/2}}\right) \tag{2.25}$$

We can now introduce the third-invariant modifying function Γ to account for this difference.

$$\Gamma(\beta) = \frac{1}{2}\left(1 + \sin 3\beta + \frac{1}{\psi}(1 - \sin 3\beta)\right) \tag{2.26}$$

$$= \frac{1}{2}\left(1 - \frac{3\sqrt{3}J_3}{2(J_2)^{3/2}} + \frac{1}{\psi}\left(1 + \frac{3\sqrt{3}J_3}{2(J_2)^{3/2}}\right)\right) \tag{2.27}$$

where ψ is the ratio of triaxial extension strength to compression strength, a material constant. Now

$$f_3 = \Gamma^2 J_2 - F_c(F_f - N)^2 \tag{2.28}$$

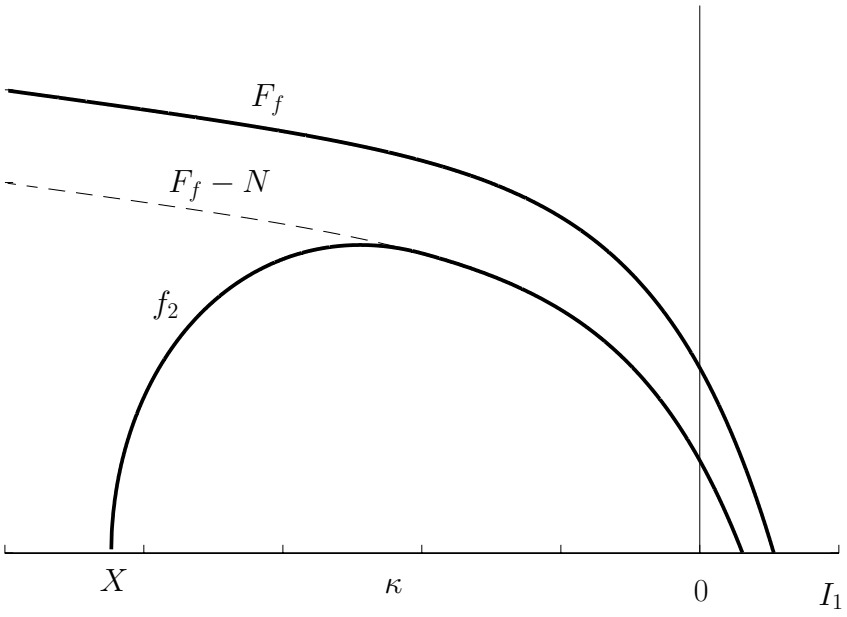

Figure 2.3. Yield surface f_2 in meridional stress space, along with the shear failure surface F_f and the shear yield surface $F_f - N$.

This creates a smooth Mohr-Coulomb approximation in the π-plane (Fig. 2.4).

The final modification to the yield surface is the introduction of the back stress tensor $\boldsymbol{\alpha}$ to capture the Bauschinger effect for cyclic loading. We use a deviatoric, translational back stress. From this we can define the relative stress

$$\boldsymbol{\xi} = \boldsymbol{\sigma} - \boldsymbol{\alpha} \tag{2.29}$$

All the invariants will now be calculated from the relative stress, and we arrive at the final form of our yield function

$$f \;=\; (\Gamma^{\xi})^2 J_2^{\xi} - F_c(F_f - N)^2 \;=\; 0 \tag{2.30}$$

where the superscript ξ indicates that all quantities are computed from the relative stress tensor, rather than the absolute stress tensor. The back stress tensor will be deviatoric, hence quantities such as I_1, F_c, and F_f will remain unchanged.

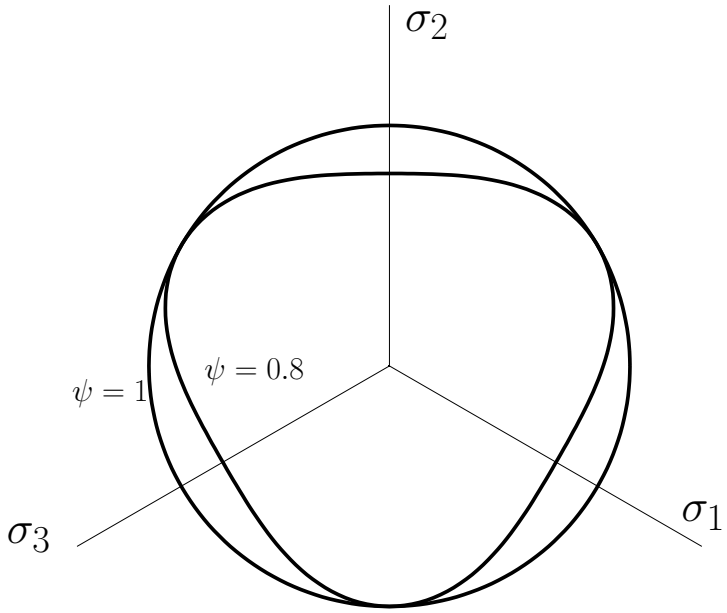

Figure 2.4. Yield surface in π-plane, for $\psi = 1$ and $\psi = 0.8$

Similarly, we introduce a plastic potential function g of the same form, but perhaps with distinct material parameters, as

$$g \;=\; (\Gamma^{\xi})^2 J_2^{\xi} - F_c^g (F_f^g - N)^2 \tag{2.31}$$

where

$$F_f^g(I_1) = A - C\exp(LI_1) - \phi I_1 \tag{2.32}$$

and

$$F_c^g(I_1) \;=\; 1 - H(\kappa - I_1)\left(\frac{I_1 - \kappa}{X^g - \kappa}\right)^2 \tag{2.33}$$

$$X^g(\kappa) \;=\; \kappa - QF_f^g(\kappa) \tag{2.34}$$

where if $L = B$, $\phi = \theta$, and $Q = R$, plastic flow is associative. Nonassociative plastic flow has been observed for low-porosity rocks [44]. The frictional strength parameters B, θ, and R typically overestimate the observed volumetric plastic deformation, warranting a nonassociative model with L, ϕ, and Q determined from experimental measurements of volumetric plastic deformation.

2.4.3 Hardening functions

The cap hardening parameter κ and deviatoric back stress $\boldsymbol{\alpha}$ evolve with plastic deformation. As one might expect, the evolution of κ is related to mean stress, and more directly to the plastic volumetric strain, ϵ_v^p, while the evolution of the back stress is related to the deviatoric plastic strain, $\boldsymbol{e}^p$.

The evolution of the back stress takes the form [21] [20]

$$\dot{\boldsymbol{\alpha}} := c^\alpha G^\alpha \dot{\boldsymbol{e}}^p = c^\alpha G^\alpha (\dot{\boldsymbol{\epsilon}}^p - \frac{1}{3}\mathrm{tr}(\dot{\boldsymbol{\epsilon}}^p)\mathbf{1}) = c^\alpha G^\alpha \dot{\gamma} \left(\frac{\partial g}{\partial \boldsymbol{\sigma}} - \frac{1}{3}\frac{\partial g}{\partial I_1}\mathbf{1} \right) \tag{2.35}$$

where c^α is a material parameter that controls the rate of hardening, and is the same as that found in Eq.(2.18). G^α is a function which limits the growth of the back stress tensor as it approaches the failure surface. It takes the form

$$G^\alpha(\boldsymbol{\alpha}) \;=\; 1 \;-\; \frac{\sqrt{J_2^\alpha}}{N} \quad , \qquad J_2^\alpha \;=\; \frac{1}{2}\boldsymbol{\alpha} : \boldsymbol{\alpha} \tag{2.36}$$

As the yield surface meets the failure surface in stress space, $G^\alpha(\boldsymbol{\alpha}) = 0$, and further deviatoric loading leads to perfect plasticity.

To determine how the cap parameter evolves in Eq. (2.10), the following form for the plastic volumetric strain is used [21]

$$\epsilon_v^p = W\left(\exp\left\{[D_1 - D_2(X(\kappa) - X_0)](X(\kappa) - X_0)\right\} - 1\right) \tag{2.37}$$

if $\dot{X} < 0$ (i.e., cap hardening). X is not allowed to increase, as this would result in softening of the cap, which appears to be unphysical behavior for these materials [55] [54]. $\dot{\kappa}$ has the same sign as $\dot{X}$, and hence the same restriction applies. For the case where κ is decreasing (cap hardening), we can calculate the change by noting

$$\dot{\epsilon}_v^p = \mathrm{tr}(\dot{\boldsymbol{\epsilon}}^p) = 3\dot{\gamma}\frac{\partial g}{\partial I_1} \tag{2.38}$$

and

$$\dot{\epsilon}_v^p = \frac{\partial \epsilon_v^p}{\partial X}\frac{\partial X}{\partial \kappa}\dot{\kappa} \tag{2.39}$$

Equating Eqs.(2.38) and (2.39), the evolution equation for κ that results is

$$\dot{\kappa} = 3\dot{\gamma}\frac{\partial g}{\partial I_1}\Bigg/\left(\frac{\partial \epsilon_v^p}{\partial X}\frac{\partial X}{\partial \kappa}\right) \tag{2.40}$$

The evolution of the strain-like internal state variables can easily be back-figured from the equations above. We define the hardening functions $\boldsymbol{h}$ for these variables as

$$\dot{\boldsymbol{\zeta}} \;=\; \dot{\gamma}\boldsymbol{h}(\boldsymbol{\sigma},\boldsymbol{q}) \quad ; \qquad \boldsymbol{h}(\boldsymbol{\sigma},\boldsymbol{q}) := \left\{ \begin{array}{c} G^{\alpha}(\boldsymbol{\alpha})\,(\partial g/\partial \boldsymbol{\sigma} - (1/3)(\partial g/\partial I_1)\mathbf{1}) \\ 3(\partial g/\partial I_1)\Big/\left[K(\partial \epsilon_v^p/\partial X)(\partial X/\partial \kappa)\right] \end{array} \right\} \tag{2.41}$$

$$\boldsymbol{h}^q = \left\{ \begin{array}{c} \boldsymbol{h}^{\alpha} \\ h^{\kappa} \end{array} \right\} = \boldsymbol{M}\cdot\boldsymbol{h}(\boldsymbol{\sigma},\boldsymbol{q}) \tag{2.42}$$

where $K = \lambda + 2\mu/3$ is the bulk modulus, and $c^{\kappa} = K$ in Eq.(2.18). We could have chosen any quantity with units of stress for c^{κ}, but the bulk modulus seems natural given κ's relationship to volumetric strain.

The above equations describe the model used in this paper. However, it should be noted that a localized deformation model is being formulated that would handle post-localization response. Furthermore, the model has been extended to include the effects of nonlinear elasticity, rate dependence, and transverse isotropy [20].

2.5 Return mapping algorithm for implicit integration

We consider a strain-driven problem. Given a strain increment $\Delta\boldsymbol{\epsilon}$ and the values of the stress and internal state variables at time t_n, the goal is to solve for the values of these variables at time t_{n+1}, using the evolution equations in (2.8), (2.9), and (2.41). However, simultaneous integration of these evolution equations is complicated. The typical solution to this problem is to use an approximate numerical technique. Because of its simplicity and unconditional stability, we integrate our equations using an implicit Euler scheme. While this scheme has the above mentioned advantages, we should note that it has two drawbacks: it is only first-order accurate in the time increment, and it is an implicit scheme. Using the implicit Euler approximation, the discrete versions of (2.8), (2.9), and (2.41) become

$$\Delta\boldsymbol{\sigma} = \boldsymbol{c}^e : \left(\Delta\boldsymbol{\epsilon} - \Delta\gamma\left(\frac{\partial g}{\partial\boldsymbol{\sigma}}\right)_{n+1}\right) \tag{2.43}$$

$$\Delta\boldsymbol{\alpha} = c^\alpha G^\alpha(\boldsymbol{\alpha}_{n+1})\Delta\gamma\left(\frac{\partial g}{\partial\boldsymbol{\sigma}} - \frac{1}{3}\frac{\partial g}{\partial I_1}\mathbf{1}\right)_{n+1} \tag{2.44}$$

$$\Delta\kappa = 3\Delta\gamma\left(\frac{\partial g}{\partial I_1}\Big/\left(\frac{\partial\epsilon_v^p}{\partial X}\frac{\partial X}{\partial\kappa}\right)\right)_{n+1} \tag{2.45}$$

where $\Delta\boldsymbol{\sigma} = \boldsymbol{\sigma}_{n+1} - \boldsymbol{\sigma}_n$, etc. Hence the solution of $\boldsymbol{\sigma}_{n+1}$, $\boldsymbol{\alpha}_{n+1}$, and κ_{n+1} are trivial from the above equations. Equation (2.43) is often conveniently rewritten as

$$\boldsymbol{\sigma}_{n+1} = \boldsymbol{\sigma}^{\rm tr}_{n+1} - \Delta\gamma\boldsymbol{c}^e : \left(\frac{\partial g}{\partial\boldsymbol{\sigma}}\right)_{n+1} \tag{2.46}$$

where $\boldsymbol{\sigma}^{\rm tr}_{n+1}$ is the trial predictor stress based on the assumption that the increment is elastic

$$\boldsymbol{\sigma}^{\rm tr}_{n+1} = \boldsymbol{\sigma}_n + \boldsymbol{c}^e : \Delta\boldsymbol{\epsilon} \tag{2.47}$$

It is convenient to rewrite this equation further as

$$\boldsymbol{\sigma}^{\rm corr} := \boldsymbol{\sigma}_{n+1} - \boldsymbol{\sigma}^{\rm tr}_{n+1} = -\Delta\gamma\boldsymbol{c}^e : \left(\frac{\partial g}{\partial\boldsymbol{\sigma}}\right)_{n+1} \tag{2.48}$$

where $\boldsymbol{\sigma}^{\rm corr}$ is the plastic corrector for the stress increment.

In the plastic regime, the solution of these equations involves the introduction of an additional variable, the incremental consistency parameter $\Delta\gamma$. Hence we need an additional equation to solve the system of equations, and that is the yield function evaluated at time t_{n+1}

$$f_{n+1} = 0 \tag{2.49}$$

To solve this system of equations, functions are evaluated at time t_{n+1}. This system is typically solved by a Newton-Raphson type iteration. Our vector of unknowns is

$$\boldsymbol{Z} \;=\; \left\{ \; \sigma_{11} \; \sigma_{22} \; \sigma_{33} \; \sigma_{23} \; \sigma_{31} \; \sigma_{12} \; \alpha_{11} \; \alpha_{22} \; \alpha_{23} \; \alpha_{31} \; \alpha_{12} \; \kappa \; \Delta\gamma \; \right\}^t \tag{2.50}$$

and our residual vector

$$\hat{\boldsymbol{R}}(\boldsymbol{Z}) \;=\; \left\{ \begin{array}{c} \Delta\gamma c^e_{11kl}(\partial g/\partial\sigma_{kl}) - \sigma_{11} + \sigma^{\rm tr}_{11} \\ \Delta\gamma c^e_{22kl}(\partial g/\partial\sigma_{kl}) - \sigma_{22} + \sigma^{\rm tr}_{22} \\ \Delta\gamma c^e_{33kl}(\partial g/\partial\sigma_{kl}) - \sigma_{33} + \sigma^{\rm tr}_{33} \\ \Delta\gamma c^e_{23kl}(\partial g/\partial\sigma_{kl}) - \sigma_{23} + \sigma^{\rm tr}_{23} \\ \Delta\gamma c^e_{31kl}(\partial g/\partial\sigma_{kl}) - \sigma_{31} + \sigma^{\rm tr}_{31} \\ \Delta\gamma c^e_{12kl}(\partial g/\partial\sigma_{kl}) - \sigma_{12} + \sigma^{\rm tr}_{12} \\ \Delta\gamma(h^\alpha)_{11} - \alpha_{11} + (\alpha_{11})_n \\ \Delta\gamma(h^\alpha)_{22} - \alpha_{22} + (\alpha_{22})_n \\ \Delta\gamma(h^\alpha)_{23} - \alpha_{23} + (\alpha_{23})_n \\ \Delta\gamma(h^\alpha)_{31} - \alpha_{31} + (\alpha_{31})_n \\ \Delta\gamma(h^\alpha)_{12} - \alpha_{12} + (\alpha_{12})_n \\ \Delta\gamma h^\kappa - \kappa + \kappa_n \\ f \end{array} \right\} = \mathbf{0} \tag{2.51}$$

where subscript $n+1$ is left off to simplify notation. Here $\alpha_{33} = -(\alpha_{11} + \alpha_{22})$ can be eliminated since the back stress is deviatoric. Even condensing out α_{33}, we are left with 13 equations and 13 unknowns. The linear system has to be solved several times as we iterate to find the solution.

We could save time in this algorithm if we could reduce the number of unknowns. Not only would this reduce the size of the matrix to be inverted, but it would also reduce the number of function evaluations, which is expensive given the complexity of the yield function and evolution equations. Tamagnini et al. [66] and Borja et al. [9] have used spectral decomposition to do this in the case of the isotropic hardening models. However, these algorithms rely on the fact that the trial stress $\boldsymbol{\sigma}^{\rm tr}_{n+1}$ has the same spectral directions

as $\partial g/\partial \boldsymbol{\sigma}$ (and from this the converged stress also has the same spectral directions). This is not in general true for kinematically hardening models. In fact, recall that for the relative stress $\boldsymbol{\xi} = \boldsymbol{\sigma} - \boldsymbol{\alpha}$, we can see that

$$\frac{\partial g}{\partial \boldsymbol{\sigma}} = \frac{\partial g}{\partial \boldsymbol{\xi}} \frac{\partial \boldsymbol{\xi}}{\partial \boldsymbol{\sigma}} = \frac{\partial g}{\partial \boldsymbol{\xi}} \tag{2.52}$$

Since the plastic potential function g depends only on the invariants of the relative stress, it is easy to show that $\boldsymbol{\xi}$ and $\partial g/\partial \boldsymbol{\xi}$ have the same spectral directions. Clearly, the spectral directions of the stress and relative stress may be different. The approach of spectrally decomposing the relative stress, however, has promise. From Eq.(2.48), $\boldsymbol{\sigma}^{\text{corr}}$ also will have the same spectral directions as the relative stress since multiplication by an isotropic tensor $\boldsymbol{c}^e$ preserves spectral directions. From Eq.(2.44), since $\mathbf{1}$ is hydrostatic and can have any spectral decomposition, $\Delta\boldsymbol{\alpha}$ also will have the same spectral directions as the relative stress. Finally, the trial relative stress can be written as

$$\boldsymbol{\xi}^{\text{tr}}_{n+1} = \boldsymbol{\sigma}^{\text{tr}}_{n+1} - \boldsymbol{\alpha}_n = \boldsymbol{\xi}_{n+1} - \boldsymbol{\sigma}^{\text{corr}} + \Delta\boldsymbol{\alpha} \tag{2.53}$$

such that it shares the same spectral directions as the converged relative stress $\boldsymbol{\xi}_{n+1}$, plastic corrector stress $\boldsymbol{\sigma}^{\text{corr}}$, and back stress increment $\Delta\boldsymbol{\alpha}$. The trial relative stress $\boldsymbol{\xi}^{\text{tr}}_{n+1}$ is the critical quantity because it is known *a priori*.

We calculate the trial relative stress and spectrally decompose it using a Jacobi iteration. While this method is slow for larger matrices, speed of convergence was good for these 3-by-3 matrices. The algorithm is described in [16] among many other places. We have chosen to express the yield condition in terms of the principal relative stresses, so we use the trial relative stresses to check yielding.

If there is yielding, we would like to put the spectral decomposition to good use. As we have noted, however, the tensor unknowns for which we need to solve, the stress and back stress, do not share the same spectral decomposition. To avoid this difficulty, we modify the unknowns that we iterate. We can easily update the stress and back stress if we have $\boldsymbol{\sigma}^{\text{corr}}$ and $\Delta\boldsymbol{\alpha}$. Since we already have the spectral directions for those tensors, we only need to solve for the principal values.

Hence the vector of unknowns becomes

$$\boldsymbol{X} \;=\; \left\{ \; \sigma^{\text{corr}}_I \;\; \sigma^{\text{corr}}_{II} \;\; \sigma^{\text{corr}}_{III} \;\; \Delta\alpha_I \;\; \Delta\alpha_{II} \;\; \Delta\kappa \;\; \Delta\gamma \; \right\}^t \tag{2.54}$$

Again, α_{III} is eliminated since the back stress is deviatoric.

Using a change of coordinates to the principal directions, the residual vector then becomes

$$\boldsymbol{R} = \left\{ \begin{array}{c} \Delta\gamma a^e_{1A}(\partial g/\partial \xi_A) + \sigma^{\text{corr}}_I \\ \Delta\gamma a^e_{2A}(\partial g/\partial \xi_A) + \sigma^{\text{corr}}_{II} \\ \Delta\gamma a^e_{3A}(\partial g/\partial \xi_A) + \sigma^{\text{corr}}_{III} \\ \Delta\gamma (h^\alpha)_I - \Delta\alpha_I \\ \Delta\gamma (h^\alpha)_{II} - \Delta\alpha_{II} \\ \Delta\gamma h^\kappa - \Delta\kappa \\ f \end{array} \right\} = \mathbf{0} \tag{2.55}$$

where subscript $n+1$ is left off, and the tensor $\boldsymbol{a}^e$ is the elasticity tensor projected to principal relative stress space,

$$\boldsymbol{a}^e = \left[\begin{array}{ccc} \lambda + 2\mu & \lambda & \lambda \\ \lambda & \lambda + 2\mu & \lambda \\ \lambda & \lambda & \lambda + 2\mu \end{array} \right] \tag{2.56}$$

Since the yield and hardening functions are expressed in terms of stress invariants, the easiest way to calculate the derivatives is

$$\frac{\partial(\bullet)}{\partial \xi_A} = \frac{\partial(\bullet)}{\partial I_1}\frac{\partial I_1}{\partial \xi_A} + \frac{\partial(\bullet)}{\partial J^\xi_2}\frac{\partial J^\xi_2}{\partial \xi_A} + \frac{\partial(\bullet)}{\partial J^\xi_3}\frac{\partial J^\xi_3}{\partial \xi_A} \tag{2.57}$$

$$= \frac{\partial(\bullet)}{\partial I_1} + \frac{\partial(\bullet)}{\partial J^\xi_2}\left(\xi_A - \frac{1}{3}I_1\right) + \frac{\partial(\bullet)}{\partial J^\xi_3}\left[\left(\xi_A - \frac{1}{3}I_1\right)^2 - \frac{2}{3}J^\xi_2\right] \tag{2.58}$$

The smaller system can now be solved using a Newton-Raphson iteration

$$\boldsymbol{X}^{k+1}_{n+1} = \boldsymbol{X}^k_{n+1} - \left[\left(\frac{D\boldsymbol{R}}{D\boldsymbol{X}}\right)^k_{n+1}\right]^{-1} \boldsymbol{R}^k_{n+1} \tag{2.59}$$

where in practice the inverse is not explicitly computed, and the equations are solved using an LU decomposition; $k+1$ refers to the current iteration. Since the updates to the stress and back stress may not have the same spectral decomposition as the stress and back stress themselves, we update as follows

$$\boldsymbol{\sigma} = \boldsymbol{\sigma}^{\mathrm{tr}} + \sum_{A=1}^{3} \sigma_A^{\mathrm{corr}} \boldsymbol{m}^{(A)} \tag{2.60}$$

$$\boldsymbol{\alpha} = \boldsymbol{\alpha}_n + \sum_{B=1}^{2} \Delta\alpha_B (\boldsymbol{m}^{(B)} - \boldsymbol{m}^{(III)}) \tag{2.61}$$

$$\kappa = \kappa_n + \Delta\kappa \tag{2.62}$$

where the subscript $n+1$ is left off to simplify notation. Here the index B runs only from 1 to 2, since only two independent principal values of the evolution of the back stress are calculated.

This algorithm is summarized in Box 1.

Box 1. Summary of stress-point algorithm

Step 1. Compute $\boldsymbol{\sigma}^{\mathrm{tr}}_{n+1} = \boldsymbol{\sigma}_n + \boldsymbol{c}^e : \Delta\boldsymbol{\epsilon}$
Step 2. Spectrally decompose $\boldsymbol{\xi}^{\mathrm{tr}}_{n+1} = \boldsymbol{\sigma}^{\mathrm{tr}}_{n+1} - \boldsymbol{\alpha}_n = \sum_{A=1}^{3} \xi^{\mathrm{tr}}_A \boldsymbol{m}^{(A)}$
Step 3. Check yielding: is $f > 0$?
    If no, set $\boldsymbol{\sigma}_{n+1} = \boldsymbol{\sigma}^{\mathrm{tr}}_{n+1}$ and exit.
Step 4. If yes, set $\boldsymbol{X}_0 = \boldsymbol{0}$ and iterate:
    $\delta\boldsymbol{X}^k = \left[(-D\boldsymbol{R}/D\boldsymbol{X})^k\right]^{-1} \boldsymbol{R}(\boldsymbol{X}^k)$
    $\boldsymbol{X}^{k+1} = \boldsymbol{X}^k + \delta\boldsymbol{X}^k$
    until $(R_\sigma/R_{\sigma,\max}) < \mathrm{tol}_\sigma$, $(R_\alpha/R_{\alpha,\max}) < \mathrm{tol}_\alpha$, $(R_\kappa/R_{\kappa,\max}) < \mathrm{tol}_\kappa$,
      $(R_f/R_{f,\max}) < \mathrm{tol}_f$
Step 5. Update:
    $\boldsymbol{\sigma}_{n+1} = \boldsymbol{\sigma}^{\mathrm{tr}}_{n+1} + \sum_{A=1}^{3} \sigma_A^{\mathrm{corr}} \boldsymbol{m}^{(A)}$
    $\boldsymbol{\alpha}_{n+1} = \boldsymbol{\alpha}_n + \sum_{B=1}^{2} \Delta\alpha_B (\boldsymbol{m}^{(B)} - \boldsymbol{m}^{(III)})$
    $\kappa_{n+1} = \kappa_n + \Delta\kappa$
    $\gamma_{n+1} = \gamma_n + \Delta\gamma$
    and exit.

Remark 1. The tolerances have to be treated carefully. Because the units of the yield function, and hence the last element of the residual vector, are those of stress squared, the value of that component may differ by several orders of magnitude from the other components. Hence, convergence of the last component can mask lack of convergence by other components, or lack of convergence of the last component may be masked by convergence of the other components. Hence, we check that each component of the residual is converging. Noting that the initial value of the first six components of the residual vector is zero, we

must also ensure that the maximum values of the residual components are compared to as we iterate.

Remark 2. Note that if, in addition to the yield function, the hardening functions depend only on the relative stress, the number of variables in the local Newton-Raphson iteration can be further reduced. If we examine

$$\boldsymbol{\xi}^{\text{corr}} = \boldsymbol{\xi} - \boldsymbol{\xi}^{\text{tr}} = \boldsymbol{\sigma}^{\text{corr}} - \Delta\boldsymbol{\alpha} \tag{2.63}$$

then we can form a residual based on the equation

$$(\boldsymbol{\xi}^{\text{corr}})_A = \Delta\gamma \left(-a^e_{AB} \frac{\partial g}{\partial \xi_B} + (h^\alpha)_A \right) \tag{2.64}$$

The corrections to the stress and back stress can then be calculated once the Newton-Raphson iteration has converged. Unfortunately, this strategy cannot be employed for the current model because one of the factors of $\boldsymbol{h}^\alpha$ is the function $G^\alpha(\boldsymbol{\alpha})$ defined in Eq.(2.36) whose evaluation requires the updated value of the back stress. Fortunately, however, this equation only affects the evolution of $\boldsymbol{\alpha}$ in a scalar fashion, and hence does not affect the spectral directions of the back stress increment.

Remark 3. There is an additional strategy that can be employed to reduce the number of equations. Notice that the last diagonal term of the matrix $D\boldsymbol{R}/D\boldsymbol{X}$, the term $\partial f/\partial\Delta\gamma$, is 0. This can be used to statically condense out the last variable as described in Simo and Hughes [60] and Tamagnini et al. [66].

Remark 4. The algorithm summarized in Box 1 is applicable to isotropic-kinematic hardening models for which elasticity is isotropic and for which the spectral directions of the back stress rate $\dot{\boldsymbol{\alpha}}$ in Eq.(2.35) are the same as those of the relative stress $\boldsymbol{\xi}$. The algorithm is not applicable to integrating models that do not share these features.

2.6 Consistent tangent

The consistent tangent modulus, also referred to as the algorithmic tangent modulus [60], is an essential part of the finite element formulation for the implicit model. For isotropic hardening, Tamagnini et al. [66] and Borja et al. [9] have used spectral directions to form the consistent tangent in a highly efficient, closed-form fashion. However, this formulation

relies on the fact that, for isotropic hardening, the stress and strain have the same spectral directions. This coaxiality is lost in the kinematically hardening case. Recall

$$\begin{aligned} \Delta\boldsymbol{\epsilon} &= \Delta\boldsymbol{\epsilon}^e + \Delta\boldsymbol{\epsilon}^p && (2.65)\\ \Delta\boldsymbol{\epsilon}^e &= (\boldsymbol{c}^e)^{-1}\Delta\boldsymbol{\sigma} && (2.66)\\ \Delta\boldsymbol{\epsilon}^p &= \Delta\gamma\frac{\partial g}{\partial\boldsymbol{\sigma}} && (2.67) \end{aligned}$$

Hence, the elastic strain shares spectral directions with the stress $\boldsymbol{\sigma}$, and the plastic strain increment shares spectral directions with the relative stress $\boldsymbol{\xi}$, as we have seen. In most cases, then, the total strain will share spectral directions with neither.

We form the consistent tangent in a traditional manner. For an implicit Euler scheme, we start with the following system of equations:

$$\mathbf{0} = \left\{ \begin{array}{c} (\boldsymbol{c}^e)^{-1}\boldsymbol{\sigma}_{n+1} - \boldsymbol{\epsilon}_{n+1} + \boldsymbol{\epsilon}^p_n + \Delta\gamma\left(\partial g/\partial\boldsymbol{\sigma}\right)_{n+1} \\ \boldsymbol{q}_{n+1} - \boldsymbol{q}_n - \Delta\gamma(\boldsymbol{h}^q)_{n+1} \\ f\left(\boldsymbol{\sigma}_{n+1}, \boldsymbol{q}_{n+1}\right) \end{array} \right\} \tag{2.68}$$

Differentiating the equations with respect to $\boldsymbol{\epsilon}_{n+1}$ and arranging the results, we can obtain the matrix equations

$$\left[\begin{array}{c} \boldsymbol{I} \\ \mathbf{0} \\ \mathbf{0} \end{array} \right] = \underbrace{\left[\begin{array}{ccc} (\boldsymbol{c}^e)^{-1} + \Delta\gamma\dfrac{\partial^2 g}{\partial\boldsymbol{\sigma}\partial\boldsymbol{\sigma}} & \Delta\gamma\dfrac{\partial^2 g}{\partial\boldsymbol{\sigma}\partial\boldsymbol{q}} & \partial g/\partial\boldsymbol{\sigma} \\ -\Delta\gamma\left(\partial\boldsymbol{h}^q/\partial\boldsymbol{\sigma}\right) & \mathbf{1} - \Delta\gamma\left(\partial\boldsymbol{h}^q/\partial\boldsymbol{q}\right) & -\boldsymbol{h}^q \\ \left(\partial f/\partial\boldsymbol{\sigma}\right)^t & \left(\partial f/\partial\boldsymbol{q}\right)^t & 0 \end{array} \right]}_{\boldsymbol{A}} \left[\begin{array}{c} \partial\boldsymbol{\sigma}/\partial\boldsymbol{\epsilon} \\ \partial\boldsymbol{q}/\partial\boldsymbol{\epsilon} \\ \left(\partial\Delta\gamma/\partial\boldsymbol{\epsilon}\right)^t \end{array} \right] \tag{2.69}$$

The $n+1$ subscripts have been omitted for simplicity. Clearly, then, the consistent tangent $\boldsymbol{c}_{n+1} = \left(\partial\boldsymbol{\sigma}/\partial\boldsymbol{\epsilon}\right)_{n+1}$ is the upper left 6-by-6 submatrix of $\boldsymbol{A}^{-1}$.

As with the integration point algorithm, notice that the system can be statically condensed by taking advantage of the fact that the last diagonal entry is zero. Partitioning the last row and column off the matrix $\boldsymbol{A}$, the equations can be condensed in the same way as those for the local iteration. After some manipulation, the equations become

$$\left[\begin{array}{c} \boldsymbol{I} \\ \boldsymbol{0} \end{array} \right] - \frac{1}{\chi} \left\{ \begin{array}{c} \partial g/\partial \boldsymbol{\sigma} \\ -\boldsymbol{h}^q \end{array} \right\} \left\{ \begin{array}{cc} \left(\dfrac{\partial f}{\partial \boldsymbol{\sigma}}\right)^t & \left(\dfrac{\partial f}{\partial \boldsymbol{q}}\right)^t \end{array} \right\} \boldsymbol{B}^{-1} \left[\begin{array}{c} \boldsymbol{I} \\ \boldsymbol{0} \end{array} \right] = \boldsymbol{B} \left[\begin{array}{c} \partial \boldsymbol{\sigma}/\partial \boldsymbol{\epsilon} \\ \partial \boldsymbol{q}/\partial \boldsymbol{\epsilon} \end{array} \right] \tag{2.70}$$

where

$$\boldsymbol{B} = \left[\begin{array}{cc} (\boldsymbol{c}^e)^{-1} + \Delta\gamma \dfrac{\partial^2 g}{\partial \boldsymbol{\sigma} \partial \boldsymbol{\sigma}} & \Delta\gamma \dfrac{\partial^2 g}{\partial \boldsymbol{\sigma} \partial \boldsymbol{q}} \\ -\Delta\gamma \left(\partial \boldsymbol{h}^q / \partial \boldsymbol{\sigma}\right) & \boldsymbol{1} - \Delta\gamma \left(\partial \boldsymbol{h}^q / \partial \boldsymbol{q}\right) \end{array} \right] \tag{2.71}$$

and

$$\chi = \left\{ \begin{array}{c} \partial g/\partial \boldsymbol{\sigma} \\ -\boldsymbol{h}^q \end{array} \right\} \boldsymbol{B}^{-1} \left\{ \begin{array}{cc} \left(\dfrac{\partial f}{\partial \boldsymbol{\sigma}}\right)^t & \left(\dfrac{\partial f}{\partial \boldsymbol{q}}\right)^t \end{array} \right\} \tag{2.72}$$

This can be rewritten as

$$\left[\begin{array}{c} \partial \boldsymbol{\sigma}/\partial \boldsymbol{\epsilon} \\ \partial \boldsymbol{q}/\partial \boldsymbol{\epsilon} \end{array} \right] = \left(\boldsymbol{B}^{-1} - \frac{1}{\chi} \boldsymbol{B}^{-1} \left\{ \begin{array}{c} \partial g/\partial \boldsymbol{\sigma} \\ -\boldsymbol{h}^q \end{array} \right\} \otimes \boldsymbol{B}^{-t} \left\{ \begin{array}{c} \partial f/\partial \boldsymbol{\sigma} \\ \partial f/\partial \boldsymbol{q} \end{array} \right\} \right) \left[\begin{array}{c} \boldsymbol{I} \\ \boldsymbol{0} \end{array} \right] \tag{2.73}$$

which is very similar to the formulation found in [60] and [4].

Finally, it should be noted that the quantities that populate the matrix $\boldsymbol{A}$ can be easily obtained from quantities that have already been calculated. For example

$$\frac{\partial f}{\partial \boldsymbol{\sigma}} = \frac{\partial f}{\partial \xi_A} \frac{\partial \xi_A}{\partial \boldsymbol{\sigma}} = \frac{\partial f}{\partial \xi_A} \boldsymbol{m}^{(A)} \tag{2.74}$$

and

$$\frac{\partial^2 g}{\partial \boldsymbol{\sigma} \partial \boldsymbol{\sigma}} = \frac{\partial^2 g}{\partial \xi_A \partial \xi_B} \boldsymbol{m}^{(A)} \otimes \boldsymbol{m}^{(B)} \tag{2.75}$$

2.7 Numerical examples

All the examples are run with the associative version of the model. Time step sizes are chosen as large as possible in order to demonstrate reasonably smooth stress-strain curves.

The first example is a one element test with fully constrained degrees of freedom designed to test the local return-mapping algorithm. The example consists of two loadings: uniaxial strain in compression (prescribed displacements in the axial direction and zero displacement in the other directions), followed by constrained shearing. A simple compression simulation would not have adequately tested the ability of the implementation to operate when the spectral directions are changing.

The material properties were fit to Salem Limestone data [20] and are shown in Box 2.

Box 2. Material Properties for Salem Limestone

Young's Modulus $E = 22547$ MPa
Poisson's Ratio $\nu = .2524$ (dimensionless)
$A = 689.2$ MPa
$B = 3.94\text{e}{-4}$ 1/MPa
$C = 675.2$ MPa
$\theta = 0.0$ radians
$R = 28.0$ (dimensionless)
$\kappa_0 = -8.05$ MPa
$W = .08$ (dimensionless)
$D_1 = 1.47\text{e-}3$ 1/MPa
$D_2 = 0.0$ 1/MPa^2
$c^\alpha = 1\text{e}5$ MPa
$\psi = 1.0$ (dimensionless)
$N = 6.0$ MPa

The stress-strain response is shown in Fig. 2.5. During the first loading increment, the axial response begins as elastic and then becomes plastic, while the shear stress and strain remain zero. During the second phase, the shear response is plastic, and the axial stress drops. The stress paths for the compression and shear phases are shown in Figs. 2.6 and 2.7 on the $\sqrt{J_2}$ vs. I_1 and $\sqrt{J_2^\xi}$ vs. I_1 planes, respectively. Recall from Eq.(2.30) that the yield function is a function of the invariants I_1, J_2^ξ, and J_3^ξ. When plotting stress paths in the $\sqrt{J_2}$ vs. I_1 plane, we expect the stress path to appear to deviate from the yield surface, whereas in fact the stress path moves out of plane because the principal directions of $\boldsymbol{\xi}$ are changing. We plot the stress path in the $\sqrt{J_2}$ vs. I_1 plane in order to show translation of the yield

surface due to evolving $\boldsymbol{\alpha}$. Plotting the stress path in the $\sqrt{J_2^{\xi}}$ vs. I_1 plane, however, we expect the stress path to remain on the yield surface, assuming $\psi = 1$ (i.e., no dependence on J_3^{ξ}), because even though the principal directions of $\boldsymbol{\xi}$ are changing, J_2^{ξ} is invariant to these changes.

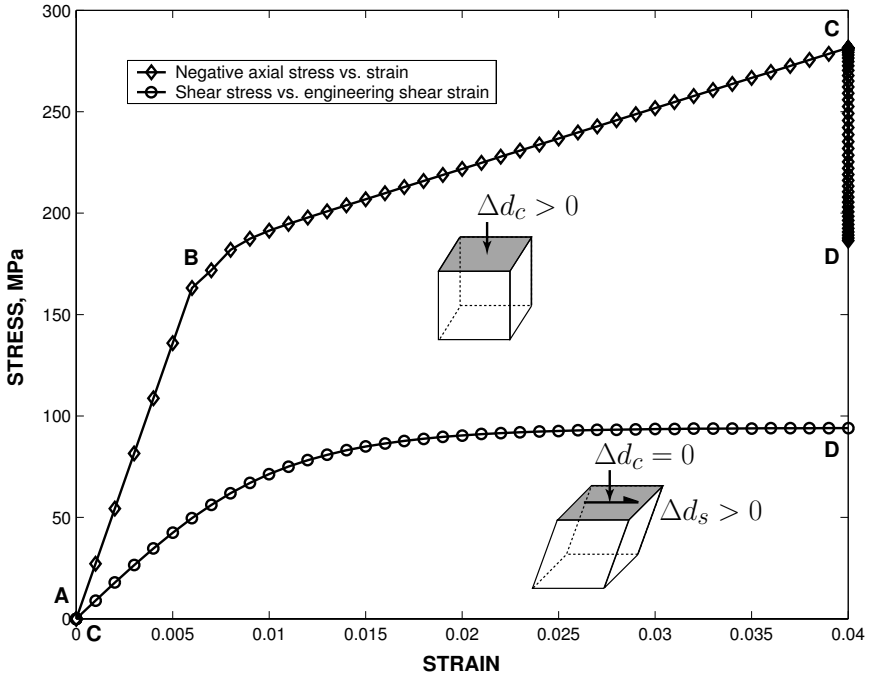

Figure 2.5. Stress-strain response for uniaxial strain in compression followed by constrained shear test. Shaded face has prescribed compression displacement d_c and shear displacement d_s, while all other faces are fixed except during shear. Letters A through D indicate the loading path. Note that C and D on the compression curve appear on a vertical line since during the shear phase there is no displacement in the compression direction, i.e. $\Delta d_c = 0$, although the axial stress drops.

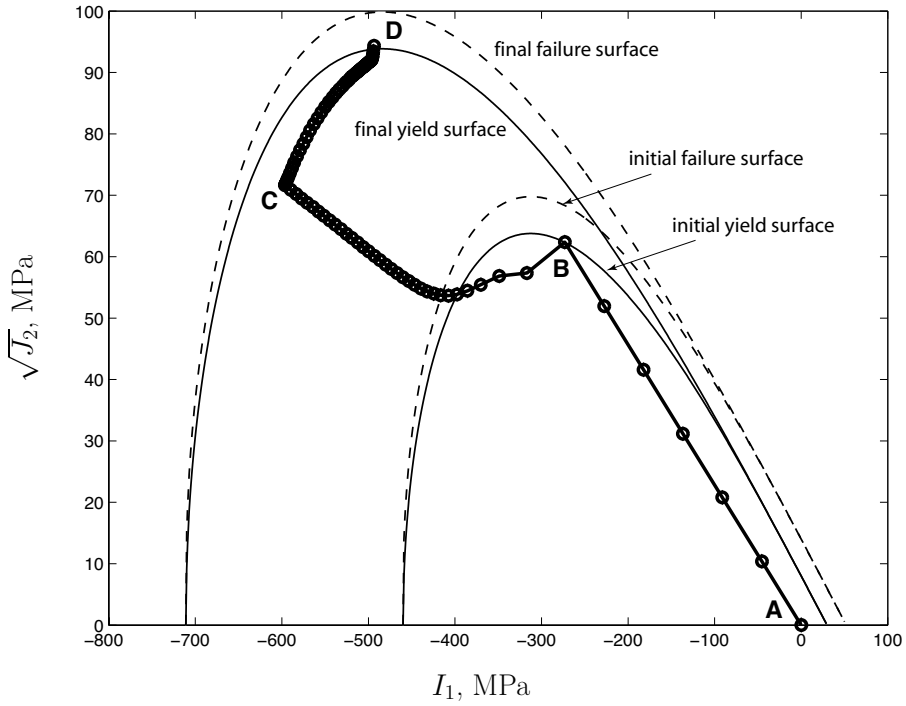

Figure 2.6. Stress path in meridional stress space $\sqrt{J_2}$ vs. I_1 for compression and shear phases of uniaxial strain and constrained shear problem. Initial and final surfaces for compression and shear phases shown. The letters indicate points on the stress path that correspond with points on the stress-strain curve in Fig. 2.5.

Clearly, the post-localization model has not been implemented here, as the strain extends to four percent. While the results are consistent with the model as implemented, they do not capture the physical behavior of the material as it is deformed to larger strains. The results underscore the need to add a localization capability to this implementation of the model.

We check the convergence of the algorithm both at the first plastic step and the first step of the shear part of the test, where the spectral directions change. The resulting norm of the residual vector for both cases is plotted in Fig. 2.8 and also shown in Table 2.1. Quadratic convergence is observed. In this problem, quadratic convergence can be observed in each component of the residual vector. As discussed earlier, because of the nature of the residual vector, convergence of each component is checked. In some other problems not shown here, one larger component may hamper the quadratic convergence of other components, but overall quadratic convergence is still observed in all the examples we have run.

For the second example, we verify that the consistent tangent is calculated correctly such that quadratic convergence is exhibited. To do this, we run the same problem we did to verify the stress point algorithm in the first example, but allow free movement in the orthogonal direction that does not have prescribed axial or shear displacements. Essentially,

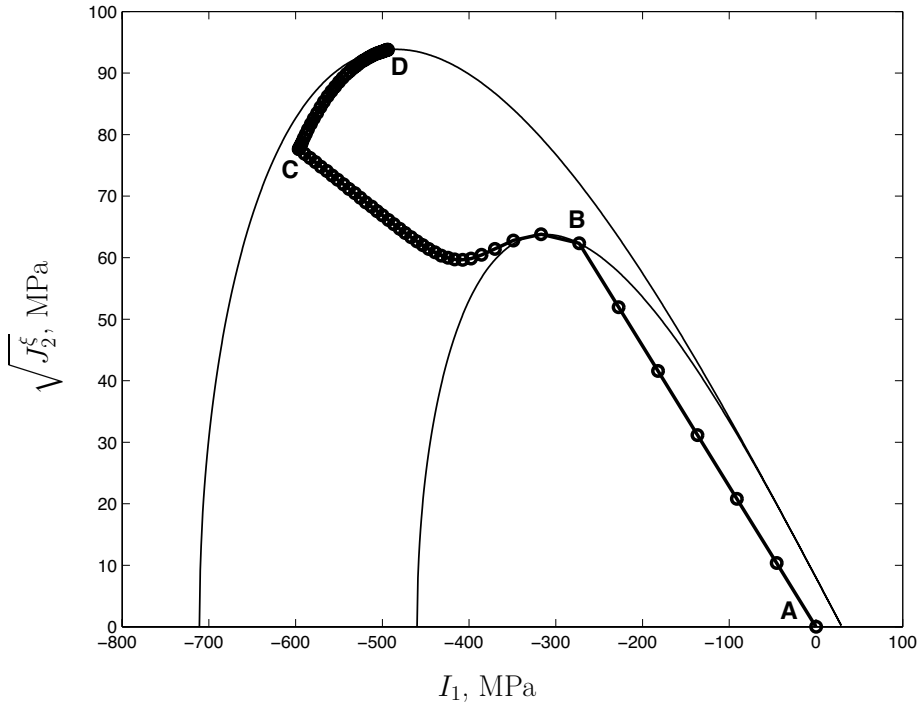

Figure 2.7. Stress path in meridional stress space $\sqrt{J_2^\xi}$ vs. I_1 for compression and shear phases of uniaxial strain and constrained shear problem. Initial and final yield surfaces shown. The letters indicate points on the stress path that correspond with points on the stress-strain curve in Fig. 2.5.

this is a plane stress version of the uniaxial strain and constrained shear problem run for the first example. This problem is run in a fully three-dimensional setting to give the problem unconstrained degrees of freedom, as are all numerical examples in this paper. The stress-strain response is shown in Fig. 2.9. The stress paths for compression and shear phases are shown in Figs. 2.10 and 2.11 on the $\sqrt{J_2}$ vs. I_1 and $\sqrt{J_2^\xi}$ vs. I_1 planes, respectively. Again, the test has two parts, compression and shear, and we verify that the global residual vector converges quadratically (cf. Fig. 2.12 and Table 2.2).

iteration number	residual norm - compression step	residual norm - shear step
1	4.127771E + 00	8.102731E + 01
2	1.088910E − 03	2.699950E − 01
3	3.771775E − 10	2.897466E − 06
4	5.911716E − 12	1.346052E − 10

Table 2.1. Convergence of integration point algorithm: norm of the residual vector.

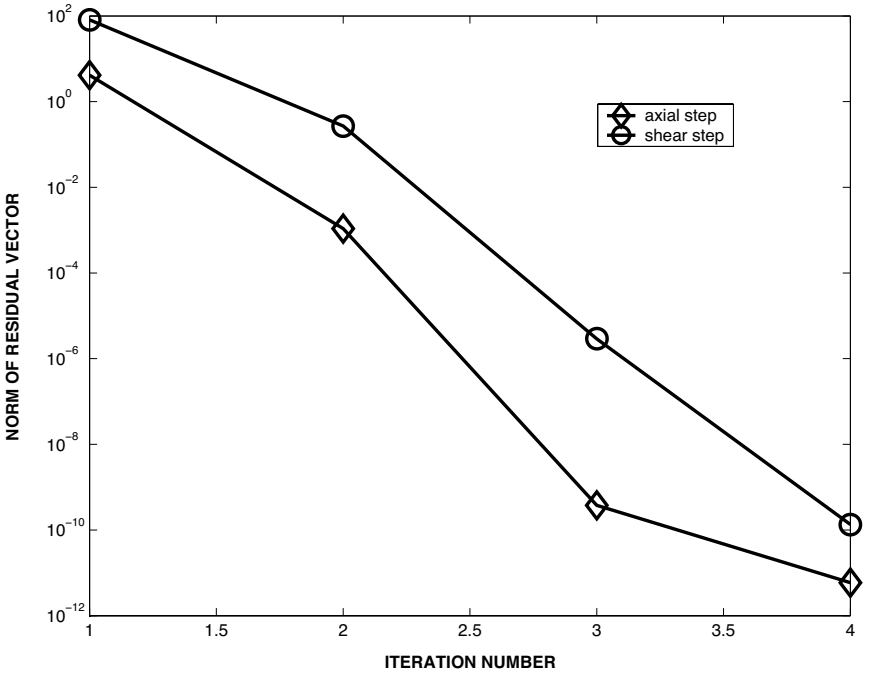

Figure 2.8. Residual norm per iteration for the first plastic step in both the compressive portion and shear portion of the uniaxial strain test. Quadratic convergence is observed.

The third example is a comparison between the implicit implementation and an existing explicit (forward Euler) implementation of the same model [21] [20]. The problem is a plane strain, one-element, loading/unloading problem to 2.5% compressive strain. A 20 MPa confining pressure is applied. The explicit algorithm was run in 5000 steps to achieve stability, while the implicit needed only 80 steps to achieve a smooth stress-strain curve. As Fig. 2.13 shows, the results are comparable. The material properties are the same as for the first example.

Next, we continue cycling this loading, from 0 to -2.5%, to verify that the model exhibits

iteration number	residual norm - compression step	residual norm - shear step
1	5.0010E + 00	5.2760E − 01
2	1.3852E + 00	4.0716E − 02
3	1.9048E − 01	2.7998E − 04
3	4.8349E − 03	1.3410E − 08
4	3.2879E − 06	4.4431E − 15
5	1.5667E − 12	

Table 2.2. Convergence of gobal algorithm: norm of the global residual vector.

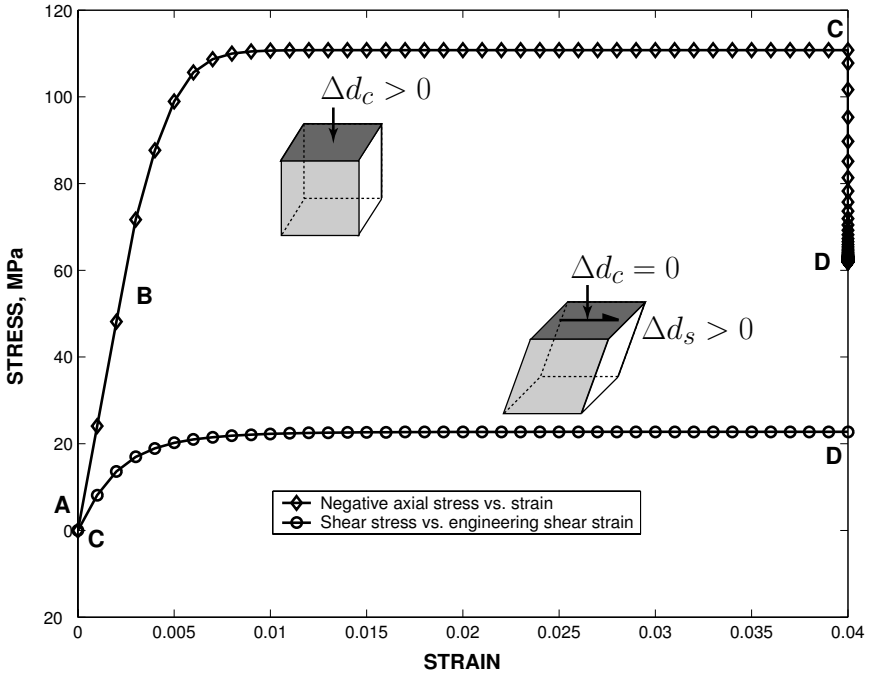

Figure 2.9. Stress-strain response for element in plane stress compression and constrained shear. Compression displacement d_c and shear displacement d_s applied to darker face, while the lighter face is free. The unshaded faces have fixed normal displacements, except during shear. Letters A through D indicate points on the stress-strain curve that correspond to letters on the stress paths in Figs. 2.10 and 2.11. Note that C and D on the compression curve appear on a vertical line since during the shear phase there is no displacement in the compression direction, i.e. $\Delta d_c = 0$, although axial stress decreases.

a Bauschinger effect. The material data for this model suggests a Baushinger effect for this Limestone, which is observed in Fig. 2.14. The stress path is shown in Figs. 2.15 and 2.16 on the $\sqrt{J_2}$ vs. I_1 and $\sqrt{J_2^\xi}$ vs. I_1 planes, respectively.

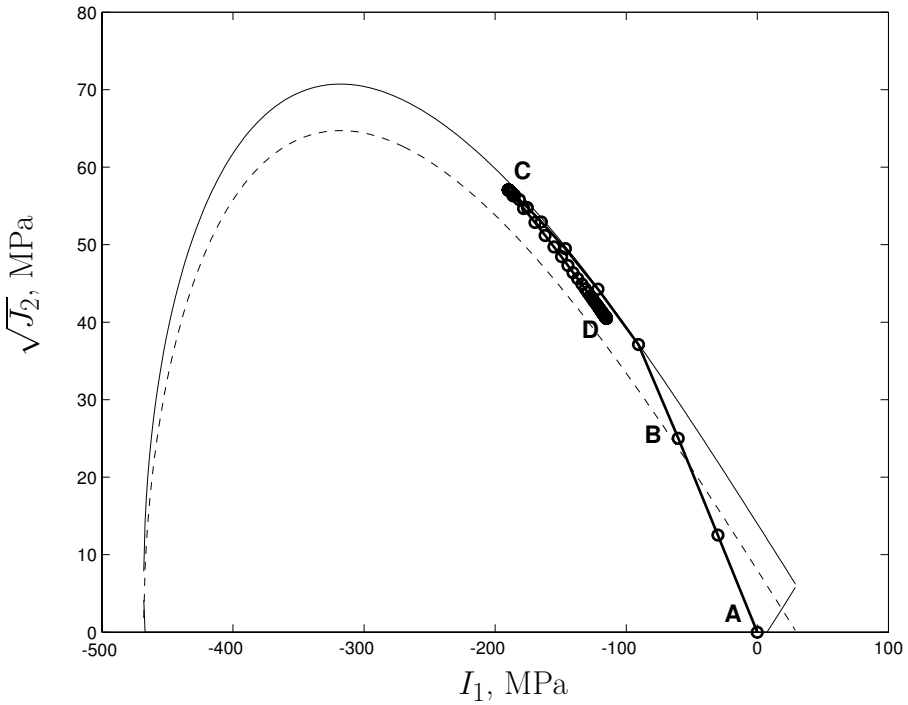

Figure 2.10. Stress path in meridional stress space $\sqrt{J_2}$ vs. I_1 for compression and shear phases of plane stress problem. The letters indicate points on the stress path that correspond with points on the stress-strain curve in Fig. 2.9. The stress path appears to deviate from the yield surface, but it is actually moving out of plane from the $\sqrt{J_2}$ vs. I_1 plane as the principal directions of $\boldsymbol{\xi}$ change. The dashed curve shows the initial yield surface and the solid curve the translated yield surface, which at this stage is the same as the failure surface.

Finally, to capture the difference in triaxial extension strength versus triaxial compression strength, new material properties are required. The material properties used in the previous three examples were set for $\psi = 1$, indicating no difference in strength between triaxial extension and compression. New material properties, also fit for a limestone are given in Box 3.

Box 3. Material properties for limestone accounting for difference in triaxial extension vs. compression strength.

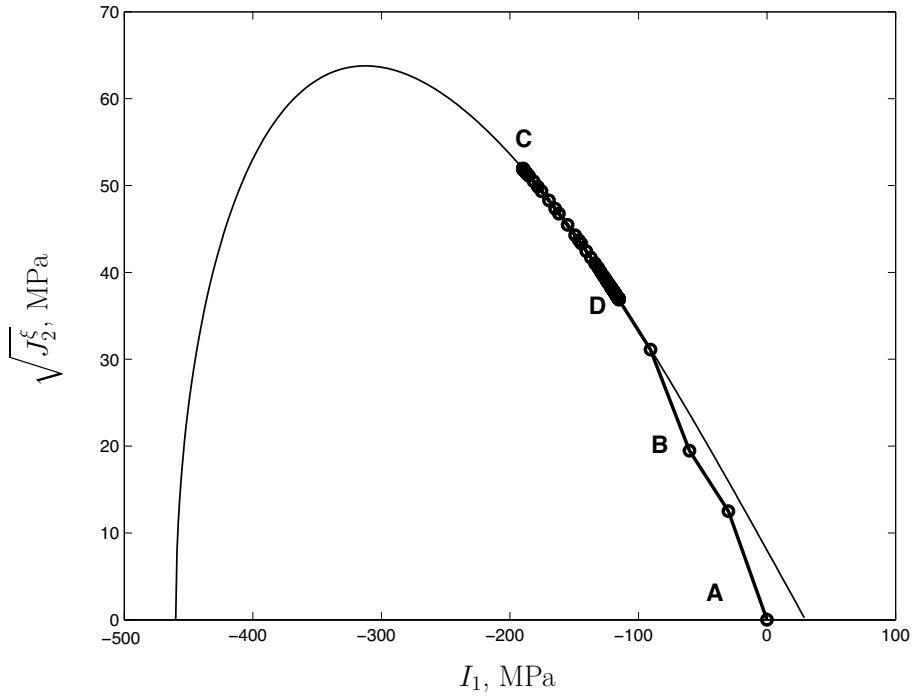

Figure 2.11. Stress path in meridional stress space $\sqrt{J_2^\xi}$ vs. I_1 for compression and shear phases of plane stress problem. The letters indicate points on the stress path that correspond with points on the stress-strain curve in Fig. 2.9. The final yield surface is shown. As opposed to Fig.2.10, in this figure the stress path remains on the yield surface because J_2^ξ and I_1 are the invariants in the yield function. The relative stress $\boldsymbol{\xi}$ is embedded in J_2^ξ, and so even as its principal directions change, J_2^ξ is invariant to these changes. The kink at point B along the stress path is due to the backstress $\boldsymbol{\alpha}$ increasing at a faster rate than the deviatoric stress $\boldsymbol{s}$ during the first plastic time step, hence resulting in an apparent softer response at point B.

Young's Modulus E = 22547 MPa
Poisson's Ratio ν = .2524 (dimensionless)
A = 843.0 MPa
B = 2.73e-4 1/MPa
C = 822.0 MPa
θ = 0.0 radians
R = 28.0 (dimensionless)
κ_0 = -8.05 MPa
W = .08 (dimensionless)
D_1 = 1.47e-3 1/MPa
D_2 = 0.0 1/MPa^2
c^α = 1e3 MPa
ψ = 0.8 (dimensionless)
N = 8.0 MPa

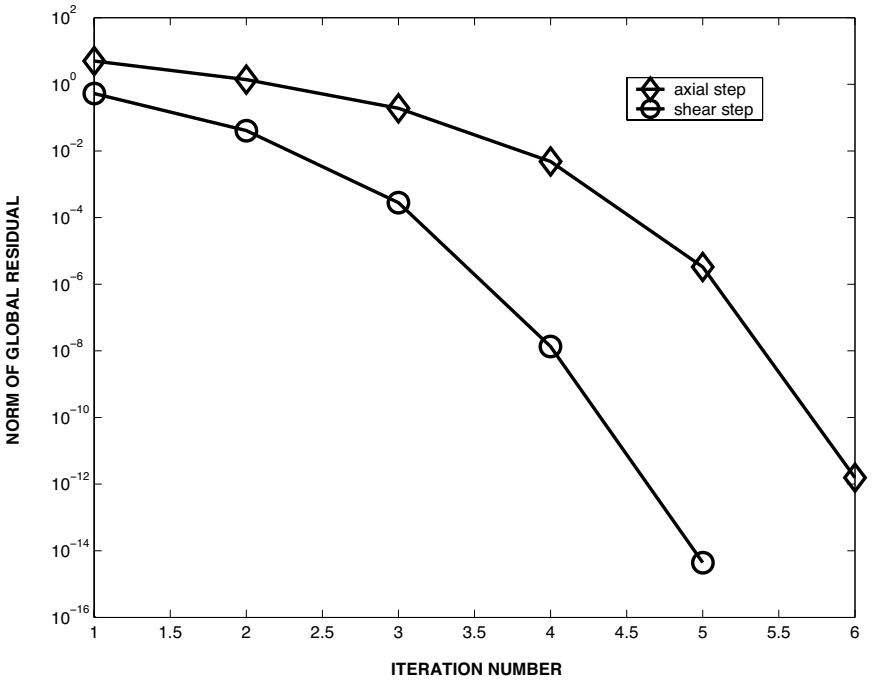

Figure 2.12. Residual norm per iteration for the first plastic step in both the compression portion and shear portion of the plane stress test for the global algorithm. Quadratic convergence is observed.

These properties were used in two tests. Both tests were run at zero mean stress with the stress tensor

$$\boldsymbol{\sigma} = \begin{bmatrix} \sigma & 0 & 0 \\ 0 & -\sigma/2 & 0 \\ 0 & 0 & -\sigma/2 \end{bmatrix} \tag{2.76}$$

For the triaxial extension test, σ is positive, while it is negative for the triaxial compression test. The results in Fig. 2.17 show that the material yields sooner and undergoes more plastic deformation in the triaxial extension case. Figures 2.18 and 2.19 show how the stress paths in the π-plane meet and translate the yield surfaces for triaxial extension and compression loadings.

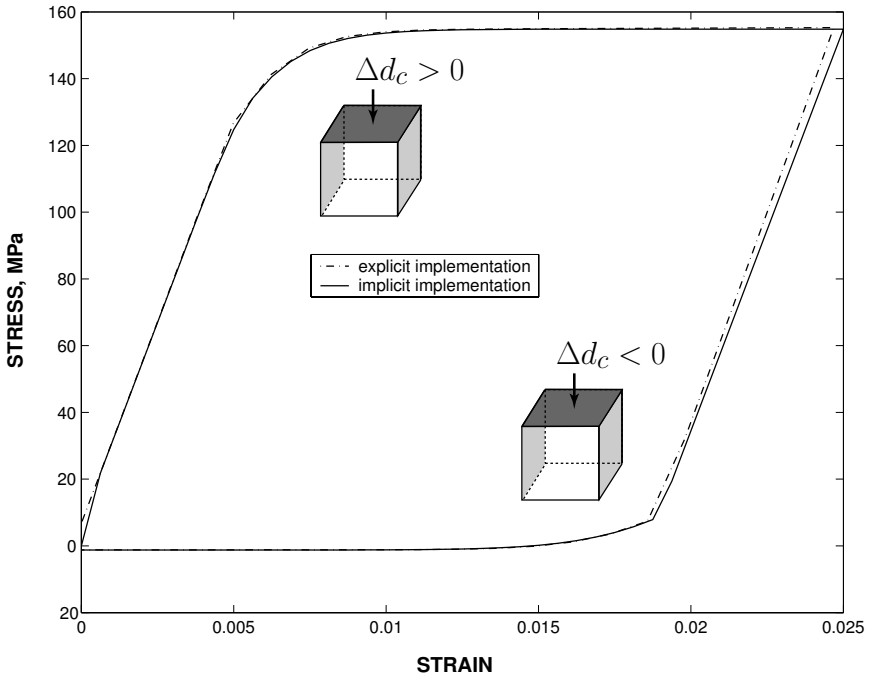

Figure 2.13. Comparison between implicit (this paper) and explicit [21] implementations of the model. Plane strain compression and unloading with 20 MPa confining pressure. Compression displacement d_c applied to darker face, while confining pressure is applied to lighter faces. The unshaded faces have fixed normal displacements.

2.8 Conclusions

The chapter reviewed a model for porous geomaterials such as limestones, sandstones, and concrete, that includes both isotropic and kinematic hardening. The chapter presented an algorithm for the implicit integration of models that have kinematic hardening or combined isotropic and kinematic hardening using the spectral decomposition of the relative stress. To our knowledge, the algorithm is novel. The local return mapping algorithm is an extension of algorithms used for isotropically hardening models as shown in [58] [9] [66]. The spectral decomposition technique reduces the number of function evaluations, which can be quite costly for even moderately advanced constitutive models, as well as reduces the size of the system of equations to be solved.

The consistent tangent has been implemented in a standard way [59] [4], noting that the quantities needed to form the generalized compliance can be computed from the spectral values without any additional function evaluations. However, the efficient methods used to compute the consistent tangent in the isotropically hardening case [42] [9] [66] cannot be used for the kinematically hardening case since the stress and strain are not coaxial.

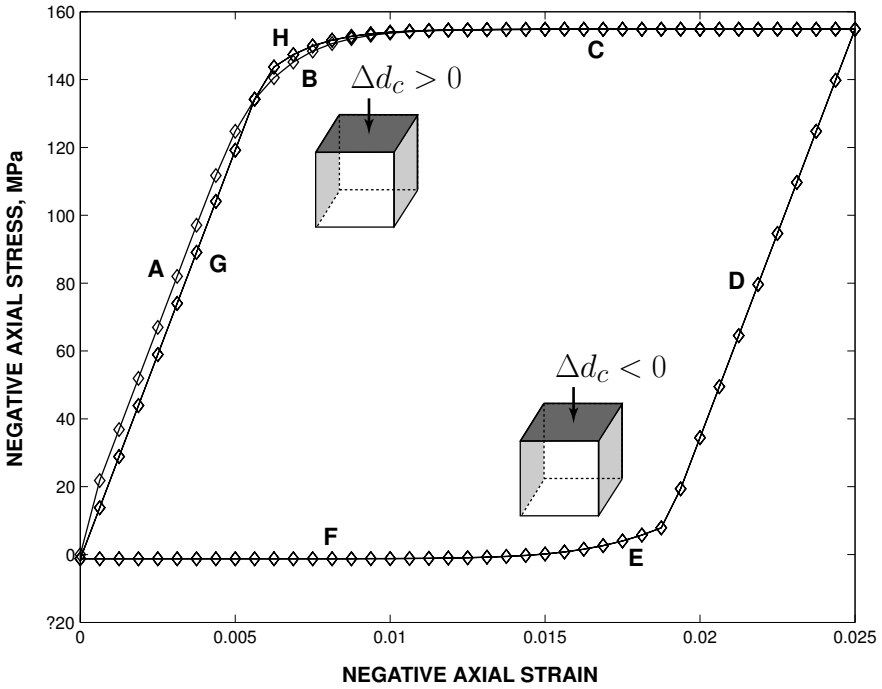

Figure 2.14. The Bauschinger, or Masing, effect captured by the model. Cyclic plane strain compression with 20 MPa confining pressure. Compression displacement d_c applied to darker face, while confining pressure is applied to lighter faces. The unshaded faces have fixed normal displacements. The letters on the stress-strain curve correspond with the stress paths in Figs. 2.15 and 2.16.

Numerical examples show that both the local and global iterations exhibit quadratic convergence. Also, these examples show how the model can be used to capture some of the behaviors common to geomatrials, including strain hardening, a Bauschinger effect, and differences in triaxial extension versus compression strength.

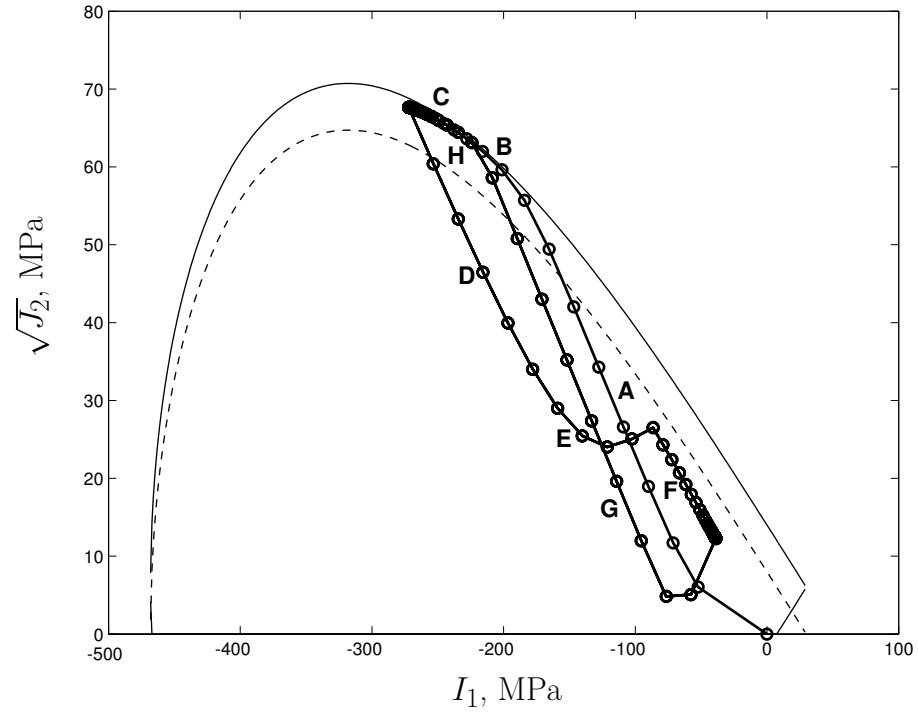

Figure 2.15. Stress path in meridional stress space $\sqrt{J_2}$ vs. I_1 for compression and shear phases of plane stress problem. The letters indicate points on the stress path that correspond with points on the stress-strain curve in Fig. 2.14. The stress path appears to deviate from the yield surface at F along the stress path, but it is actually moving out of plane from the $\sqrt{J_2}$ vs. I_1 plane as the principal directions of $\boldsymbol{\xi}$ change. The dashed curve is the initial yield surface and the solid curve the final, translated yield surface. The initial kink in the stress path along A is due to simultaneous application of confining pressure and compression displacement d_c in the first time step.

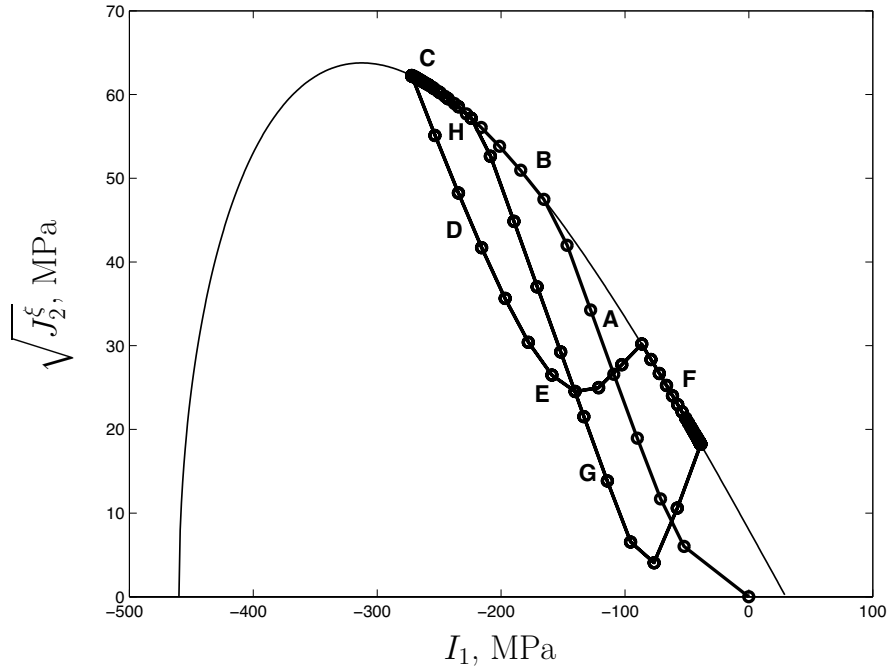

Figure 2.16. Stress path in meridional stress space $\sqrt{J_2^\xi}$ vs. I_1 for compression and shear phases of plane stress problem. The letters indicate points on the stress path that correspond with points on the stress-strain curve in Fig. 2.14. As opposed to Fig.2.15, in this figure the stress path remains on the yield surface because J_2^ξ and I_1 are invariants in the yield function, and J_2^ξ is invariant to changing principal directions of $\boldsymbol{\xi}$.

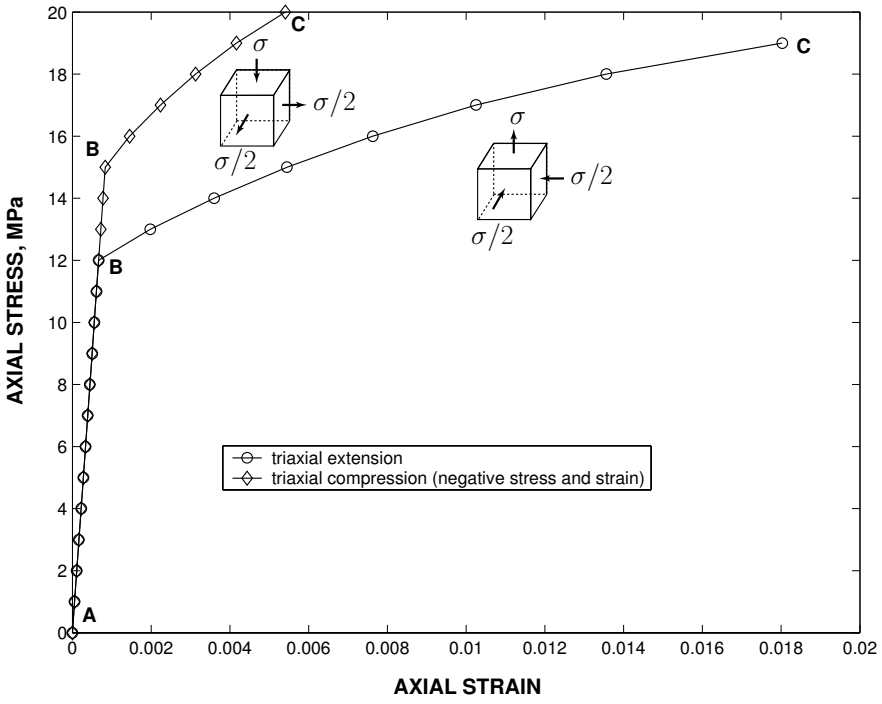

Figure 2.17. Comparison of material response in trixial extension vs triaxial compression at zero mean stress. Axial stresses are the principal stresses largest in magnitude. The letters denote points on the stress-strain curves that correspond to points on the stress paths in Figs. 2.18 and 2.19.

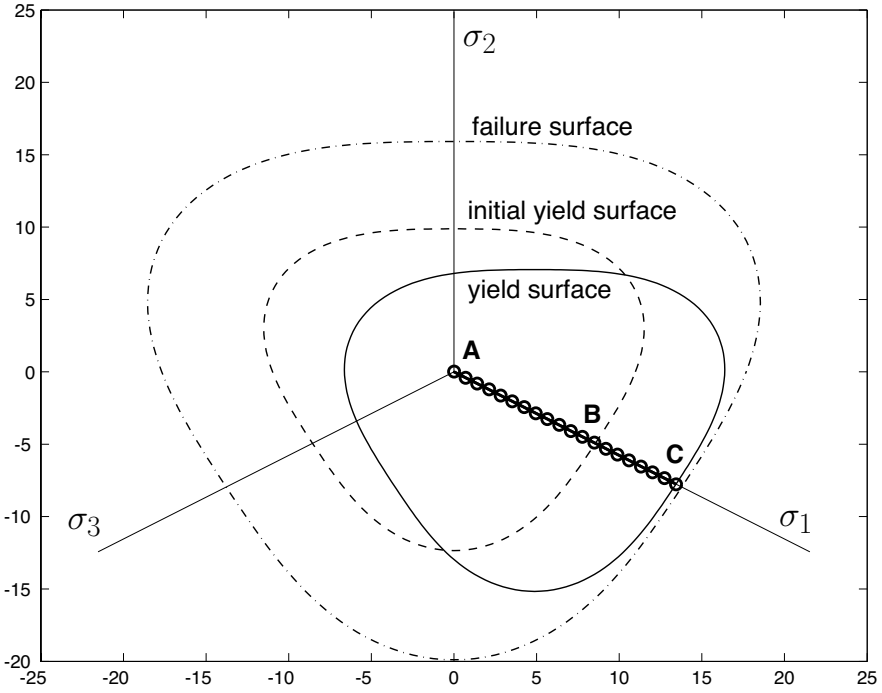

Figure 2.18. Stress path in π-plane for triaxial extension showing intersection with initial yield surface and stopping at final yield surface. The failure surface is shown for reference. The letters denote points on the stress path that correspond with points on the stress-strain curve in Fig. 2.17.

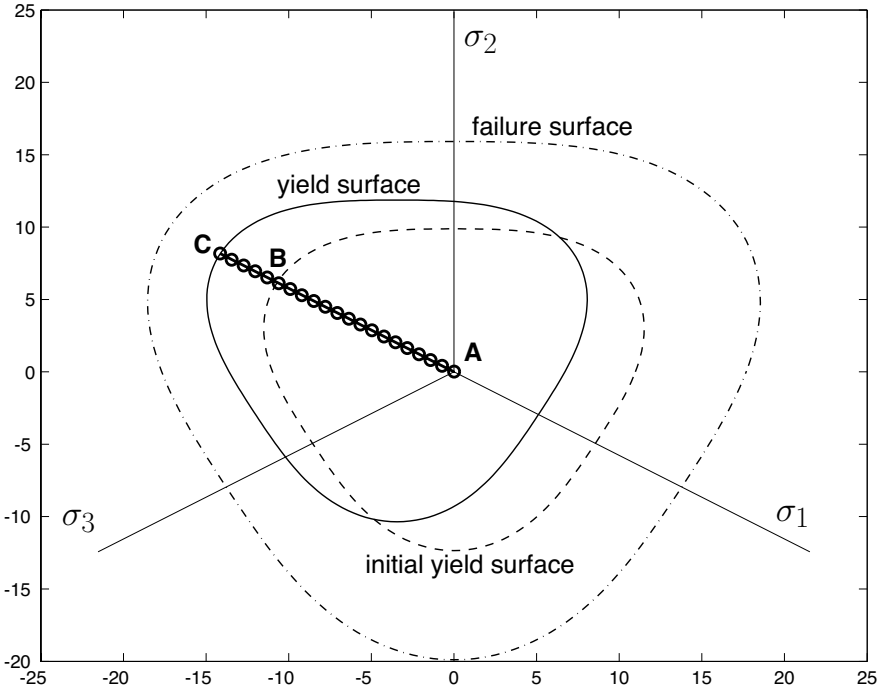

Figure 2.19. Stress path in π-plane for triaxial compression showing intersection with initial yield surface and stopping at final yield surface. The failure surface is shown for reference. The letters denote points on the stress path that correspond with points on the stress-strain curve in Fig. 2.17.

This page intentionally left blank.

Chapter 3

Bifurcation conditions for Sandia GeoModel

Authors: R.A. Regueiro, C.D. Foster, A.F. Fossum, R.I. Borja

Portions of this chapter may be found in [48] and [49].

3.1 Introduction

Localized deformation such as shear bands, compaction bands, dilation bands, combined shear-compaction or shear-dilation bands, fractures, and joint slippage are commonly found in geomaterials. These localized deformations can be triggered by either material inhomogeneities such as joint sets in rocks, inhomogeneous stress resulting from boundary conditions such as friction at end platens in a confined compression test, or by some microstructurally driven material instability. We can account for material inhomogeneities by constitutive modeling in conjunction with a numerical simulation method such as the finite element method. Significant material inhomogeneities such as strata and joint sets can be meshed discretely, assigning different material properties for each spatial region of the finite element mesh, or they can be incorporated in an average sense into a continuum constitutive model via directional structure/anisotropy tensors or the like. Either way, depending on boundary and loading conditions, the material deformation response predicted by the constitutive model could become mathematically unstable. This mathematical instability could be made to coincide with the natural material instability observed in the field or laboratory. The most straightforward way to do this is to endow the constitutive model with as much material characterization and representative deformation response that is deemed significant for the problem of interest. For example, if joint sets are plentiful and dominate the material deformation response, they must be represented in the constitutive model. Depending on

the boundary and loading conditions, the model must predict the onset of gross localized deformation resulting from activity of certain critical joint sets. In essence, the ability of a continuum constitutive model to predict material instability in the form of localized deformation is only as good as the model's sophistication in terms of representing material behavior. Some questions we should ask when choosing and developing constitutive models for geomaterials are: Is the material isotropic or anisotropic elastically and/or plastically? Is the material temperature and rate-sensitive? Are joint sets or other in-situ material inhomogeneities prominent?

Given a relatively sophisticated continuum constitutive model for geomaterials, this chapter focuses on determining stress states at which the constitutive model predicts mathematical instabilities. With regard to modeling material deformation response after an instability is detected, such as transition of continuous rock-like material to fragmented rock material, this instability will be referred to as a bifurcation in material response. Developing a post-bifurcation constitutive model and numerical implementation, whether via the finite element method or a meshfree method, is the next step in modeling material failure in geomaterials and will be discussed in Chapters 4, 5, and 6.

The bifurcation analysis assumes strong (jump in displacement) and weak (jump in strain) discontinuity kinematics for both rate insensitive and rate sensitive forms of the constitutive model. For the rate insensitive form, different bifurcation conditions result for strong and weak discontinuities as well as whether bifurcation is continuous or discontinuous. Continuous bifurcation assumes that at the instant of bifurcation there is plastic loading outside the discontinuity as well as within/on it [50]. Discontinuous bifurcation assumes there is elastic unloading outside the discontinuity and plastic loading within/on the discontinuity. Rice and Rudnicki [50] analyzed continuous and discontinuous bifurcation for weak discontinuities in the context of rate insensitive non-associative plasticity. We will extend this analysis to strong discontinuities and rate sensitivity and with future numerical examples will address specifically the effects of the third invariant and backstress on bifurcation. For weak discontinuity, we find there is a difference between continuous and discontinuous bifurcation conditions, whereas for strong discontinuity, there is no difference. We solve for the unit normal $\boldsymbol{n}$ to a discontinuity interface that satisfies the loss of ellipticity condition, the determinant of the acoustic tensor $\boldsymbol{A}$ is zero ($\det\boldsymbol{A} = 0$) [51], which results from the condition that traction is continuous across the discontinuity. This bifurcation condition in essence tells us that at a given stress state a discontinuity is admissible in our material body. This condition is necessary but not sufficient for the discontinuity to appear. It is well known in the literature that for rate sensitive plasticity, large positive values of viscosity preclude loss of ellipticity (i.e., $\det\boldsymbol{A} > 0$), unless the viscosity is small enough such that the model is nearly rate insensitive. Hence, loss of ellipticity is not a meaningful bifurcation condition for a rate sensitive geomaterial model. This requires us to determine a physically meaningful bifurcation condition for the rate sensitive form of the model since we know from laboratory tests and field evidence that failure occurs for rate sensitive materials. In addition, we ques-

tion whether $\det \boldsymbol{A} = 0$ for the rate insensitive form is a physically meaningful bifurcation condition because it depends on a continuum constitutive model and on a fit of its material parameters to data determined from homogeneously deforming experimental specimens. It seems physically meaningful to have similar bifurcation criteria for both rate insensitive and rate sensitive forms of the model. This chapter, however, focuses on bifurcation analysis of rate insensitive and sensitive forms of a geomaterial constitutive model. Future work will revisit this issue.

Throughout the chapter we assume small deformations and rotations. Symbolic notation is used for clearer presentation, such as the inner product of two second order tensors $(\boldsymbol{a}\cdot\boldsymbol{b})_{ik} = a_{ij}b_{jk}$, the contraction of two tensors $\boldsymbol{a} : \boldsymbol{b} = a_{ij}b_{ij}$, or the dyadic product $(\boldsymbol{a}\otimes\boldsymbol{b})_{ijkl} = a_{ij}b_{kl}$. Tensor operators are used such as the trace operator $\mathrm{tr}\boldsymbol{a} = a_{ii}$, deviatoric operator $\mathrm{dev}\boldsymbol{a} = \boldsymbol{a} - (\mathrm{tr}\boldsymbol{a}/3)\boldsymbol{1}$, symmetric gradient $(\boldsymbol{\nabla}^s\boldsymbol{v})_{ij} = (v_{i,j} + v_{j,i})/2$, and divergence $(\boldsymbol{\nabla}\cdot\boldsymbol{a})_i = a_{ij,j}$.

3.2 Kinematics and governing equations for weak and strong discontinuities

For **weak discontinuities**, we assume a planar band with thickness h, which is small relative to the size of the body (0.1% or 1%), such that $1/h$ is a large number but remains bounded. The strain rate assuming small strains is written as [5]

$$\dot{\boldsymbol{\epsilon}} \;=\; \begin{cases} \dot{\boldsymbol{\epsilon}}^1 \;=\; \dot{\boldsymbol{\epsilon}}^0 \;+\; \frac{1}{h}\mathrm{sym}([\![\boldsymbol{v}]\!]\otimes\boldsymbol{n}) & \in \mathcal{B}^h \\ \dot{\boldsymbol{\epsilon}}^0 & \in \Omega\backslash\bar{\mathcal{B}}^h \end{cases} \tag{3.1}$$

where $\dot{\boldsymbol{\epsilon}} = \boldsymbol{\nabla}^s\boldsymbol{v}$, superscript 1 denotes just inside the band and 0 denotes just outside the band (say, across $\mathcal{S}^h_+$), $[\![\boldsymbol{v}]\!] = \boldsymbol{v}_+ - \boldsymbol{v}_-$ is the jump in velocity across the band, and $\boldsymbol{n}$ is the unit normal to the band (cf. Fig.3.1).

The local form of quasi-static, isothermal equilibrium for a body Ω with weak discontinuity is written as follows

$$\begin{aligned} \boldsymbol{\nabla}\cdot\boldsymbol{\sigma} + \boldsymbol{b} &= \boldsymbol{0} \quad \text{in } \Omega \\ \boldsymbol{\sigma}\cdot\boldsymbol{\nu} &= \boldsymbol{t}^\sigma \quad \text{on } \Gamma_t \\ \boldsymbol{u} &= \boldsymbol{g} \quad \text{on } \Gamma_g \\ [\![\boldsymbol{\sigma}]\!]\cdot\boldsymbol{n}_+ &= \boldsymbol{0} \quad \text{across } \mathcal{S}^h_+ \\ [\![\boldsymbol{\sigma}]\!]\cdot\boldsymbol{n}_- &= \boldsymbol{0} \quad \text{across } \mathcal{S}^h_- \end{aligned} \tag{3.2}$$

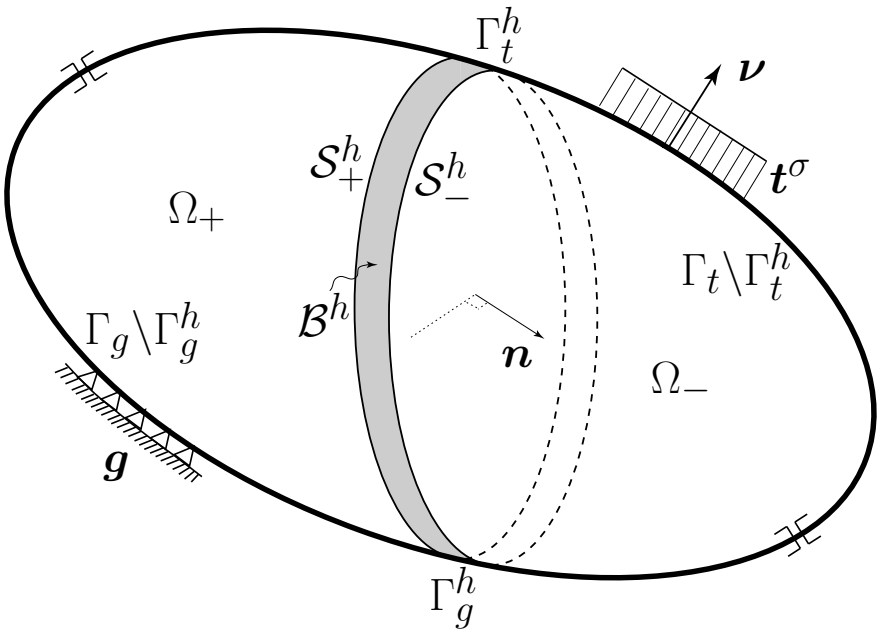

Figure 3.1. Body $\bar{\Omega}$ with planar weak discontinuity $\mathcal{B}^h$ ($\Omega = \Omega_+ \cup \Omega_- \cup \mathcal{B}^h$, $\Gamma = \Gamma_t \cup \Gamma_g \cup \mathcal{S}_-^h \cup \mathcal{S}_+^h$, $\bar{\mathcal{B}}^h = \mathcal{B}^h \cup \Gamma_t^h \cup \Gamma_g^h \cup \mathcal{S}_-^h \cup \mathcal{S}_+^h$, $\bar{\Omega} = \Omega \cup \Gamma$).

where $\boldsymbol{\sigma}$ is the Cauchy stress, $\boldsymbol{b}$ is the prescribed body force, $\boldsymbol{\nu}$ is the unit normal to Γ_t, $\boldsymbol{n}_+ = \boldsymbol{n}_- = \boldsymbol{n}$ is the unit normal to $\mathcal{S}_+^h$ and $\mathcal{S}_-^h$ since the band is assumed planar, $\boldsymbol{t}^\sigma$ is the prescribed traction, $\boldsymbol{g}$ is the prescribed displacement, and $[\![\boldsymbol{\sigma}]\!]$ denotes the jump in stress across $\mathcal{S}_+^h$ or $\mathcal{S}_-^h$ (i.e., $[\![\boldsymbol{\sigma}]\!] = \boldsymbol{\sigma}^1 - \boldsymbol{\sigma}^0$).

The variational form of quasi-static equilibrium, using the local form as a point of departure, then may be written as follows

$$\begin{aligned}\int_\Omega \boldsymbol{\nabla}^s \boldsymbol{\eta} : \boldsymbol{\sigma}\, d\Omega \;\; = \;\; & \int_\Omega \boldsymbol{\eta} \cdot \boldsymbol{b}\, d\Omega \; + \; \int_{\Gamma_t} \boldsymbol{\eta} \cdot \boldsymbol{t}^\sigma\, d\Gamma \\ & + \int_{\mathcal{S}_+^h} \boldsymbol{\eta} \cdot ([\![\boldsymbol{\sigma}]\!] \cdot \boldsymbol{n})\, d\Gamma \\ & + \int_{\mathcal{S}_-^h} \boldsymbol{\eta} \cdot ([\![\boldsymbol{\sigma}]\!] \cdot \boldsymbol{n})\, d\Gamma \end{aligned} \tag{3.3}$$

where $\boldsymbol{\eta} = \delta \boldsymbol{u}$ is the weighting function and first variation of $\boldsymbol{u}$. The traction continuity condition $[\![\boldsymbol{\sigma}]\!] \cdot \boldsymbol{n} = \boldsymbol{0}$ across $\mathcal{S}_+^h$ and $\mathcal{S}_-^h$ for a body with weak discontinuities will be used to determine bifurcation.

For **strong discontinuities**, a spatial jump in velocity $[\![\boldsymbol{v}]\!]$ across $\mathcal{S}$ leads to a singular strain rate at $\mathcal{S}$ as [62]

$$\dot{\boldsymbol{\epsilon}} \;=\; \begin{cases} \dot{\boldsymbol{\epsilon}}^1 \;=\; \dot{\boldsymbol{\epsilon}}^0 \,+\, \mathrm{sym}([\![\boldsymbol{v}]\!] \otimes \boldsymbol{n})\, \delta_{\mathcal{S}} & \in \mathcal{S} \\ \dot{\boldsymbol{\epsilon}}^0 & \in \Omega \backslash \mathcal{S} \end{cases} \tag{3.4}$$

where $\delta_{\mathcal{S}}$ is the Dirac-delta function at the discontinuity surface $\mathcal{S}$ (cf. Fig.3.2).

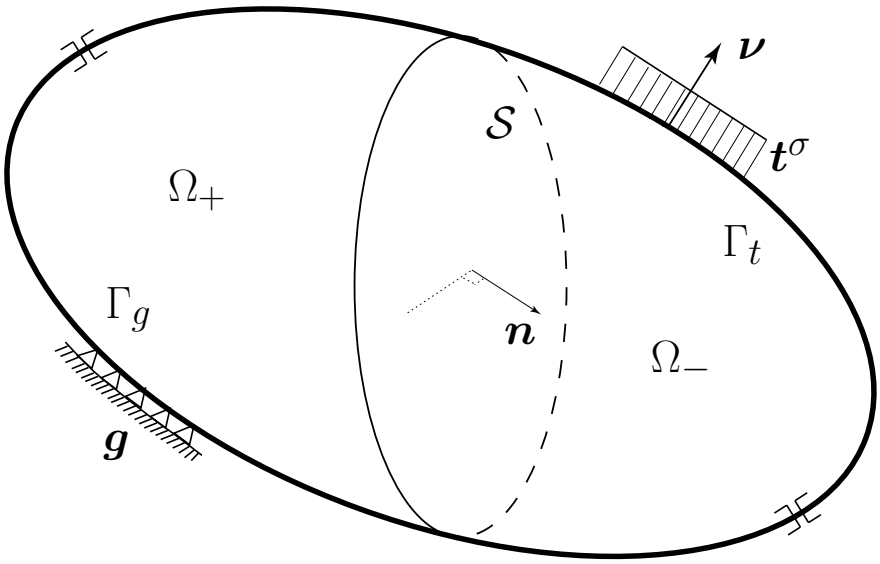

Figure 3.2. Body $\bar{\Omega}$ with planar strong discontinuity $\mathcal{S}$ ($\Omega = \Omega_+ \cup \Omega_-$, $\Gamma = \Gamma_t \cup \Gamma_g \cup \mathcal{S}$, $\bar{\Omega} = \Omega \cup \Gamma$).

The local form of quasi-static, isothermal equilibrium for a body Ω with strong discontinuity is written as follows

$$\begin{aligned} \boldsymbol{\nabla} \cdot \boldsymbol{\sigma} + \boldsymbol{b} \;&=\; \boldsymbol{0} \quad \text{in } \Omega \\ \boldsymbol{\sigma} \cdot \boldsymbol{\nu} \;&=\; \boldsymbol{t}^{\sigma} \quad \text{on } \Gamma_t \\ \boldsymbol{u} \;&=\; \boldsymbol{g} \quad \text{on } \Gamma_g \\ [\![\boldsymbol{\sigma}]\!] \cdot \boldsymbol{n} \;&=\; \boldsymbol{0} \quad \text{across } \mathcal{S} \end{aligned} \tag{3.5}$$

where $\boldsymbol{n}$ is the unit normal to $\mathcal{S}$ and $[\![\boldsymbol{\sigma}]\!]$ is the jump in stress across $\mathcal{S}$.

The variational form of quasi-static equilibrium is then

$$\begin{aligned} \int_{\Omega} \boldsymbol{\nabla}^s \boldsymbol{\eta} : \boldsymbol{\sigma}\, d\Omega \;&=\; \int_{\Omega} \boldsymbol{\eta} \cdot \boldsymbol{b}\, d\Omega \,+\, \int_{\Gamma_t} \boldsymbol{\eta} \cdot \boldsymbol{t}^{\sigma}\, d\Gamma \\ &\quad + \int_{\mathcal{S}} \boldsymbol{\eta} \cdot ([\![\boldsymbol{\sigma}]\!] \cdot \boldsymbol{n})\, d\Gamma \end{aligned} \tag{3.6}$$

$$[\![\boldsymbol{u}(\boldsymbol{x},t)]\!] \;=\; u_n\boldsymbol{n} \,+\, u_t\boldsymbol{t} \;=\; \zeta\boldsymbol{m}$$

weak discontinuity

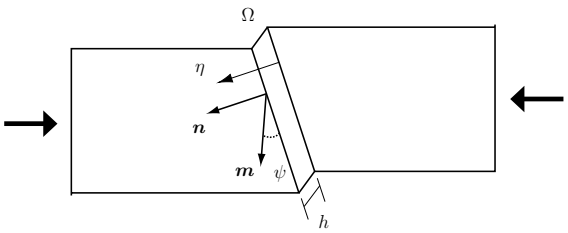

$$\begin{aligned}
\boldsymbol{u}(\boldsymbol{x},t) &= \tilde{\boldsymbol{u}}(\boldsymbol{x},t) \,+\, [\![\boldsymbol{u}(\boldsymbol{x},t)]\!]\,\frac{\eta(\boldsymbol{x})}{h} \\
\boldsymbol{\nabla}\boldsymbol{u}(\boldsymbol{x},t) &= \boldsymbol{\nabla}\tilde{\boldsymbol{u}}(\boldsymbol{x},t) \,+\, \boldsymbol{\nabla}\left([\![\boldsymbol{u}(\boldsymbol{x},t)]\!]\right)\,\frac{\eta(\boldsymbol{x})}{h} \\
&\quad +\, \left([\![\boldsymbol{u}(\boldsymbol{x},t)]\!]\otimes\boldsymbol{n}(\boldsymbol{x})\right)\,\frac{1}{h}
\end{aligned}$$

strong discontinuity

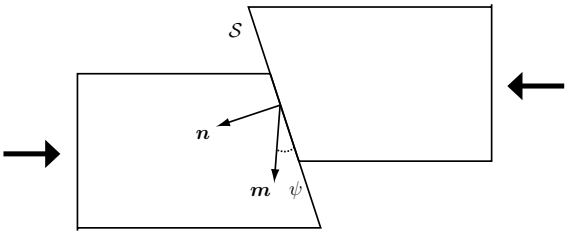

$$\begin{aligned}
\boldsymbol{u}(\boldsymbol{x},t) &= \tilde{\boldsymbol{u}}(\boldsymbol{x},t) \,+\, [\![\boldsymbol{u}(\boldsymbol{x},t)]\!]\,H_{\mathcal{S}}(\boldsymbol{x}) \\
\boldsymbol{\nabla}\boldsymbol{u}(\boldsymbol{x},t) &= \boldsymbol{\nabla}\tilde{\boldsymbol{u}}(\boldsymbol{x},t) \,+\, \boldsymbol{\nabla}\left([\![\boldsymbol{u}(\boldsymbol{x},t)]\!]\right)\,H_{\mathcal{S}}(\boldsymbol{x}) \\
&\quad +\, \left([\![\boldsymbol{u}(\boldsymbol{x},t)]\!]\otimes\boldsymbol{n}(\boldsymbol{x})\right)\,\delta_{\mathcal{S}}(\boldsymbol{x})
\end{aligned}$$

Figure 3.3. Kinematics of weak and strong discontinuities.

As for weak discontinuities, the traction continuity condition $[\![\boldsymbol{\sigma}]\!]\cdot\boldsymbol{n}=\boldsymbol{0}$ for a body with strong discontinuities will be used to determine bifurcation.

3.3 Summary of Sandia GeoModel for bifurcation analysis

Here, a brief summary is given of the three-invariant isotropic/kinematic hardening cap plasticity model (Sandia GeoModel). For more details, refer to Chapt.2.

3.3.1 Rate insensitive model

For small strains, an additive decomposition of the strain rate into elastic and plastic parts is assumed

$$\dot{\boldsymbol{\epsilon}} := \dot{\boldsymbol{\epsilon}}^e + \dot{\boldsymbol{\epsilon}}^p \tag{3.7}$$

Assuming linear isotropic elasticity, the constitutive equation for the stress rate is

$$\dot{\boldsymbol{\sigma}} = \boldsymbol{c}^e : \dot{\boldsymbol{\epsilon}}^e \ , \ \boldsymbol{c}^e = \lambda \mathbf{1} \otimes \mathbf{1} \ + \ 2\mu \boldsymbol{I} \tag{3.8}$$

where λ and μ are the Lamé parameters.

The single yield surface f and plastic potential function g are written in terms of the invariants as

$$f \ = \ \Gamma^2(\beta^\xi) J_2^\xi - [F_y(I_1)]^2 F_c(I_1, \kappa) = 0 \tag{3.9}$$

$$g \ = \ \Gamma^2(\beta^\xi) J_2^\xi \ - \ [F_y^g(I_1)]^2 F_c^g(I_1, \kappa) \tag{3.10}$$

where f is the yield function, $\beta^\xi(J_2^\xi, J_3^\xi)$ is the Lode angle, Γ is a function of β^ξ and Ψ (the ratio of strength in triaxial extension versus triaxial compression, $\Psi = 1$ if no difference in strength), N is the offset of the shear failure surface $F_f(I_1)$ from the initial shear yield surface $F_y(I_1) = F_f(I_1) - N$, $I_1 = \sigma_{ii}$ is the first stress invariant, $J_2^\xi = \frac{1}{2}\boldsymbol{\xi} : \boldsymbol{\xi}$ is the second invariant of the deviatoric relative stress $\boldsymbol{\xi} = \boldsymbol{s} - \boldsymbol{\alpha}$, $\boldsymbol{s}$ is the deviatoric stress, $\boldsymbol{\alpha}$ is the deviatoric backstress associated with the Bauschinger effect, $J_3^\xi = \frac{1}{3}(\boldsymbol{\xi} \cdot \boldsymbol{\xi}) : \boldsymbol{\xi}$ is the third invariant of the deviatoric relative stress, κ is the internal stress variable associated with compaction hardening, $F_y^g(I_1) = F_f^g(I_1) - N$, and g is the plastic potential function allowing for non-associative plastic flow. Material parameters for the shear failure surface $F_f(I_1)$ are determined from peak stress experimental data. The purpose of the shear failure surface is to limit the hardening of the backstress $\boldsymbol{\alpha}$. The effect of $F_c(I_1, \kappa)$ is to provide a smooth elliptical cap. A non-associative flow rule is assumed for plastic flow as

$$\dot{\boldsymbol{\epsilon}}^p \ = \ \dot{\gamma} \frac{\partial g}{\partial \boldsymbol{\sigma}} \ = \ \dot{\gamma} \boldsymbol{g} \tag{3.11}$$

The flow rule is associative if material parameters are chosen such that $f = g$. The evolution of the internal variables is

$$\dot{\boldsymbol{\alpha}} \ = \ \dot{\gamma} \boldsymbol{h}^\alpha(\boldsymbol{\alpha}) \ ; \ \boldsymbol{h}^\alpha(\boldsymbol{\alpha}) = c^\alpha G^\alpha(\boldsymbol{\alpha}) \, \mathrm{dev} \boldsymbol{g}$$

$$\dot{\kappa} \ = \ \dot{\gamma} h^\kappa(\kappa) \ ; \ h^\kappa(\kappa) \ = \ 3 c^\kappa G^\kappa(\kappa) \partial g / \partial I_1$$

To determine the consistency parameter $\dot{\gamma}$, evaluate the consistency condition

$$\dot{f} \;=\; \frac{\partial f}{\partial \boldsymbol{\sigma}} : \dot{\boldsymbol{\sigma}} + \frac{\partial f}{\partial \boldsymbol{\alpha}} : \dot{\boldsymbol{\alpha}} + \frac{\partial f}{\partial \kappa}\dot{\kappa} \;=\; 0 \tag{3.12}$$

then solve for $\dot{\gamma}$

$$\begin{aligned} \dot{\gamma} \;&=\; \frac{1}{\chi}\boldsymbol{f} : \boldsymbol{c}^e : \dot{\boldsymbol{\epsilon}} \\ &\chi = \boldsymbol{f} : \boldsymbol{c}^e : \boldsymbol{g} - \frac{\partial f}{\partial \boldsymbol{\alpha}} : \boldsymbol{h}^\alpha - \frac{\partial f}{\partial \kappa} h^\kappa \end{aligned} \tag{3.13}$$

where $\boldsymbol{f} = \partial f / \partial \boldsymbol{\sigma}$. Substituting into the rate equation for stress gives

$$\dot{\boldsymbol{\sigma}} \;=\; \left(\boldsymbol{c}^e - \frac{1}{\chi}\boldsymbol{c}^e : \boldsymbol{g} \otimes \boldsymbol{f} : \boldsymbol{c}^e \right) : \dot{\boldsymbol{\epsilon}} \;=\; \boldsymbol{c}^{ep} : \dot{\boldsymbol{\epsilon}} \tag{3.14}$$

where $\boldsymbol{c}^{ep}$ is the continuum elasto-plastic tangent.

3.3.2 Rate sensitive model

The rate sensitive form of the model involves a standard viscous regularization following Perzyna [60], which can be expressed in generalized Duvaut-Lions form [18]. The constitutive equations are similar to those of the rate insensitive model except that now there is no consistency condition by which to calculate the plastic consistency parameter (hence, regularizing the rate insensitive plasticity model).

Revisiting equations from the inviscid model, we now introduce a viscoplastic strain rate $\dot{\boldsymbol{\epsilon}}^{vp}$ such that the evolution equations are

$$\begin{aligned} \dot{\boldsymbol{\epsilon}} \;&=\; \dot{\boldsymbol{\epsilon}}^e + \dot{\boldsymbol{\epsilon}}^{vp} \\ \dot{\boldsymbol{\sigma}} \;&=\; \boldsymbol{c}^e : \dot{\boldsymbol{\epsilon}}^e \;=\; \boldsymbol{c}^e : (\dot{\boldsymbol{\epsilon}} - \dot{\boldsymbol{\epsilon}}^{vp}) \\ \dot{\boldsymbol{\epsilon}}^{vp} \;&=\; \dot{\gamma}\boldsymbol{g} \\ \dot{\boldsymbol{\alpha}} \;&=\; \dot{\gamma}\boldsymbol{h}^\alpha \\ \dot{\kappa} \;&=\; \dot{\gamma} h^\kappa \\ \dot{\gamma} \;&=\; \frac{< g >}{\eta} \end{aligned} \tag{3.15}$$

where η is the viscosity coefficient with units $(\text{Pa})^3\text{s}$. These equations may be expressed in generalized Duvaut-Lions form as

$$\begin{aligned}
\dot{\boldsymbol{\epsilon}}^{vp} &= \frac{1}{\tau}(\boldsymbol{c}^e)^{-1} : (\boldsymbol{\sigma} - \bar{\boldsymbol{\sigma}}) \\
\dot{\boldsymbol{\alpha}} &= \frac{-1}{\tau}(\boldsymbol{\alpha} - \bar{\boldsymbol{\alpha}}) \\
\dot{\kappa} &= \frac{-1}{\tau}(\kappa - \bar{\kappa}) \\
\tau &= \frac{\eta}{(2\mu)^3}
\end{aligned} \tag{3.16}$$

where τ is the relaxation time, and $\bar{\boldsymbol{\sigma}}, \bar{\boldsymbol{\alpha}}, \bar{\kappa}$ are solutions to the inviscid problem. The evolution equations can be written as

$$\begin{aligned}
\dot{\boldsymbol{\sigma}} + \frac{1}{\tau}\boldsymbol{\sigma} &= \boldsymbol{c}^e : \dot{\boldsymbol{\epsilon}} + \frac{1}{\tau}\bar{\boldsymbol{\sigma}} \\
\dot{\boldsymbol{\alpha}} + \frac{1}{\tau}\boldsymbol{\alpha} &= \frac{1}{\tau}\bar{\boldsymbol{\alpha}} \\
\dot{\kappa} + \frac{1}{\tau}\kappa &= \frac{1}{\tau}\bar{\kappa}
\end{aligned}$$

Since these are linear ODEs, the closed form solution may be found:

$$\begin{aligned}
\boldsymbol{\sigma}(t) &= (\boldsymbol{\sigma}(0) - \bar{\boldsymbol{\sigma}})\, e^{-t/\tau} + \bar{\boldsymbol{\sigma}} \\
&\quad + e^{-t/\tau}\boldsymbol{c}^e : \int_0^t e^{s/\tau}\dot{\boldsymbol{\epsilon}}(s)ds \qquad (3.17) \\
\boldsymbol{\alpha}(t) &= (\boldsymbol{\alpha}(0) - \bar{\boldsymbol{\alpha}})\, e^{-t/\tau} + \bar{\boldsymbol{\alpha}} \qquad (3.18) \\
\kappa(t) &= (\kappa(0) - \bar{\kappa})\, e^{-t/\tau} + \bar{\kappa} \qquad (3.19)
\end{aligned}$$

To obtain the inviscid solution, $\tau \to 0$, and to obtain the elastic solution, $\tau \to \infty$.

For bifurcation analysis, it is useful to express the rate sensitive form of the model in incremental form, given the inviscid solution determined from say an implicit numerical integration scheme like Backward Euler [22] discussed in Chapt.2. Approximating the integration in Eq.(3.17) leads to [60]

$$\begin{aligned}\boldsymbol{\sigma}_{n+1} &= e^{-\Delta t/\tau}\boldsymbol{\sigma}_n + (1-e^{-\Delta t/\tau})\bar{\boldsymbol{\sigma}}_{n+1} \\ &\quad + \frac{\tau}{\Delta t}(1-e^{-\Delta t/\tau})\boldsymbol{c}^e : \Delta\boldsymbol{\epsilon} \\ &\quad \Delta t = t_{n+1} - t_n \\ &\quad \Delta\boldsymbol{\epsilon} = \boldsymbol{\epsilon}_{n+1} - \boldsymbol{\epsilon}_n\end{aligned} \tag{3.20}$$

where t_{n+1} is the current time. Linearizing Eq.(3.20) leads to

$$\delta\boldsymbol{\sigma} = (1-e^{-\Delta t/\tau})\left(\delta\bar{\boldsymbol{\sigma}} + \frac{\tau}{\Delta t}\boldsymbol{c}^e : \delta\boldsymbol{\epsilon}\right) \tag{3.21}$$

where $\mathcal{L}\boldsymbol{\sigma} = \boldsymbol{\sigma}^o + \delta\boldsymbol{\sigma}$ is the linearization operator [30].

3.4 Bifurcation analysis

The bifurcation analysis follows closely that conducted in [7]. As is well-reported in the literature (Sandler & Wright [56], Needleman [41], Sluys & de Borst [65]) viscous regularization in the manner of Duvaut-Lions inhibits loss of strong ellipticity for strain-softening plasticity models, assuming the viscosity is finite. For a nearly rate insensitive model (viscosity $\eta \approx 0$), however, loss of strong ellipticity via the underlying inviscid model is possible. The first subsection is devoted to bifurcation analysis of the rate insensitive (inviscid) form of the model, while the second addresses bifurcation of the rate sensitive model.

3.4.1 Rate insensitive model

We consider weak discontinuities first and then strong discontinuities, addressing both continuous and discontinuous bifurcation.

weak discontinuity

For **continuous bifurcation**, plastic loading occurs outside the planar band ($\boldsymbol{f} : \boldsymbol{c}^e : \dot{\boldsymbol{\epsilon}}^0 > 0$) and within the band ($\boldsymbol{f} : \boldsymbol{c}^e : \dot{\boldsymbol{\epsilon}}^1 > 0$) at the instant of bifurcation. The plastic consistency parameter is assumed to decompose as (and its two parts determined from the consistency parameter derived in Eq.(3.13))

$$\begin{aligned} \dot{\gamma} &= \dot{\bar{\gamma}} + \frac{1}{h}\dot{\gamma}_h \\ \dot{\bar{\gamma}} &= \frac{1}{\chi}\boldsymbol{f} : \boldsymbol{c}^e : \dot{\boldsymbol{\epsilon}}^0 \\ \dot{\gamma}_h &= \frac{1}{\chi}\boldsymbol{f} : \boldsymbol{c}^e : \mathrm{sym}(\llbracket \boldsymbol{v} \rrbracket \otimes \boldsymbol{n}) \end{aligned} \tag{3.22}$$

Note that h is finite, and thus $\dot{\gamma}$ is bounded. If $h \to 0$ to make $\dot{\gamma}$ unbounded (and, as a result, the stress-like internal state variables unbounded and the plastic dissipation undefined) then a strong discontinuity bifurcation analysis is warranted.

At a material point, assume $\llbracket \boldsymbol{v} \rrbracket$ is spatially-invariant such that

$$\llbracket \boldsymbol{v}(t) \rrbracket = \dot{\zeta}(t)\boldsymbol{m} \tag{3.23}$$

where $\dot{\zeta}$ is the jump rate magnitude and $\boldsymbol{m}$ its direction. Recall from Eq.(3.2) that for traction to be continuous across the planar band with normal $\boldsymbol{n}$, $(\dot{\boldsymbol{\sigma}}^1 - \dot{\boldsymbol{\sigma}}^0) \cdot \boldsymbol{n} = \boldsymbol{0}$ and

$$\begin{aligned} \boldsymbol{n} \cdot \dot{\boldsymbol{\sigma}}^0 &= \boldsymbol{n} \cdot \dot{\boldsymbol{\sigma}}^1 \\ \boldsymbol{n} \cdot \boldsymbol{c}^{ep} : \dot{\boldsymbol{\epsilon}}^0 &= \boldsymbol{n} \cdot \boldsymbol{c}^{ep} : \left(\dot{\boldsymbol{\epsilon}}^0 + \frac{1}{h}\mathrm{sym}(\llbracket \boldsymbol{v} \rrbracket \otimes \boldsymbol{n}) \right) \\ \boldsymbol{0} &= \frac{\dot{\zeta}}{h}\boldsymbol{n} \cdot \boldsymbol{c}^{ep} : \boldsymbol{a} \ , \ \boldsymbol{a} = \mathrm{sym}(\boldsymbol{m} \otimes \boldsymbol{n}) \\ \boldsymbol{0} &= (\boldsymbol{n} \cdot \boldsymbol{c}^{ep} \cdot \boldsymbol{n}) \cdot \boldsymbol{m} = \boldsymbol{A} \cdot \boldsymbol{m} \\ &\Longrightarrow \det \boldsymbol{A} = 0 \quad \text{for} \quad \boldsymbol{m} \neq \boldsymbol{0} \end{aligned} \tag{3.24}$$

Equation (3.24) states that in order for there to be a nontrivial solution $\boldsymbol{m} \neq \boldsymbol{0}$ to the traction continuity condition, the determinant of the acoustic tensor $\boldsymbol{A}$ must be zero. For a given stress state $\boldsymbol{\sigma}$ and state variables $\boldsymbol{\alpha}$ and κ, we solve $\det \boldsymbol{A} = 0$ for the band normals $\boldsymbol{n}$ and then $\boldsymbol{A} \cdot \boldsymbol{m} = \boldsymbol{0}$ for the localized deformation directions.

For **discontinuous bifurcation**, there is elastic unloading outside the band ($\boldsymbol{f} : \boldsymbol{c}^e : \dot{\boldsymbol{\epsilon}}^0 < 0$) and plastic loading within the band ($\boldsymbol{f} : \boldsymbol{c}^e : \dot{\boldsymbol{\epsilon}}^1 > 0$). The consistency parameter is then

$$\begin{aligned} \dot{\gamma} &= \frac{1}{h}\dot{\gamma}_h \\ \dot{\gamma}_h &= \frac{1}{\chi}\boldsymbol{f} : \boldsymbol{c}^e : \left(h\dot{\boldsymbol{\epsilon}}^0 + \mathrm{sym}(\llbracket \boldsymbol{v} \rrbracket \otimes \boldsymbol{n}) \right) \end{aligned} \tag{3.25}$$

Note that h is finite, and thus $\dot{\gamma}$ is bounded. For traction to be continuous across the band,

$$\begin{aligned} \boldsymbol{n}\cdot\dot{\boldsymbol{\sigma}}^0 &= \boldsymbol{n}\cdot\dot{\boldsymbol{\sigma}}^1 \\ \boldsymbol{n}\cdot\boldsymbol{c}^e:\dot{\boldsymbol{\epsilon}}^0 &= \boldsymbol{n}\cdot\left(\boldsymbol{c}^e-\frac{1}{\chi}\boldsymbol{c}^e:\boldsymbol{g}\otimes\boldsymbol{f}:\boldsymbol{c}^e\right): \\ &\quad \left(\dot{\boldsymbol{\epsilon}}^0+\frac{1}{h}\mathrm{sym}([\![\boldsymbol{v}]\!]\otimes\boldsymbol{n})\right) \\ \boldsymbol{0} &= (\boldsymbol{n}\cdot\boldsymbol{c}^e\cdot\boldsymbol{n})\cdot\boldsymbol{m}-\frac{\dot{\gamma}_h}{\dot{\zeta}}\boldsymbol{n}\cdot\boldsymbol{c}^e:\boldsymbol{g} \end{aligned} \tag{3.26}$$

In order to determine bifurcation from Eq.(3.26), we need to assume a relation for $\dot{\gamma}_h/\dot{\zeta}$. Assuming material within the band in the post-localization regime is governed by a simple Mohr-Coulomb planar failure model, the ratio between the plastic consistency parameter $\dot{\gamma}_h$ and shear displacement $\dot{\zeta}$ is dependent upon the dilation/compaction angle ψ (cf. Fig. 3.4) as

$$\frac{\dot{\gamma}_h}{\dot{\zeta}} \;=\; \cos\psi \;=\; \boldsymbol{m}\cdot\boldsymbol{t} \tag{3.27}$$

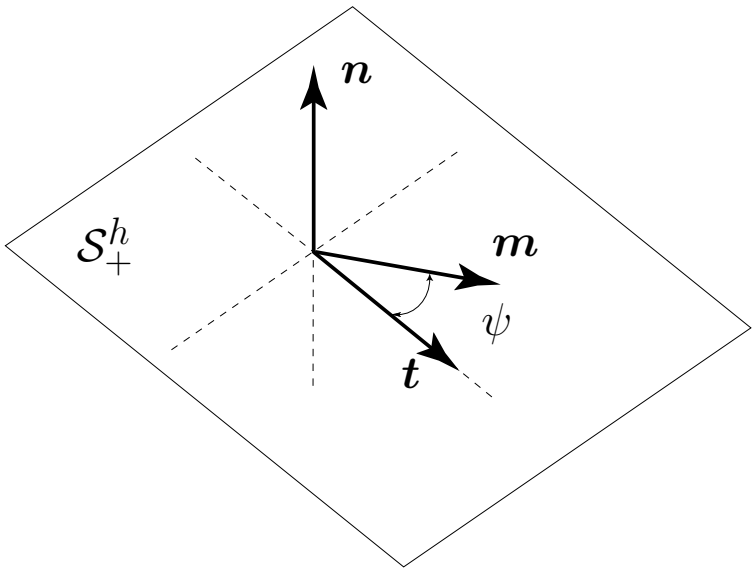

Figure 3.4. Band normal $\boldsymbol{n}$, tangent $\boldsymbol{t}$, and velocity jump direction $\boldsymbol{m}$ with dilation/compaction angle ψ.

Then, for continuous traction across the band to be satisfied for discontinuous bifurcation,

$$
\begin{aligned}
\mathbf{0} &= (\boldsymbol{n}\cdot\boldsymbol{c}^e\cdot\boldsymbol{n})\cdot\boldsymbol{m} - (\boldsymbol{m}\cdot\boldsymbol{t})\boldsymbol{n}\cdot\boldsymbol{c}^e:\boldsymbol{g}\\
\mathbf{0} &= [\boldsymbol{n}\cdot\boldsymbol{c}^e\cdot\boldsymbol{n} - (\boldsymbol{n}\cdot\boldsymbol{c}^e:\boldsymbol{g})\otimes\boldsymbol{t}]\cdot\boldsymbol{m}\\
\mathbf{0} &= \hat{\boldsymbol{A}}\cdot\boldsymbol{m}\\
&\Longrightarrow \det\hat{\boldsymbol{A}}=0 \quad \text{for} \quad \boldsymbol{m}\neq\mathbf{0}
\end{aligned}
\tag{3.28}
$$

Notice the bifurcation conditions for continuous and discontinuous bifurcation in Eqs.(3.24) and (3.28), respectively, are different for the case of weak discontinuity, regardless of the assumption made in Eq.(3.27). It is interesting to note that given the assumption in Eq.(3.27), if we have a pure dilation/compaction band (i.e., $\boldsymbol{m}\cdot\boldsymbol{t}=0$), then discontinuous bifurcation for weak discontinuity is not possible since $\boldsymbol{c}^e$ is positive definite (see Eq. (3.28)).

We will show that for the case of strong discontinuity, the bifurcation conditions are the same for continuous and discontinuous bifurcation.

bifurcation with strong discontinuity

Recall the planar surface is of zero measure, such that the velocity field is discontinuous across $\mathcal{S}$ [62]. For **continuous bifurcation**, the plastic consistency parameter is decomposed as

$$
\dot{\gamma} = \dot{\bar{\gamma}} + \dot{\gamma}_\delta\delta_{\mathcal{S}} \tag{3.29}
$$

In order for the backstress and isotropic stress to be bounded (and the plastic dissipation to be well-defined [62]), the hardening moduli c^α and c^κ bifurcate

$$
\begin{aligned}
(c^\alpha)^{-1} &= (\bar{c}^\alpha)^{-1} + (c^\alpha_\delta)^{-1}\delta_{\mathcal{S}}\\
(c^\alpha)^{-1}\dot{\boldsymbol{\alpha}} &= G^\alpha\dot{\gamma}\mathrm{dev}\boldsymbol{g}\\
\dot{\boldsymbol{\alpha}} &= \bar{c}^\alpha G^\alpha\dot{\bar{\gamma}}\mathrm{dev}\boldsymbol{g} = \bar{\boldsymbol{h}}^\alpha\dot{\bar{\gamma}}\\
\dot{\boldsymbol{\alpha}} &= c^\alpha_\delta G^\alpha\dot{\gamma}_\delta\mathrm{dev}\boldsymbol{g} = \boldsymbol{h}^\alpha_\delta\dot{\gamma}_\delta
\end{aligned}
\tag{3.30}
$$

$$
\begin{aligned}
(c^\kappa)^{-1} &= (\bar{c}^\kappa)^{-1} + (c^\kappa_\delta)^{-1}\delta_{\mathcal{S}}\\
(c^\kappa)^{-1}\dot{\kappa} &= G^\kappa\dot{\gamma}\mathrm{tr}\boldsymbol{g}\\
\dot{\kappa} &= \bar{c}^\kappa G^\kappa\dot{\bar{\gamma}}\mathrm{tr}\boldsymbol{g} = \bar{h}^\kappa\dot{\bar{\gamma}}\\
\dot{\kappa} &= c^\kappa_\delta G^\kappa\dot{\gamma}_\delta\mathrm{tr}\boldsymbol{g} = h^\kappa_\delta\dot{\gamma}_\delta
\end{aligned}
\tag{3.31}
$$

Then, the consistency condition reads

$$\begin{aligned}\dot{f} &= \boldsymbol{f} : \boldsymbol{c}^e : (\dot{\boldsymbol{\epsilon}}^0 + \dot{\zeta}\boldsymbol{a}\,\delta_{\mathcal{S}} - (\dot{\bar{\gamma}} + \dot{\gamma}_\delta\delta_{\mathcal{S}})\boldsymbol{g}) \\ &\quad + \frac{\partial f}{\partial \boldsymbol{\alpha}} : \bar{\boldsymbol{h}}^\alpha \dot{\bar{\gamma}} + \frac{\partial f}{\partial \kappa}\bar{h}^\kappa \dot{\bar{\gamma}} \;=\; 0 \end{aligned} \tag{3.32}$$

and for the regular and singular parts of the consistency condition to be satisfied,

$$\begin{aligned}\dot{\bar{\gamma}} &= \frac{1}{\bar{\chi}}\boldsymbol{f} : \boldsymbol{c}^e : \dot{\boldsymbol{\epsilon}}^0 \\ \bar{\chi} &= \boldsymbol{f} : \boldsymbol{c}^e : \boldsymbol{g} - \frac{\partial f}{\partial \boldsymbol{\alpha}} : \bar{\boldsymbol{h}}^\alpha - \frac{\partial f}{\partial \kappa}\bar{h}^\kappa \\ \dot{\gamma}_\delta &= \frac{\boldsymbol{f} : \boldsymbol{c}^e : \mathrm{sym}([\![\boldsymbol{v}]\!] \otimes \boldsymbol{n})}{\boldsymbol{f} : \boldsymbol{c}^e : \boldsymbol{g}}\end{aligned}$$

Then the stress rate on the surface $\mathcal{S}$, $\dot{\boldsymbol{\sigma}}^1$, and outside the surface, $\dot{\boldsymbol{\sigma}}^0$, read

$$\begin{aligned}\dot{\boldsymbol{\sigma}}^1 &= \underbrace{\left(\boldsymbol{c}^e - \frac{1}{\bar{\chi}}\boldsymbol{c}^e : \boldsymbol{g} \otimes \boldsymbol{f} : \boldsymbol{c}^e\right)}_{\bar{\boldsymbol{c}}^{ep}} : \dot{\boldsymbol{\epsilon}}^0 \\ &\quad + \dot{\zeta}\underbrace{\left(\boldsymbol{c}^e - \frac{\boldsymbol{c}^e : \boldsymbol{g} \otimes \boldsymbol{f} : \boldsymbol{c}^e}{\boldsymbol{f} : \boldsymbol{c}^e : \boldsymbol{g}}\right)}_{\tilde{\boldsymbol{c}}^{ep}} : \boldsymbol{a}\,\delta_{\mathcal{S}} \end{aligned} \tag{3.33}$$

$$\dot{\boldsymbol{\sigma}}^0 = \bar{\boldsymbol{c}}^{ep} : \dot{\boldsymbol{\epsilon}}^0 \tag{3.34}$$

For continuous traction across the discontinuity surface

$$\begin{aligned}\boldsymbol{n}\cdot\dot{\boldsymbol{\sigma}}^0 &= \boldsymbol{n}\cdot\dot{\boldsymbol{\sigma}}^1 \\ \boldsymbol{n}\cdot\bar{\boldsymbol{c}}^{ep} : \dot{\boldsymbol{\epsilon}}^0 &= \boldsymbol{n}\cdot\bar{\boldsymbol{c}}^{ep} : \dot{\boldsymbol{\epsilon}}^0 + \dot{\zeta}\boldsymbol{n}\cdot\tilde{\boldsymbol{c}}^{ep} : \boldsymbol{a}\,\delta_{\mathcal{S}} \\ \boldsymbol{0} &= (\boldsymbol{n}\cdot\tilde{\boldsymbol{c}}^{ep}\cdot\boldsymbol{n})\cdot\boldsymbol{m}\,\delta_{\mathcal{S}} \;=\; \tilde{\boldsymbol{A}}\cdot\boldsymbol{m}\,\delta_{\mathcal{S}} \\ &\Longrightarrow \det\tilde{\boldsymbol{A}} = 0 \quad \text{for} \quad \boldsymbol{m} \neq \boldsymbol{0}\end{aligned} \tag{3.35}$$

For **discontinuous bifurcation**, the consistency parameter is localized to the discontinuity as

$$\dot{\gamma} \;=\; \dot{\gamma}_\delta\delta_{\mathcal{S}} \tag{3.36}$$

Again, the hardening moduli bifurcate in order to have well defined plastic dissipation. Then, the consistency condition reads

$$\begin{aligned} \dot{f} &= \boldsymbol{f} : \boldsymbol{c}^e : (\dot{\boldsymbol{\epsilon}}^0 + \dot{\zeta}\boldsymbol{a}\,\delta_{\mathcal{S}} - \dot{\gamma}_\delta \boldsymbol{g}\delta_{\mathcal{S}}) \\ &\quad + \frac{\partial f}{\partial \boldsymbol{\alpha}} : \boldsymbol{h}^\alpha_\delta \dot{\gamma}_\delta + \frac{\partial f}{\partial \kappa} h^\kappa_\delta \dot{\gamma}_\delta = 0 \end{aligned} \tag{3.37}$$

and for the regular and singular parts of the consistency condition to be satisfied,

$$\dot{\gamma}_\delta = \frac{-\boldsymbol{f} : \boldsymbol{c}^e : \dot{\boldsymbol{\epsilon}}^0}{\frac{\partial f}{\partial \boldsymbol{\alpha}} : \boldsymbol{h}^\alpha_\delta + \frac{\partial f}{\partial \kappa} h^\kappa_\delta} = \frac{\dot{\zeta}\boldsymbol{f} : \boldsymbol{c}^e : \boldsymbol{a}}{\boldsymbol{f} : \boldsymbol{c}^e : \boldsymbol{g}} \tag{3.38}$$

For continuous traction across the discontinuity surface $\mathcal{S}$

$$\begin{aligned} \boldsymbol{n}\cdot\dot{\boldsymbol{\sigma}}^0 &= \boldsymbol{n}\cdot\dot{\boldsymbol{\sigma}}^1 \\ \boldsymbol{n}\cdot\boldsymbol{c}^e : \dot{\boldsymbol{\epsilon}}^0 &= \boldsymbol{n}\cdot\boldsymbol{c}^e : \dot{\boldsymbol{\epsilon}}^0 + \dot{\zeta}\boldsymbol{n}\cdot\tilde{\boldsymbol{c}}^{ep} : \boldsymbol{a}\,\delta_{\mathcal{S}} \\ \boldsymbol{0} &= \tilde{\boldsymbol{A}}\cdot\boldsymbol{m}\,\delta_{\mathcal{S}} \\ &\Longrightarrow \det\tilde{\boldsymbol{A}} = 0 \quad \text{for} \quad \boldsymbol{m} \neq \boldsymbol{0} \end{aligned}$$

Thus, the same bifurcation condition results for continuous and discontinuous bifurcation for the case of strong discontinuity localized kinematics.

3.4.2 Rate sensitive model

weak discontinuity

For **continuous bifurcation**, from Eq.(3.17), the stress just outside and just inside the band are, respectively,

$$\begin{aligned} \boldsymbol{\sigma}^0(t) &= (\boldsymbol{\sigma}^0(0) - \bar{\boldsymbol{\sigma}}^0)\, e^{-t/\tau} + \bar{\boldsymbol{\sigma}}^0 \\ &\quad + e^{-t/\tau}\boldsymbol{c}^e : \int_0^t e^{s/\tau}\dot{\boldsymbol{\epsilon}}^0(s)ds \end{aligned} \tag{3.39}$$

$$\begin{aligned} \boldsymbol{\sigma}^1(t) &= (\boldsymbol{\sigma}^1(0) - \bar{\boldsymbol{\sigma}}^1)\, e^{-t/\tau} + \bar{\boldsymbol{\sigma}}^1 \\ &\quad + e^{-t/\tau}\boldsymbol{c}^e : \int_0^t e^{s/\tau}\dot{\boldsymbol{\epsilon}}^1(s)ds \end{aligned} \tag{3.40}$$

where, recall, $\bar{\boldsymbol{\sigma}}$ denotes inviscid stress, and we assume at time zero that the stresses just inside and just outside the band are equal $\boldsymbol{\sigma}^0(0) = \boldsymbol{\sigma}^1(0)$. Then, for continuous traction across the band,

$$\begin{aligned}
\boldsymbol{n}\cdot\boldsymbol{\sigma}^0(t) &= \boldsymbol{n}\cdot\boldsymbol{\sigma}^1(t) \\
\mathbf{0} &= \boldsymbol{n}\cdot(\bar{\boldsymbol{\sigma}}^1 - \bar{\boldsymbol{\sigma}}^0)(1-e^{-t/\tau}) \\
&\quad + \frac{1}{h}e^{-t/\tau}\boldsymbol{n}\cdot\boldsymbol{c}^e : \boldsymbol{a}\int_0^t e^{s/\tau}\dot{\zeta}(s)ds \\
\tau\to 0 &\implies \boldsymbol{n}\cdot(\bar{\boldsymbol{\sigma}}^1 - \bar{\boldsymbol{\sigma}}^0) = \mathbf{0} \\
\tau\to\infty &\implies (\boldsymbol{n}\cdot\boldsymbol{c}^e\cdot\boldsymbol{n})\cdot\boldsymbol{m} = \mathbf{0}
\end{aligned} \tag{3.41}$$

As expected, for $\tau \to 0$ we obtain the bifurcation condition for the inviscid case, and for $\tau \to \infty$, we obtain the elastic solution and hence no loss of strong ellipticity (real, elastic wave speeds, after Hadamard, cf. Hill [25]). The lower bound ($\tau \to 0$) on the viscous bifurcation condition is useful in that if a geomaterial is nearly rate insensitive even when loaded to high strain rates, its bifurcation will depend on an analysis of the inviscid model. Then, the dynamic characteristics of the crack/shear band propagation and post-localization constitutive response will be important even for a nearly rate insensitive geomaterial.

For a rate sensitive geomaterial, not so highly viscous to be elastic ($\tau > 0$ is finite), there should be no bifurcation to localized deformation mode; see Eq.(3.41). This should be made clear by an analysis for the discrete form of the integrated equations, as in section 4.2.3.

For **discontinous bifurcation**, the analysis is the same as for continuous bifurcation, except that the inviscid stress jump across the band interface such as $\mathcal{S}^h_+$, $\bar{\boldsymbol{\sigma}}^1 - \bar{\boldsymbol{\sigma}}^0$, is different.

$$\begin{aligned}
\bar{\boldsymbol{\sigma}}^0 &= \boldsymbol{c}^e : \boldsymbol{\epsilon}^0 \\
\bar{\boldsymbol{\sigma}}^1 &= \int_0^t \boldsymbol{c}^{ep}(s) : \dot{\boldsymbol{\epsilon}}^1(s)ds \\
\bar{\boldsymbol{\sigma}}^1 - \bar{\boldsymbol{\sigma}}^0 &= \frac{\zeta(t)}{h}\boldsymbol{c}^e : \boldsymbol{a} \\
&\quad - \int_0^t \frac{\boldsymbol{f}(s) : \boldsymbol{c}^e : \dot{\boldsymbol{\epsilon}}^0(s)}{\chi(s)}\boldsymbol{c}^e : \boldsymbol{g}(s)ds \\
&\quad - \frac{1}{h}\int_0^t \frac{\dot{\zeta}(s)\boldsymbol{f}(s) : \boldsymbol{c}^e : \boldsymbol{a}}{\chi(s)}\boldsymbol{c}^e : \boldsymbol{g}(s)ds
\end{aligned}$$

so the inviscid case yields the bifurcation condition formulated for the rate insensitive model.

strong discontinuity

For strong discontinuities, bifurcation analysis of the viscoplastic model is the same as for weak discontinuities, except of course that the inviscid bifurcation analysis is different as shown above in the analysis of the rate insensitive model.

discrete form of rate sensitive model

Bifurcation analysis of the discrete form of a rate sensitive model allows one to analyze acoustic tensors to determine mathematical instability.

In linearized form, the incremental strain for **weak discontinuity** comes from Eq.(3.1). For continuous bifurcation, from Eq.(3.14), the incremental stress for the inviscid solution is given, and from Eq.(3.21), the incremental stress for the viscous solution is

$$\begin{aligned} \delta\boldsymbol{\sigma}^0 &= \underbrace{(1-e^{-\Delta t/\tau})\left(\boldsymbol{c}^{ep} + \frac{\tau}{\Delta t}\boldsymbol{c}^{e}\right)}_{\hat{\boldsymbol{c}}^{ep}} : \delta\boldsymbol{\epsilon}^0 \\ \delta\boldsymbol{\sigma}^1 &= \hat{\boldsymbol{c}}^{ep} : \delta\boldsymbol{\epsilon}^1 \end{aligned} \tag{3.42}$$

Then for continuous traction,

$$\begin{aligned} \boldsymbol{n}\cdot\delta\boldsymbol{\sigma}^0 &= \boldsymbol{n}\cdot\delta\boldsymbol{\sigma}^1 \\ \boldsymbol{n}\cdot\hat{\boldsymbol{c}}^{ep} : \delta\boldsymbol{\epsilon}^0 &= \boldsymbol{n}\cdot\hat{\boldsymbol{c}}^{ep} : \delta\boldsymbol{\epsilon}^0 + \frac{\delta\zeta}{h}\boldsymbol{n}\cdot\hat{\boldsymbol{c}}^{ep} : \boldsymbol{a} \\ \boldsymbol{0} &= (\boldsymbol{n}\cdot\hat{\boldsymbol{c}}^{ep}\cdot\boldsymbol{n})\boldsymbol{m} = \hat{\boldsymbol{A}}\cdot\boldsymbol{m} \\ \tau\to 0 &\implies \hat{\boldsymbol{c}}^{ep} = \boldsymbol{c}^{ep} \\ \tau\to\infty &\implies \hat{\boldsymbol{c}}^{ep} = \boldsymbol{c}^{e} \end{aligned}$$

and for finite $\tau > 0$, $\hat{\boldsymbol{c}}^{ep}$ should remain positive definite, i.e. $\det\hat{\boldsymbol{A}} > 0$, but more analysis is needed to determine this. For discontinuous bifurcation, the incremental form for the inviscid solution along with the incremental viscous solution gives for continuous traction,

$$
\begin{aligned}
\boldsymbol{n}\cdot\delta\boldsymbol{\sigma}^0 &= \boldsymbol{n}\cdot\delta\boldsymbol{\sigma}^1 \\
\mathbf{0} &= -(1-e^{-\Delta t/\tau}) \\
&\quad \times\left(\frac{\boldsymbol{f}:\boldsymbol{c}^e:\delta\boldsymbol{\epsilon}^0}{\chi}\right)\boldsymbol{n}\cdot\boldsymbol{c}^e:\boldsymbol{g} \\
&\quad +\frac{\delta\zeta}{h}\boldsymbol{n}\cdot\hat{\boldsymbol{c}}^{ep}:\boldsymbol{a} \\
\tau\to 0 &\implies \text{inviscid} \\
\tau\to\infty &\implies \text{elastic}
\end{aligned}
$$

and for finite $\tau > 0$, the analysis is inconclusive.

For **strong discontinuity**, the incremental strain from Eq.(3.4) is given. For continuous bifurcation, the incremental form of the inviscid solution comes from Eqs.(3.33) and (3.34) and then for continuous traction,

$$
\begin{aligned}
\boldsymbol{n}\cdot\delta\boldsymbol{\sigma}^0 &= \boldsymbol{n}\cdot\delta\boldsymbol{\sigma}^1 \\
\mathbf{0} &= (\boldsymbol{n}\cdot\hat{\boldsymbol{c}}^{ep}\cdot\boldsymbol{n})\cdot\boldsymbol{m}\,\delta_{\mathcal{S}} = \hat{\boldsymbol{A}}\cdot\boldsymbol{m}\,\delta_{\mathcal{S}} \\
\tau\to 0 &\implies \hat{\boldsymbol{c}}^{ep} = \tilde{\boldsymbol{c}}^{ep} \\
\tau\to\infty &\implies \hat{\boldsymbol{c}}^{ep} = \boldsymbol{c}^e
\end{aligned}
$$

where here $\hat{\boldsymbol{c}}^{ep}$ is a function of $\tilde{\boldsymbol{c}}^{ep}$ rather than $\boldsymbol{c}^{ep}$ in Eq.(3.42). For finite $\tau > 0$, $\hat{\boldsymbol{c}}^{ep}$ should remain positive definite, i.e. that $\det\hat{\boldsymbol{A}} > 0$, but more analysis is needed. For discontinuous bifurcation, the same bifurcation condition for $\tau \to 0$ results as for continuous bifurcaton with strong discontinuity.

3.5 Numerical algorithm to detect loss of ellipticity for 3D stress states

The algorithm as described in [43] has been modified to account for non-symmetric tangents, and the implementation may be found at
“ http://cvs.sourceforge.net/viewcvs.py/tahoe/tahoe/src/elements/continuum/solid/materials/primitives/ ”
in the class DetCheckT, within the function DetCheck3D_SS.

Table 3.1. Parameters for Gosford Sandstone using Drucker-Prager model [47] for verifying and testing 3D numerical algorithm in section 3.5

Symbol	Value
E	15 GPa
ν	0.3
cohesion $\bar{\alpha}$	13 MPa
friction β	0.5
dilation b	0.35
hard./soft. mod. H	-1 GPa

3.6 Numerical examples

The first numerical example is used to verify the numerical optimization algorithm for the plane strain case, for which we have an analytical solution for the bifurcation condition and slip line normal [43]. The second example demonstrates the ability of the algorithm to determine bifurcation and slip surface normals for a three-dimensional boundary value problem, corner shear. The third example demonstrates the algorithm for plane strain compression using the GeoModel and tests the effect of viscosity on loss of ellipticity.

3.6.1 Plane strain verification

The numerical optimization algorithm is verified for a plane strain example (material parameters shown in Table 3.1), using eight trilinear hexahedral elements constrained in the out-of-plane direction and loaded in confined compression similar to the example discussed in [48]. The comparison of the two numerical solutions is reasonable and is shown in Table 3.2.

3.6.2 Corner shear

Using the parameters from Table 3.1, the second example tests the nonlinear optimization algorithm for a three-dimensional corner shear problem shown in Fig. 3.5. A displacement is prescribed at the corner node $(1, 1, 1)$ with direction $\boldsymbol{d}/\|\boldsymbol{d}\| = [1, -1, 1]$. The plot of force versus magnitude of the displacement vector $\|\boldsymbol{d}\|$ is shown in Fig. 3.6 for the standard plasticity solution only; no post-bifurcation numerical solution is shown. The Gauss point closest to this corner node plastifies and localizes first. The resulting normals and slip directions are shown in Table 3.3, one of which makes physical sense, $\boldsymbol{n} = [0.57, 0.59, 0.57]$.

Table 3.2. Comparison of slip line and slip surface normals for 2D plane strain and 3D constrained plane strain, respectively

	2D plane strain		3D constrained plane strain	
$\boldsymbol{n}$	$\begin{bmatrix} 0.84 \\ 0.54 \\ 0 \end{bmatrix}$	$\begin{bmatrix} 0.84 \\ -0.54 \\ 0 \end{bmatrix}$	$\begin{bmatrix} 0.82 \\ 0.57 \\ 0.0 \end{bmatrix}$	$\begin{bmatrix} 0.84 \\ -0.57 \\ 0.0 \end{bmatrix}$
$\boldsymbol{m}$	$\begin{bmatrix} 0.84 \\ -0.54 \\ 0 \end{bmatrix}$	$\begin{bmatrix} -0.84 \\ -0.54 \\ 0 \end{bmatrix}$	$\begin{bmatrix} 0.82 \\ -0.57 \\ 0.0 \end{bmatrix}$	$\begin{bmatrix} -0.82 \\ -0.57 \\ 0.0 \end{bmatrix}$
ψ	24.7°		21.1°	

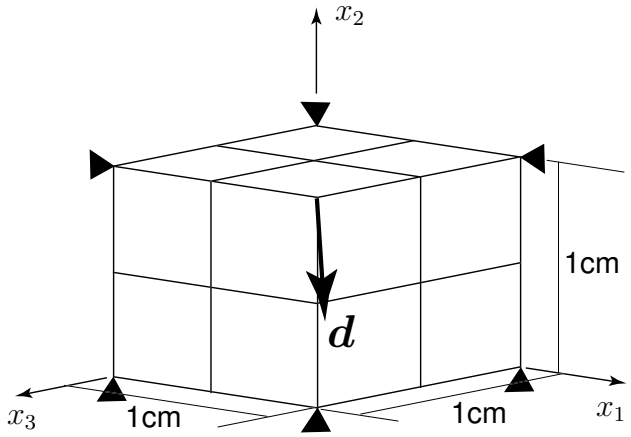

Figure 3.5. Eight hexahedral element mesh with pinned corners and prescribed displacement $\boldsymbol{d}$ at one corner.

Table 3.3. Slip surface normals for 3D corner shear.

	3D corner shear	
$\boldsymbol{n}$	$\begin{bmatrix} 0.57 \\ 0.59 \\ 0.57 \end{bmatrix}$	$\begin{bmatrix} 0.57 \\ -0.6 \\ 0.57 \end{bmatrix}$
$\boldsymbol{m}$	$\begin{bmatrix} 0.6 \\ -0.52 \\ 0.6 \end{bmatrix}$	$\begin{bmatrix} 0.6 \\ 0.53 \\ 0.6 \end{bmatrix}$
ψ	22.2° 21.5°	

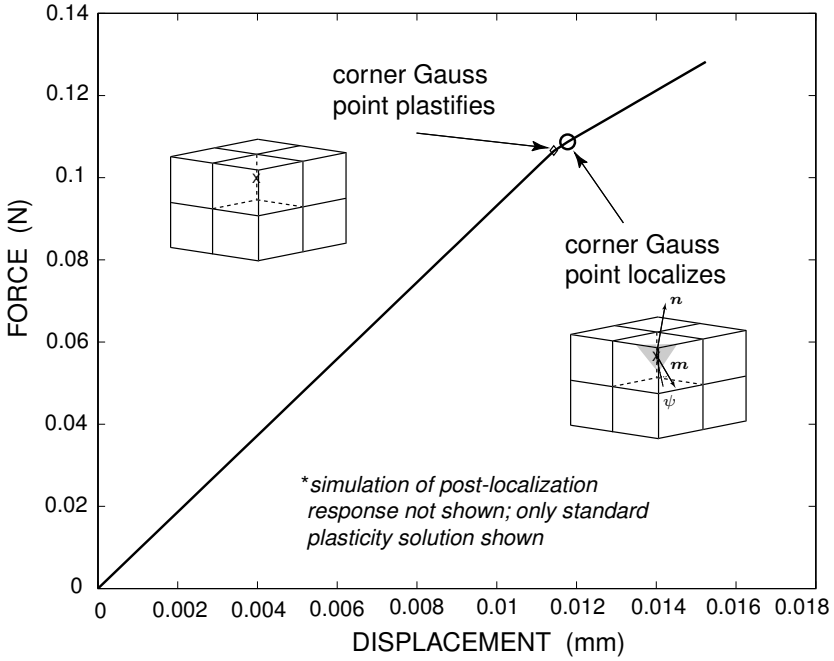

Figure 3.6. Plot of force versus displacement for corner shear simulation.

3.6.3 Choosing discontinuity plane normal $\boldsymbol{n}$

For a general three-dimensional stress state, three unique normals $\boldsymbol{n}$ may be generated. An algorithm must then be developed to test which normal to choose. Based on experience, we found that the following test works best, for the various jump displacement directions $\boldsymbol{m}$ and discontinuity surface normals $\boldsymbol{n}$

$$\text{maximize} \quad \boldsymbol{\nabla u} : \boldsymbol{m} \otimes \boldsymbol{n} \tag{3.43}$$

Attempts at finding the normal that maximized the dissipation, or the normal that minimized $\det \boldsymbol{A}$, did not consistently work as well as this test.

3.6.4 Bifurcation for rate-sensitive Sandia Geomodel

Using parameters given in Box 2 for Salem Limestone, along with a relaxation time $\tau = 5 \times 10^{-4}$ sec, loss of ellipticity is checked for 0.025/sec, 0.25/sec, and 2.5/sec strain rates. As shown in Fig.3.7, loss of ellipticity is detected for the 0.025/sec and 0.25/sec strain rates,

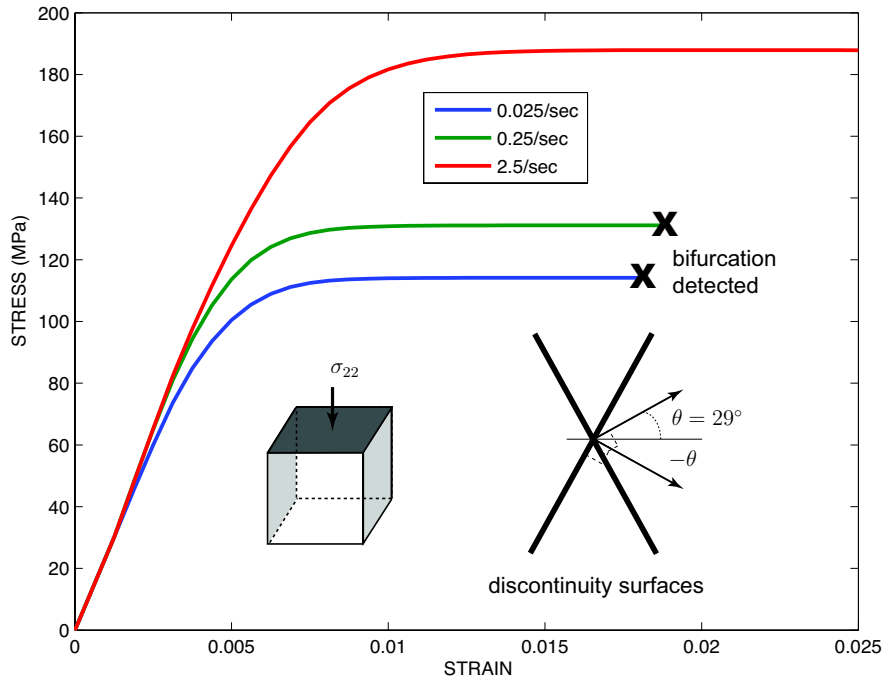

Figure 3.7. Plot of stress versus strain for bifurcation analysis of plane strain compression of Salem Limestone using the Sandia Geomodel. One element 0.04m wide by 0.08m high is used for the simulations.

while it is inhibited for the 2.5/sec strain rate, a result that is well documented in the literature (cf. [41]).

3.7 Conclusions

For a rate insensitive model, bifurcation conditions under weak discontinuity for continuous and discontinuous bifurcation are different whereas they are the same under strong discontinuity. This result for strong discontinuity stems from bifurcation of the hardening moduli that leads to an elastic-perfectly-plastic acoustic tensor [62]. For determining mathematical instability for weak discontinuities, however, it was shown in [50] that continuous bifurcation provides the lower bound for the range of discontinuous bifurcation, and thus is the more critical condition. For a rate sensitive model, it is not surprising that for large viscosity, mathematical stability is ensured even for strain-softening plasticity. For smaller values of viscosity, bifurcation could occur, depending on the strain rate.

The 3D numerical bifurcation algorithm correctly predicted two unique slip normals for the contrained out-of-plane case (plane strain), and a corner shear problem also predicted two

unique normals, most likely as a result of the loading symmetry. For now, this bifurcation algorithm will be used to trigger a post-bifurcation constitutive model. In the future, we need to develop a universal bifurcation condition/strategy that works for both high and low strain rates. In our modeling, we introduce viscous regularization to represent the viscosity of the material, not to inhibit onset of localization. Therefore, we need a bifurcation criterion that will predict onset of localization at high strain rates because that is what is observed experimentally (cf., for example, [23]).

This page intentionally left blank.

Chapter 4

Post-bifurcation traction-displacement constitutive models

Authors: R.A. Regueiro, M.T. Manzari

In this chapter, a general form of post-bifurcation traction-displacement models is presented, along with some specific ones for geomaterials.

The general form of a post-bifurcation traction-displacement constitutive model is the following:

$$\text{traction}: \quad \boldsymbol{T} = [T_n \; T_t]\,; \quad T_n = \boldsymbol{n}\cdot\boldsymbol{\sigma}\cdot\boldsymbol{n}\,; \quad T_t = \boldsymbol{t}\cdot\boldsymbol{\sigma}\cdot\boldsymbol{n} \tag{4.1}$$

$$\text{displacement}: \quad [\![\dot{\boldsymbol{u}}]\!] = \dot{\gamma}_\delta \partial G(\boldsymbol{T},\boldsymbol{q})/\partial \boldsymbol{T} \tag{4.2}$$

$$\text{yield function}: \quad F(\boldsymbol{T},\boldsymbol{q}) = 0 \tag{4.3}$$

$$\text{evolution equations}: \quad \dot{\boldsymbol{q}} = \dot{\gamma}_\delta \boldsymbol{h}^q \tag{4.4}$$

where $\boldsymbol{T}$ is the traction vector on $\mathcal{S}$, $\boldsymbol{t}$ is the unit tangent vector, $[\![\dot{\boldsymbol{u}}]\!] = \dot{u}_t\boldsymbol{t} + \dot{u}_n\boldsymbol{n} = \dot{\zeta}\boldsymbol{m}$ is the rate of jump displacement, $\dot{\zeta} = \| [\![\dot{\boldsymbol{u}}]\!] \|$ its magnitude, $\boldsymbol{m} = [\![\dot{\boldsymbol{u}}]\!] / (\| [\![\dot{\boldsymbol{u}}]\!] \|)$ its direction, $\dot{\boldsymbol{u}} = d\boldsymbol{u}/dt$, $\dot{\gamma}_\delta$ is an internal inelastic multiplier on $\mathcal{S}$, G is an inelastic potential function, F is an inelastic yield function, $\boldsymbol{q}$ is a vector of internal strength variables (e.g., χ tensile strength, c cohesion, ϕ friction angle, ψ dilation angle), and $\boldsymbol{h}^q$ is a vector of softening functions.

4.1 Simple Mohr-Coulomb like traction-displacement model

A simple, Mohr-Coulomb like traction-displacement model is summarized as

$$
\begin{aligned}
F &= |T_t| - (c - T_n^* \tan\phi) \;=\; 0 \\
G &= |T_t| - (c - T_n^* \tan\psi) \\
c &= c_r + (c_p - c_r)\exp\left(-\alpha_c \gamma_\delta\right) \quad ; \quad \gamma_\delta = \int_0^t \dot{\gamma}_\delta dt \quad ; \quad \dot{\gamma}_\delta = \cos\psi\dot{\zeta} \\
\phi &= \phi_r + (\phi_p - \phi_r)\exp\left(-\alpha_\phi \gamma_\delta\right) \\
\psi &= \psi_p \exp\left(-\alpha_\psi \gamma_\delta\right)
\end{aligned}
$$

where $T_n^* = (T_n - |T_n|)/2$, and the vector of internal variables is

$$
\boldsymbol{q} = \left[\begin{array}{ccc} c & \phi & \psi \end{array} \right]^T \tag{4.5}
$$

with c cohesion, ϕ friction angle, and ψ dilation angle. Subscript $(\bullet)_r$ refers to residual value, and $(\bullet)_p$ peak value. The material parameters α_c, α_ϕ, and α_ψ control the rate of softening for each internal variable.

The implementation of this model using an Embedded Discontinuity Finite Element formulation is discussed in Chapt. 6.

4.2 Geomaterial traction-displacement model

A more sophisticated traction-displacement model that models post-bifurcation softening, including tensile softening, is written as

$$
\begin{aligned}
F &= T_t^2 - (c - T_n \tan\phi)^2 + (c - \chi \tan\phi)^2 \;=\; 0 \\
G &= T_t^2 - (c - T_n \tan\psi)^2 \\
c &= c_r + (c_p - c_r)\exp\left(-\alpha_c \epsilon_s^p\right) \quad ; \quad \epsilon_s^p = \int_0^t \dot{\epsilon}_s^p dt \quad ; \quad \dot{\epsilon}_s^p = \frac{\text{sign}(T_t)}{G_f^{II}}(|T_t| - |T_n^* \tan\phi|)\dot{u}_t \\
\chi &= \chi_r + (\chi_p - \chi_r)\exp\left(-\alpha_\chi \epsilon_n^p\right) \quad ; \quad \epsilon_n^p = \int_0^t \dot{\epsilon}_n^p dt \quad ; \quad \dot{\epsilon}_n^p = \frac{1}{G_f^I}(\langle T_n \rangle \dot{u}_n + T_t \dot{u}_t) \\
\tan\phi &= \tan\phi_r + (\tan\phi_p - \tan\phi_r)\exp\left(-\alpha_\phi \epsilon_s^p\right) \\
\tan\psi &= (\tan\psi_p)\exp\left(-\alpha_\psi \epsilon_s^p\right)
\end{aligned}
$$

where $\langle T_n \rangle = (T_n + |T_n|)/2$, $T_n^* = (T_n - |T_n|)/2$, and the vector of internal variables is

$$
\boldsymbol{q} = \left[\begin{array}{cccc} c & \chi & \phi & \psi \end{array} \right]^T \tag{4.6}
$$

with c cohesion, χ tensile internal variable, ϕ friction angle, and ψ dilation angle. Subscript $(\bullet)_r$ refers to residual value, and $(\bullet)_p$ peak value. G_f^{II} is the fracture energy for mode II (shear) fracture, and G_f^I is the fracture energy for mode I (tension) fracture. The material parameters α_c, α_χ, α_ϕ, and α_ψ control the rate of softening for each internal variable.

The implementation of this model using a Cohesive Surface Element formulation is discussed in Chapt. 5.

This page intentionally left blank.

Chapter 5

Cohesive surface element implementation

Authors: M.T. Manzari, R.A. Regueiro

In this chapter, the implementation of an elasto-plastic and rigid-plastic traction-displacement (or cohesive zone) model as presented in Section 4.2 is carried out using a Cohesive Surface Element (CSE) [31].

We consider two formulations of a cohesive zone model for geomaterials, where the only difference is that one includes elastic cohesive displacements (elasto-plastic cohesive zone model), whereas the other does not (rigid-plastic cohesive zone model). The appeal of the rigid-plastic model over the elasto-plastic one is that no fictitious elastic compliance is introduced at the cohesive surface interface. This is particularly important if one is to generate a finite element mesh with CSEs at each element interface, thus generating a mesh-dependent result for an elastic solution, let alone a plastic one. We will use CSEs in the future as adaptively embedded elements, so this problem will be avoided. On physical grounds, however, we believe for geomaterials there is negligible, if any, elasticity within the cohesive zone.

Two numerical examples will be used to test the numerical implementation of each model: 1) constrained shear, and 2) pure tension.

5.1 Variational equations

The weak form for elastostatics including the cohesive zone tractions becomes

$$\int_{\mathcal{B}} \boldsymbol{\nabla w} : \boldsymbol{\sigma} dv \;\; = \;\; \int_{\mathcal{B}} \boldsymbol{b} \cdot \boldsymbol{w} dv + \int_{\Gamma_t} \boldsymbol{t}^{\sigma} \cdot \boldsymbol{w} da + \underbrace{\int_{\Gamma_T} \boldsymbol{T} \cdot [\![\boldsymbol{w}]\!] \, d\mathcal{S}}_{\text{cohesive surface}} \tag{5.1}$$

where $\boldsymbol{T}$ is the vector of tractions on the cohesive surface Γ_T, and $[\![\boldsymbol{w}]\!]$ is the jump in displacement variation or weighting function.

Upon linearizing Eq.5.1, we find we need the traction $\boldsymbol{T}$ and its Jacobian $\partial \boldsymbol{T} / \partial [\![\boldsymbol{u}]\!]$, where $[\![\boldsymbol{u}]\!]$ is the jump displacement, or cohesive surface displacement.

5.2 Implicit integration of elasto-plastic cohesive zone model for geomaterials

For an elasto-plastic cohesive zone, the jump displacement is additively decomposed into elastic and plastic parts as

$$[\![\boldsymbol{u}]\!] = [\![\boldsymbol{u}^e]\!] + [\![\boldsymbol{u}^p]\!] \tag{5.2}$$

The traction rate may be written as

$$\dot{\boldsymbol{T}} = \boldsymbol{K}^e \cdot [\![\dot{\boldsymbol{u}}^e]\!] = \boldsymbol{K}^e \cdot ([\![\dot{\boldsymbol{u}}]\!] - [\![\dot{\boldsymbol{u}}^p]\!]) \; ; \quad \boldsymbol{K}^e = \begin{bmatrix} E_n & 0 \\ 0 & E_t \end{bmatrix} \tag{5.3}$$

where E_n is the normal elastic modulus and E_t the tangential elastic modulus along the cohesive surface. The evolution equations for $[\![\dot{\boldsymbol{u}}^p]\!]$ and the internal variables are written in Section 4.2. For the softening functions, we write

$$\boldsymbol{h}^q = \boldsymbol{A} \cdot \boldsymbol{B} \cdot \partial G / \partial \boldsymbol{T} \; ; \quad \boldsymbol{A} = \begin{bmatrix} A_1 & 0 \\ 0 & A_2 \\ 0 & A_3 \\ 0 & A_4 \end{bmatrix} \; ; \quad \boldsymbol{B} = \begin{bmatrix} B_1 & B_2 \\ 0 & B_3 \end{bmatrix} \tag{5.4}$$

$$A_1 = -\alpha_\chi(\chi - \chi_r) \qquad B_1 = \langle T_n \rangle / G_f^I \tag{5.5}$$

$$A_2 = -\alpha_c(c - c_r) \qquad B_2 = T_t / G_f^I \tag{5.6}$$

$$A_3 = -\alpha_\phi(\tan\phi - \tan\phi_r) \quad B_3 = \frac{\text{sign}(T_t)}{G_f^{II}}(|T_t| - |T_n^* \tan\phi|) \tag{5.7}$$

$$A_4 = -\alpha_\psi \tan\psi \tag{5.8}$$

Given the loading and unloading (Kuhn-Tucker) conditions [60]

$$\dot\gamma_\delta \geq 0\,,\ F \leq 0 \implies \dot\gamma_\delta \dot F = 0 \tag{5.9}$$

we can solve for the inelastic multiplier

$$\dot\gamma_\delta = \frac{\partial F_{\boldsymbol{T}} \cdot \boldsymbol{K}^e \cdot [\![\dot{\boldsymbol{u}}]\!]}{H}\,; \quad H = \partial F_{\boldsymbol{T}} \cdot \boldsymbol{K}^e \cdot \partial G_{\boldsymbol{T}} - \partial F_{\boldsymbol{q}} \cdot \boldsymbol{h}^q \tag{5.10}$$

where $\partial F_{\boldsymbol{T}} = \partial F/\partial \boldsymbol{T}$, $\partial G_{\boldsymbol{T}} = \partial G/\partial \boldsymbol{T}$, $\partial F_{\boldsymbol{q}} = \partial F/\partial \boldsymbol{q}$. The continuum elasto-plastic tangent is then

$$\boldsymbol{K}^{ep} = \boldsymbol{K}^e - (\boldsymbol{K}^e \cdot \partial G_{\boldsymbol{T}}) \otimes (\partial G_{\boldsymbol{T}} \cdot \boldsymbol{K}^e)\,/H \tag{5.11}$$

For numerical integration, we use Backward Euler [60]. For simplicity of notation, we leave off the current time step designator $(\bullet)_{n+1}$ and iteration number $(\bullet)^{k+1}$, where

$$\Delta(\bullet) = (\bullet)_{n+1} - (\bullet)_n\,; \quad \Delta t = t_{n+1} - t_n \tag{5.12}$$

$$\delta(\bullet) = (\bullet)^{k+1} - (\bullet)^k \tag{5.13}$$

Integrating

$$\boldsymbol{T} = \boldsymbol{T}_n + \boldsymbol{K}^e \cdot \Delta([\![\boldsymbol{u}]\!] - [\![\boldsymbol{u}^p]\!]) \tag{5.14}$$

$$\Delta [\![\boldsymbol{u}^p]\!] = \Delta\gamma_\delta \partial G_{\boldsymbol{T}} \tag{5.15}$$

$$\Delta \boldsymbol{q} = \Delta\gamma_\delta \boldsymbol{h}^q \tag{5.16}$$

or in residual form

$$\boldsymbol{R} = \begin{bmatrix} -\Delta \left[\!\left[\boldsymbol{u}^p \right]\!\right] \\ -\Delta \boldsymbol{q} \\ F \end{bmatrix} + \Delta\gamma_\delta \begin{bmatrix} \partial G_{\boldsymbol{T}} \\ \boldsymbol{h}^q \\ 0 \end{bmatrix} = \boldsymbol{0} \tag{5.17}$$

These are 3 nonlinear equations for 3 unknowns $\left[\!\left[\boldsymbol{u}^p \right]\!\right]$, $\boldsymbol{q}$, and γ_δ, so we linearize such that

$$\boldsymbol{R} = \boldsymbol{R}^k + \delta\boldsymbol{R} = \boldsymbol{0} \tag{5.18}$$

where

$$\delta\boldsymbol{R} = \begin{bmatrix} (\boldsymbol{K}^e)^{-1} \cdot \delta\boldsymbol{T} + \Delta\gamma_\delta \left(\partial G_{\boldsymbol{TT}} \cdot \delta\boldsymbol{T} + \partial G_{\boldsymbol{Tq}} \cdot \delta\boldsymbol{q}\right) + \delta\gamma_\delta \partial G_{\boldsymbol{T}} \\ -\delta\boldsymbol{q} + \Delta\gamma_\delta \left(\partial \boldsymbol{h}^q_{\boldsymbol{T}} \cdot \delta\boldsymbol{T} + \partial \boldsymbol{h}^q_{\boldsymbol{q}} \cdot \delta\boldsymbol{q}\right) + \delta\gamma_\delta \boldsymbol{h}^q \\ \partial F_{\boldsymbol{T}} \cdot \delta\boldsymbol{T} + \partial F_{\boldsymbol{q}} \cdot \delta\boldsymbol{q} \end{bmatrix} \tag{5.19}$$

Given that the third equation of Eq.(5.18) is independent of $\delta\gamma_\delta$ we can statically condense out this equation to solve for $\delta\gamma_\delta$ as

$$\delta\gamma_\delta = \frac{F - \left[\partial F_{\boldsymbol{T}} \; \partial F_{\boldsymbol{q}}\right] \cdot \boldsymbol{D}^{-1} \cdot \begin{bmatrix} \boldsymbol{R}^u \\ \boldsymbol{R}^q \end{bmatrix}}{\left[\partial F_{\boldsymbol{T}} \; \partial F_{\boldsymbol{q}}\right] \cdot \boldsymbol{D}^{-1} \cdot \begin{bmatrix} \partial G_{\boldsymbol{T}} \\ \boldsymbol{h}^q \end{bmatrix}} \tag{5.20}$$

where

$$\boldsymbol{D} = \begin{bmatrix} (\boldsymbol{K}^e)^{-1} + \Delta\gamma_\delta \partial G_{\boldsymbol{TT}} & \Delta\gamma_\delta \partial G_{\boldsymbol{Tq}} \\ \Delta\gamma_\delta \partial \boldsymbol{h}^q_{\boldsymbol{T}} & -\boldsymbol{1} + \Delta\gamma_\delta \partial \boldsymbol{h}^q_{\boldsymbol{q}} \end{bmatrix} \tag{5.21}$$

Then the increment of traction and internal variables may be calculated as

$$\begin{bmatrix} \delta\boldsymbol{T} \\ \delta\boldsymbol{q} \end{bmatrix} = -\boldsymbol{D}^{-1} \cdot \begin{bmatrix} \boldsymbol{R}^u + \delta\gamma_\delta \partial G_{\boldsymbol{T}} \\ \boldsymbol{R}^q + \delta\gamma_\delta \boldsymbol{h}^q \end{bmatrix} \tag{5.22}$$

and the increment of jump plastic displacement is updated as $\left[\!\left[\delta\boldsymbol{u}^p \right]\!\right] = -(\boldsymbol{K}^e)^{-1} \cdot \delta\boldsymbol{T}$. The variables may then be updated

$$
\begin{aligned}
(\llbracket \boldsymbol{u}^p \rrbracket)^{k+1} &= (\llbracket \boldsymbol{u}^p \rrbracket)^k + \llbracket \delta \boldsymbol{u}^p \rrbracket && (5.23)\\
\boldsymbol{q}^{k+1} &= \boldsymbol{q}^k + \delta \boldsymbol{q} && (5.24)\\
\gamma_\delta^{k+1} &= \gamma_\delta^k + \delta\gamma_\delta && (5.25)
\end{aligned}
$$

Then check for convergence $\|\boldsymbol{R}^{k+1}\|/\|\boldsymbol{R}^0\| \leq \text{tol}$, where tol is a chosen tolerance value, and if satisfied continue to next time step, otherwise iterate $k = k + 1$.

5.3 Implicit integration of rigid-plastic cohesive zone model for geomaterials

For a rigid-plastic cohesive zone, the jump displacement is only plastic such that

$$\llbracket \boldsymbol{u} \rrbracket = \llbracket \boldsymbol{u}^p \rrbracket \tag{5.26}$$

the consistency condition then leads to the inelastic multiplier

$$\dot{\gamma}_\delta = \frac{\partial F_{\boldsymbol{T}} \cdot \dot{\boldsymbol{T}}}{H^p} \; ; \quad H^p = -\partial F_{\boldsymbol{q}} \cdot \boldsymbol{h}^q \tag{5.27}$$

where, when using the flow rule in Eq.(4.2), the rigid-plastic continuum tangent is

$$\dot{\boldsymbol{T}} = \boldsymbol{K}^p \cdot \llbracket \dot{\boldsymbol{u}}^p \rrbracket \; ; \quad \boldsymbol{K}^p = H^p \left(\partial G_{\boldsymbol{T}} \otimes \partial F_{\boldsymbol{T}}\right)^{-1} \tag{5.28}$$

Similar to the elasto-plastic model, we integrate using Backward-Euler, and iterate to solve for the jump displacment $\llbracket \boldsymbol{u}^p \rrbracket$, internal variables $\boldsymbol{q}$, and inelastic multiplier γ_δ.

Integrating

$$
\begin{aligned}
\boldsymbol{T} &= \boldsymbol{T}_n + \boldsymbol{K}^p \cdot \Delta \llbracket \boldsymbol{u}^p \rrbracket && (5.29)\\
\Delta \llbracket \boldsymbol{u}^p \rrbracket &= \Delta\gamma_\delta \partial G_{\boldsymbol{T}} && (5.30)\\
\Delta \boldsymbol{q} &= \Delta\gamma_\delta \boldsymbol{h}^q && (5.31)
\end{aligned}
$$

or in residual form

$$\boldsymbol{R} = \begin{bmatrix} -\Delta \left[\!\left[\boldsymbol{u}^p \right]\!\right] \\ -\Delta \boldsymbol{q} \\ F \end{bmatrix} + \Delta\gamma_\delta \begin{bmatrix} \partial G_{\boldsymbol{T}} \\ \boldsymbol{h}^q \\ 0 \end{bmatrix} = \boldsymbol{0} \tag{5.32}$$

These are 3 nonlinear equations for 3 unknowns $\left[\!\left[\boldsymbol{u}^p \right]\!\right]$, $\boldsymbol{q}$, and γ_δ, so we linearize such that

$$\boldsymbol{R} = \boldsymbol{R}^k + \delta\boldsymbol{R} = \boldsymbol{0} \tag{5.33}$$

where

$$\delta\boldsymbol{R} = \begin{bmatrix} (\boldsymbol{K}^p)^{-1} \cdot \delta\boldsymbol{T} + \Delta\gamma_\delta \left(\partial G_{\boldsymbol{TT}} \cdot \delta\boldsymbol{T} + \partial G_{\boldsymbol{Tq}} \cdot \delta\boldsymbol{q}\right) + \delta\gamma_\delta \partial G_{\boldsymbol{T}} \\ -\delta\boldsymbol{q} + \Delta\gamma_\delta \left(\partial \boldsymbol{h}^q_{\boldsymbol{T}} \cdot \delta\boldsymbol{T} + \partial \boldsymbol{h}^q_{\boldsymbol{q}} \cdot \delta\boldsymbol{q}\right) + \delta\gamma_\delta \boldsymbol{h}^q \\ \partial F_{\boldsymbol{T}} \cdot \delta\boldsymbol{T} + \partial F_{\boldsymbol{q}} \cdot \delta\boldsymbol{q} \end{bmatrix} \tag{5.34}$$

Given that the third equation of Eq.(5.18) is independent of $\delta\gamma_\delta$ we can statically condense out this equation to solve for $\delta\gamma_\delta$ as

$$\delta\gamma_\delta = \frac{F - \left[\partial F_{\boldsymbol{T}} \; \partial F_{\boldsymbol{q}}\right] \cdot \boldsymbol{D}^{-1} \cdot \begin{bmatrix} \boldsymbol{R}^u \\ \boldsymbol{R}^q \end{bmatrix}}{\left[\partial F_{\boldsymbol{T}} \; \partial F_{\boldsymbol{q}}\right] \cdot \boldsymbol{D}^{-1} \cdot \begin{bmatrix} \partial G_{\boldsymbol{T}} \\ \boldsymbol{h}^q \end{bmatrix}} \tag{5.35}$$

where

$$\boldsymbol{D} = \begin{bmatrix} (\boldsymbol{K}^p)^{-1} + \Delta\gamma_\delta \partial G_{\boldsymbol{TT}} & \Delta\gamma_\delta \partial G_{\boldsymbol{Tq}} \\ \Delta\gamma_\delta \partial \boldsymbol{h}^q_{\boldsymbol{T}} & -\boldsymbol{1} + \Delta\gamma_\delta \partial \boldsymbol{h}^q_{\boldsymbol{q}} \end{bmatrix} \tag{5.36}$$

Then the increment of traction and internal variables may be calculated as

$$\begin{bmatrix} \delta\boldsymbol{T} \\ \delta\boldsymbol{q} \end{bmatrix} = -\boldsymbol{D}^{-1} \cdot \begin{bmatrix} \boldsymbol{R}^u + \delta\gamma_\delta \partial G_{\boldsymbol{T}} \\ \boldsymbol{R}^q + \delta\gamma_\delta \boldsymbol{h}^q \end{bmatrix} \tag{5.37}$$

and the increment of jump plastic displacement is updated as $[\![\delta \boldsymbol{u}^p]\!] = (\boldsymbol{K}^p)^{-1} \cdot \delta \boldsymbol{T}$. The variables may then be updated as in Eq.(5.25), where in addition now we update the traction as $\boldsymbol{T}^{k+1} = \boldsymbol{T}^k + \delta \boldsymbol{T}$.

5.4 Numerical examples

To test the numerical implementations, constrained shear and pure tension simulations are conducted. The FE and CSE meshes are shown in Fig.5.1. These tests involved two FEs and one CSE in between the FEs.

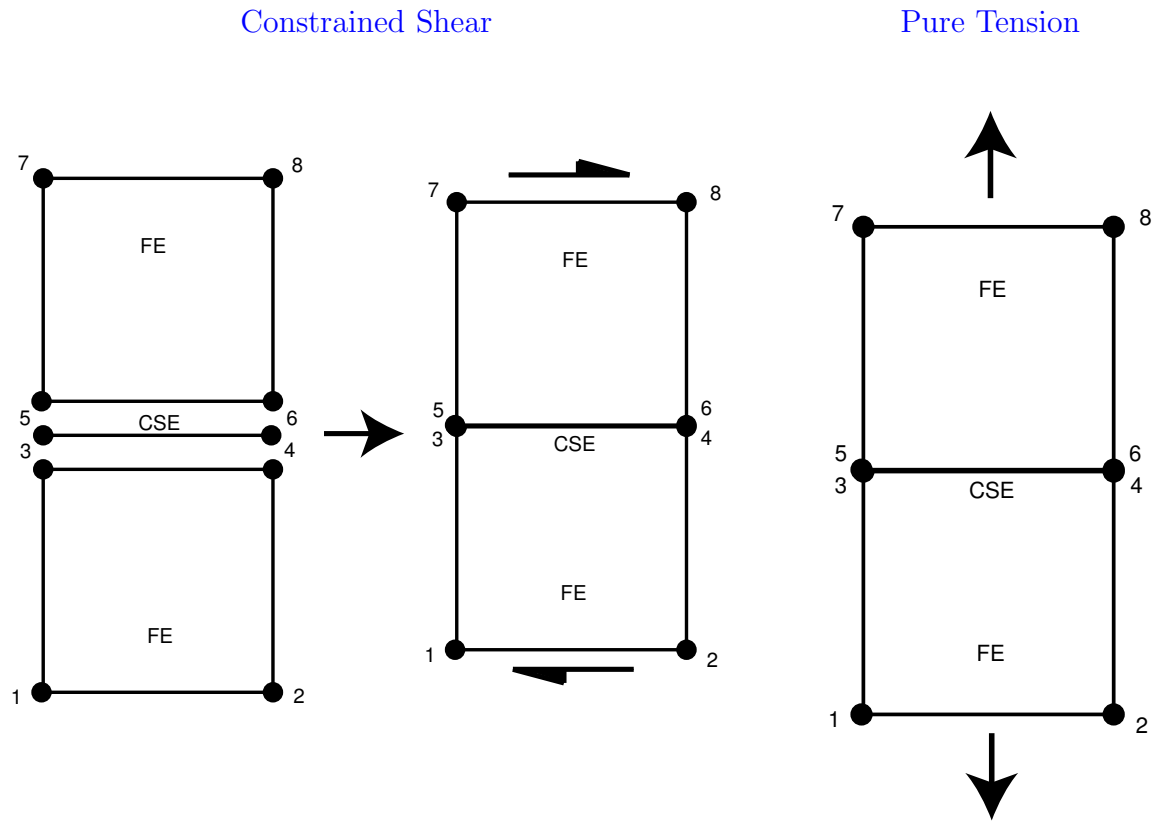

Figure 5.1. Numerical examples to test CSE implementation

5.4.1 Elasto-plastic examples

First, we'll consider the elasto-plastic model. Fig.5.2 shows the stress path in the T_t vs T_n plane, the left plot in Fig.5.3 shows the T_t vs. u_t plot, while the right shows T_n vs. u_t plot.

Table 5.1. Parameters for CSE geomaterial examples

Symbol	Value
E_n	1000
E_t	1000
G_f^I	2
G_f^{II}	1
χ_p	3
χ_r	0.1
c_p	4.5
c_r	0
ϕ_p	0.72
ϕ_r	0.58
ψ_p	0.72
α_χ	100
α_c	10
α_ϕ	10
α_ψ	10

Recall for constrained shear the normal displacement is held fixed $u_n = 0$. The evolution of internal variables for constrained shear are shown in Fig.5.4.

For the pure tension case, only normal T_n develops and softens, along with the internal variable χ. All other variables are zero. The stress path in Fig.5.5 shows the pure tension path in red, and the successively softening green yield surfaces. The path is such that the normal traction T_n moves to the right until it encounters the outer yield surface in green, and then moves to the left as it softens while staying on the yield surface. The T_n vs. u_n is shown in Fig.5.6, and the evolution of χ in Fig.5.7.

5.4.2 Rigid-plastic example

For the rigid-plastic model, imagine the elastic moduli $E_n \to \infty$ and $E_t \to \infty$, i.e. the stiffnesses are infinite. From a computational standpoint, this would lead to an ill-conditioned global stiffness matrix as the CSE stiffnesses would be much larger than the FE stiffness. If choosing a penalty parameter type implementation for the rigid-plastic model, to essentially hold the CSE interface together until yield is reached, we would expect difficulty converging to a solution. This was our initial attempt at the implementation of the rigid-plastic model.

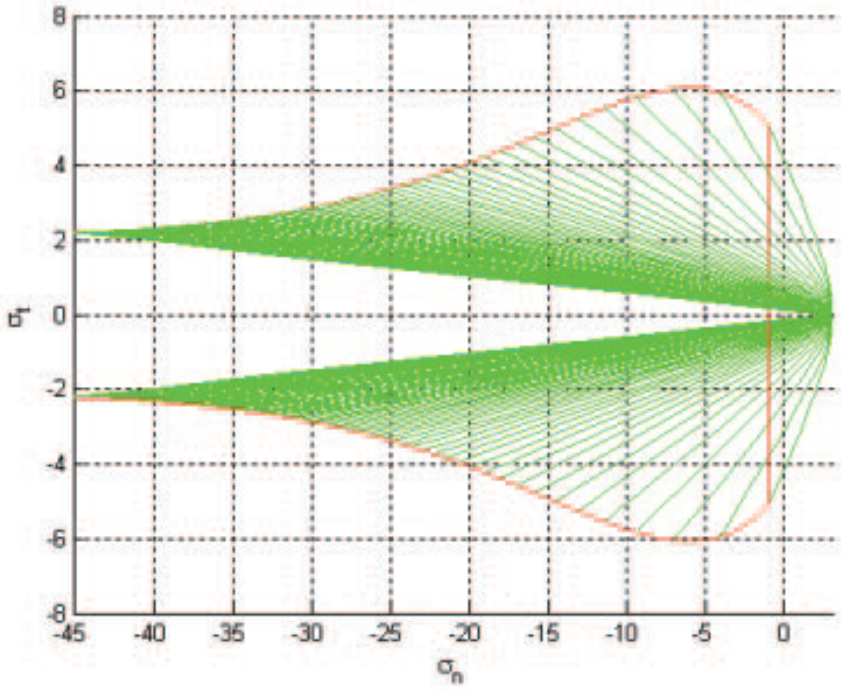

Figure 5.2. Constrained shear stress paths in positive and negative shear. σ is used on the axes in place of T for normal n and trangential t tractions. The red line represents the stress path, and the green curves the successive yield surfaces.

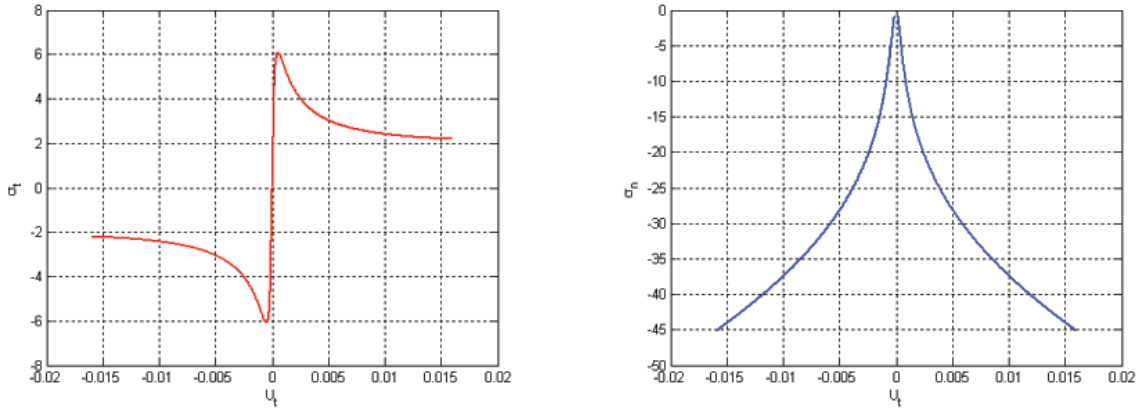

Figure 5.3. Constrained shear stress versus tangential displacement u_t in positive and negative shear. Both the normal n and tangential t tractions are softening.

Work is underway to use a Lagrange multiplier, which we expect would be more stable numerically [32]. Given the numerical instability associated with using a penalty approach,

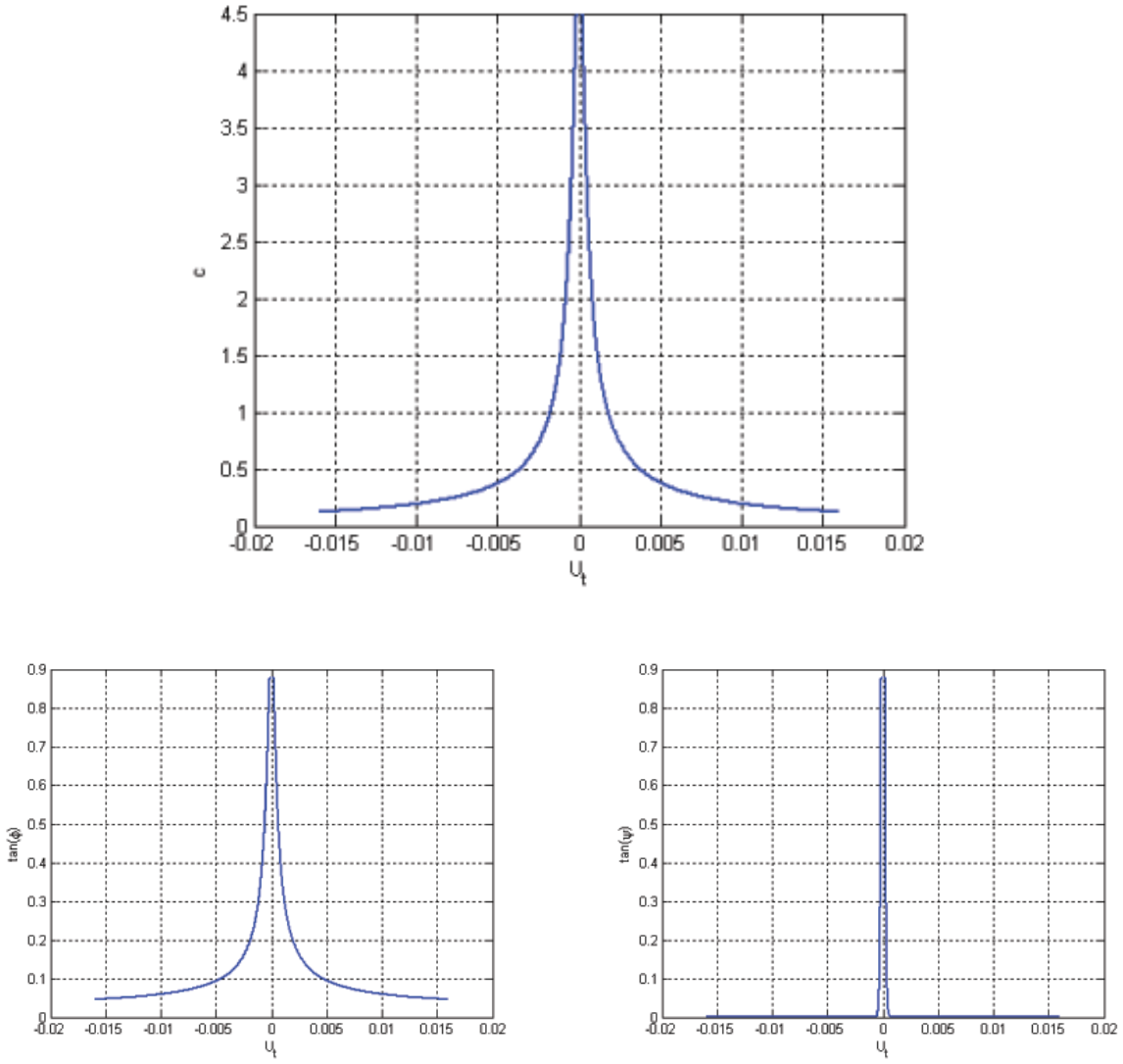

Figure 5.4. Internal variable evolution for positive and negative constrained shear simulation. Top plot shows cohesion softening, middle shows friction angle softening, and bottom shows dilation angle softening. The tension variable χ does not softening for constrained shear because the tension side of the yield surface is not encountered.

we were only able to generate results for pure tension, and not constrained shear. The traction softening result is shown in Fig.5.8.

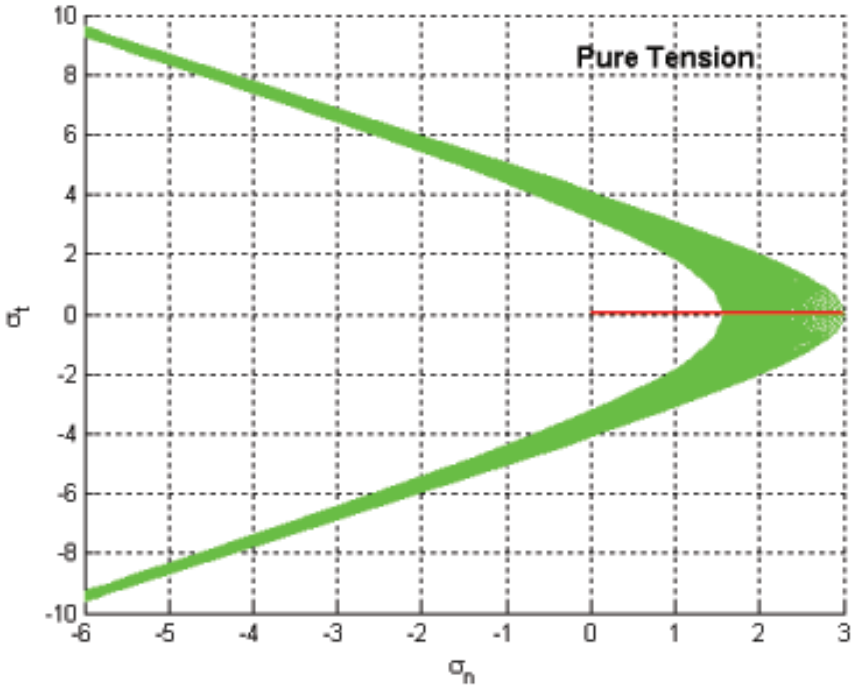

Figure 5.5. Pure tension stress path.

5.5 Conclusion

This chapter described the implicit integration and CSE implementation of a cohesive zone (traction-displacement) model for geomaterials. We envision using such an implementation **after** a discontinuity has been adaptively embedded in a finite element to avoid remeshing, and when the element deformation is such that the element Jacobian approaches zero, the element will be split into two or however many elements is required, and then a CSE is inserted at the element interface. The next chapter describes the embedded discontinuity formulation and implementation. Transition to remeshing and insertion of CSEs is left for future work.

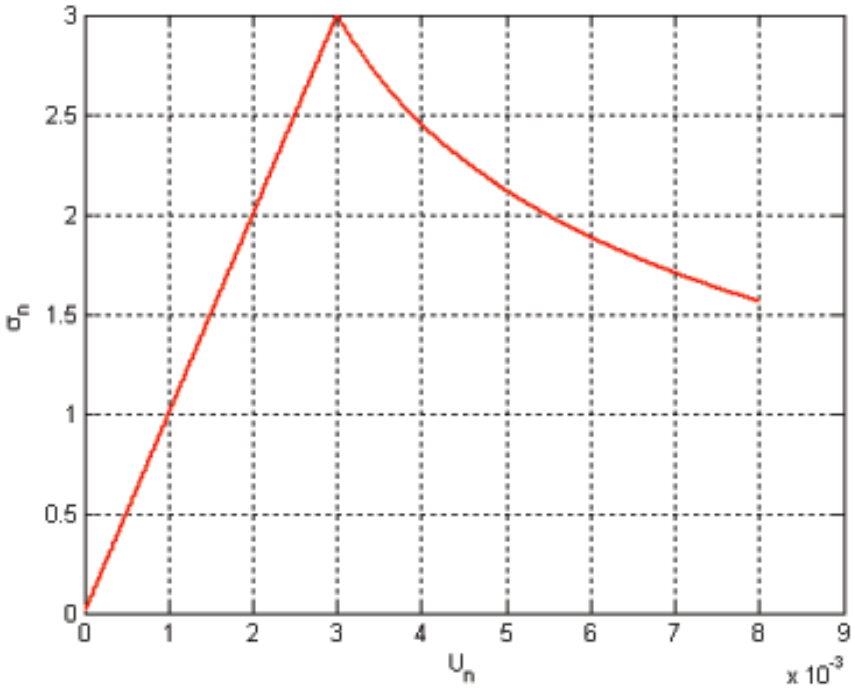

Figure 5.6. Pure tension traction T_n vs u_n.

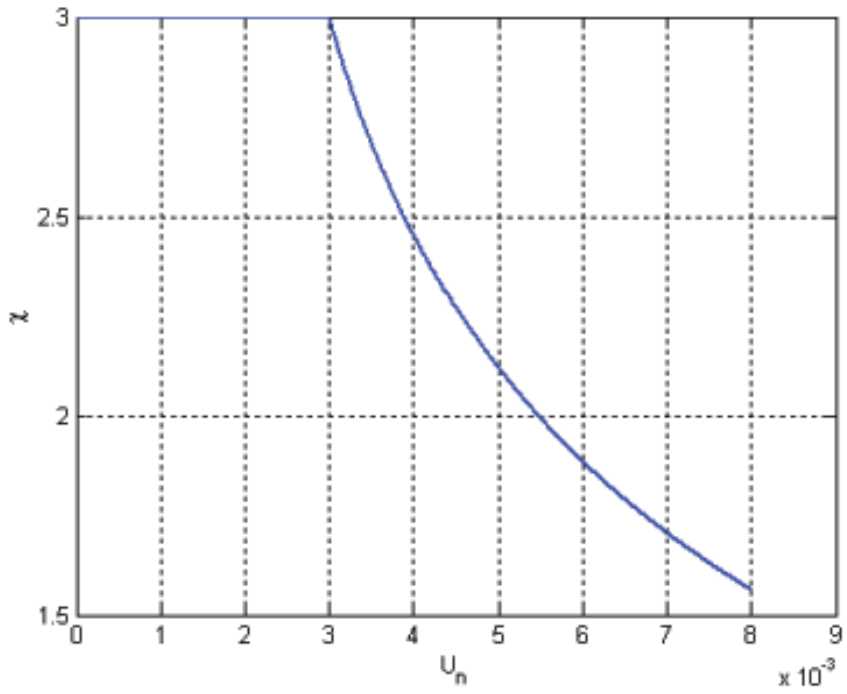

Figure 5.7. Softening of internal variable χ for pure tension. It holds at its initial value until the yield surface is reached.

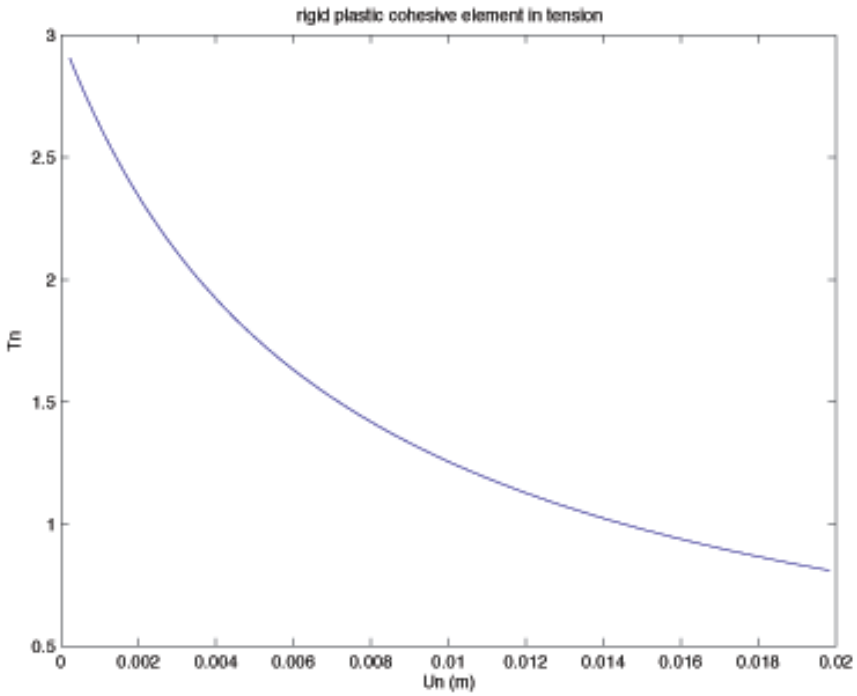

Figure 5.8. Normal traction T_n versus normal displacement u_n for pure rigid-plastic tension. Notice there is no elastic region. The internal tension variable χ would softening similarly to the traction curve shown here.

Chapter 6

Embedded discontinuity finite element implementation

Author: R.A. Regueiro

This chapter describes an embedded strong discontinuity finite element implementation using an assumed enhanced strain method [64, 61]. We will start with the Petrov-Galerkin form for the three-field variational equations, discuss an orthogonality condition and patch test, describe the embedded discontinuity enhancement function for 3D, express the traction-displacement relation in weak form using method of weighted residuals, linearize for iterative solution, and present some numerical examples to demonstrate the implementation.

6.1 Petrov-Galerkin form for three-field variational equations

We start by writing the Petrov-Galerkin variational equations that are derived from the three-field variational form [64, 63, 47]

$$\int_{\Omega^h} \boldsymbol{\nabla}\tilde{\boldsymbol{w}}^h : \boldsymbol{\sigma}^h dv = \int_{\Omega^h} \tilde{\boldsymbol{w}}^h \cdot \boldsymbol{b} dv + \int_{\Gamma_t^h} \tilde{\boldsymbol{w}}^h \cdot \boldsymbol{t}^\sigma da \tag{6.1}$$

$$\int_{\Omega^h_{\rm loc}} \hat{\boldsymbol{\gamma}}^h : \boldsymbol{\sigma}^h dv = 0 \tag{6.2}$$

where $\tilde{\boldsymbol{w}}^h$ is the compatible part of the weighting function, $\boldsymbol{\sigma}^h$ the Cauchy stress, $\boldsymbol{b}$ the body force, $\boldsymbol{t}^\sigma$ the applied traction, $\Omega^h_{\rm loc}$ the domain in which elements have localized, and $\hat{\boldsymbol{\gamma}}^h$ the

enhanced strain variation. Equation (6.1) is the standard balance of linear momentum, and Eq.(6.2) is known as the orthogonality condition. We will use the orthogonality condition when writing our traction-displacment model in weak form, and the patch test will need to pass in order to ensure convergence.

6.1.1 Orthogonality condition

From [8], we assume an enhanced strain variation that must satisfy the orthogonality condition

$$\hat{\boldsymbol{\gamma}}^h = \eta^h \left(\frac{\delta_{\mathcal{S}^h}}{A_{\mathcal{S}^h}} - \frac{1}{V^h_{\text{loc}}} \right) \hat{\boldsymbol{H}}^h \tag{6.3}$$

where η^h is a scalar weighting function, $\delta_{\mathcal{S}^h}$ is the Dirac-delta function at $\mathcal{S}^h$, $A_{\mathcal{S}^h}$ is the area of $\mathcal{S}^h$, V^h_{loc} is the localized volume, and $\hat{\boldsymbol{H}}^h$ is an arbitrary second order tensor that will be chosen based on the choice of traction-displacement model [8]. Given Eq.(6.3), the orthogonality condition reads

$$\frac{1}{A_{\mathcal{S}^h}} \int_{\mathcal{S}^h} \eta^h \hat{\boldsymbol{H}}^h : \boldsymbol{\sigma}^h da - \frac{1}{V^h_{\text{loc}}} \int_{\Omega^h_{\text{loc}}} \eta^h \hat{\boldsymbol{H}}^h : \boldsymbol{\sigma}^h dv = 0 \tag{6.4}$$

Note that $1/A_{\mathcal{S}^h}$ and $1/V^h_{\text{loc}}$ can be placed outside the integral because for small deformations the current areas and volumes approximately equal the reference ones. For finite deformations, this would not be the case [61].

6.1.2 Patch test

In [67], the patch test essentially states that constant stress fields must be admissible in the solution space. This means to say that if $h \to 0$, as the finite elements reduce in size to a point, the finite element solution must approach the exact solution of the partial differential equation, which at a point has a constant stress value. Here, this can be stated as $\boldsymbol{\sigma}^h = \boldsymbol{\sigma}_0$, where $\boldsymbol{\sigma}_0$ is constant, and then the orthogonality condition reads [64, 61]

$$\left[\int_{\Omega^h_{\text{loc}}} \hat{\boldsymbol{\gamma}}^h dv \right] : \boldsymbol{\sigma}_0 = 0 \tag{6.5}$$

which is satisfied if

$$\int_{\Omega^h_{\text{loc}}} \hat{\boldsymbol{\gamma}}^h dv = \mathbf{0} \tag{6.6}$$

which, when substituting Eq.(6.3), leads to

$$\frac{1}{A_{\mathcal{S}^h}} \int_{\mathcal{S}^h} \eta^h \hat{\boldsymbol{H}}^h da - \frac{1}{V^h_{\text{loc}}} \int_{\Omega^h_{\text{loc}}} \eta^h \hat{\boldsymbol{H}}^h dv = 0 \tag{6.7}$$

For constant η^h and $\hat{\boldsymbol{H}}^h$ within a localized element e, this condition would be satisfied trivially, and then the patch test would pass. For generality, however, we leave this condition as it is because in the future we would like to consider non-constant ζ on $\mathcal{S}^h$ and in Ω^h_{loc}. For most enhanced strain implementations of embedded strong discontinuities [62, 63, 2, 8, 47], it is assumed these values are constant, and we will assume the same in this chapter. If not treated as constant, Eq.(6.7) would be an additional constraint on η^h and $\hat{\boldsymbol{H}}^h$.

6.2 Embedded discontinuity enhanced function

To complete the embedded strong discontinuity finite element formulation, the enhancement function $f^e_{\mathcal{S}}$ for a 3D element must be determined. For linear tetrahedral and hexahedral elements, various ways in which a planar strong discontinuity can cut the elements are depicted in Fig.6.1. The procedure for determining the active nodes, and thus the enhancement function $f^e_{\mathcal{S}}$ is shown in Fig.6.2. With coordinates of a point $\boldsymbol{x}^s$ on the discontinuity surface $\mathcal{S}^e$ for element e, and with the normal to the surface $\boldsymbol{n}$, we can determine an active node by the following: if $\boldsymbol{n} \cdot (\boldsymbol{x}^A - \boldsymbol{x}^s) > 0$ then node A is active where $\boldsymbol{x}^A$ is the location of node A. This procedure should work for higher order elements as well, although the procedure is not tested in this chapter for higher order tetrahedral and hexahedral elements.

6.3 Treating strong discontinuity as contributing to enhanced strain

In order for the plastic dissipation to be defined and stress to remain regular (as opposed to singular), certain conditions on the internal variables and stress result [62, 47]. For the

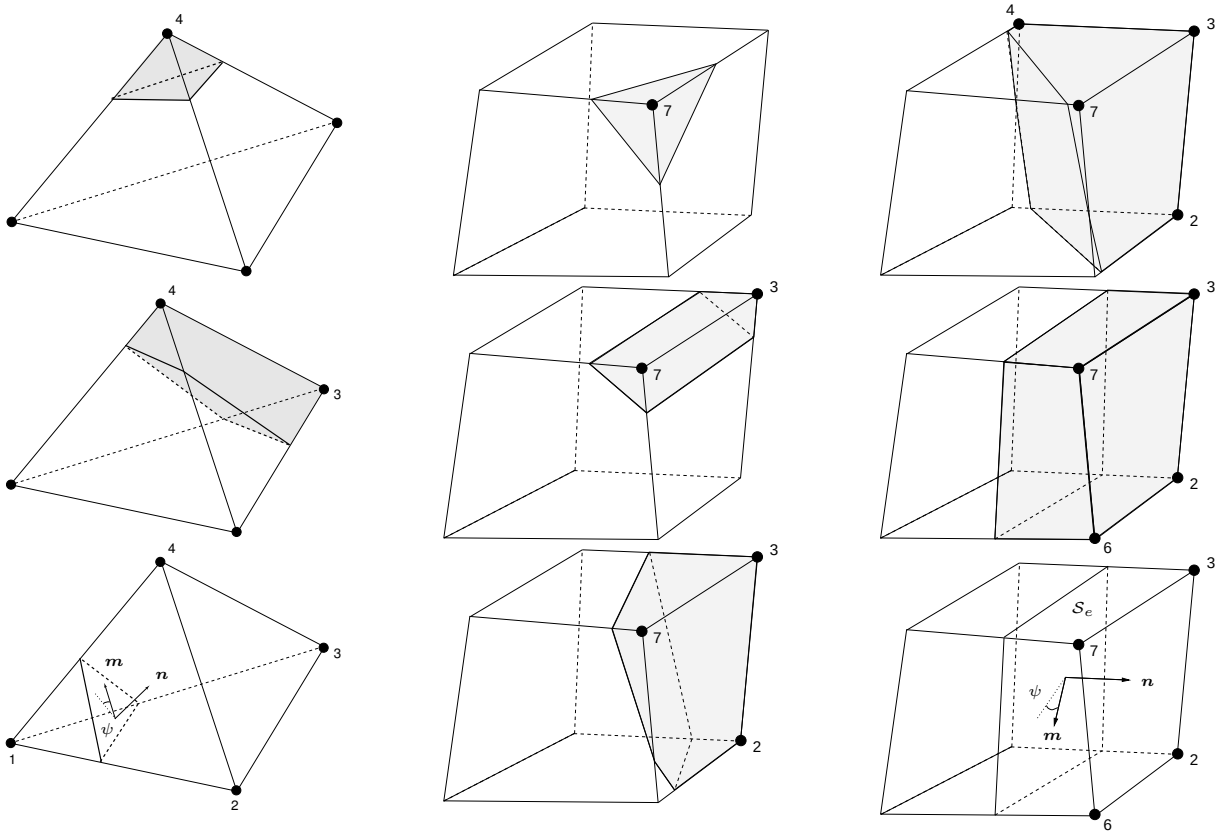

Figure 6.1. Embedded strong discontinuity linear hexahedral and tetrahedral finite elements.

$$f^e_{\mathcal{S}}(\boldsymbol{x}) = \sum_{B=1}^{n_{\text{active}}} N^B(\boldsymbol{x})$$

$$\boldsymbol{\nabla} f^e_{\mathcal{S}}(\boldsymbol{x}) = \sum_{B=1}^{n_{\text{active}}} \boldsymbol{\nabla} N^B(\boldsymbol{x})$$

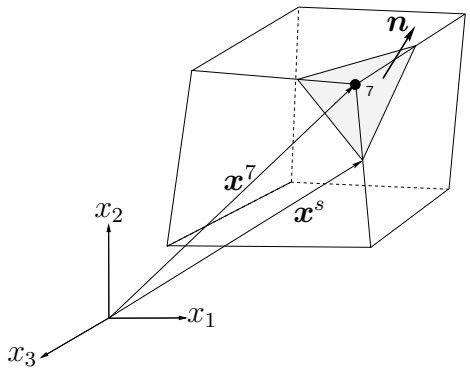

Figure 6.2. Determination of active nodes and embedded strong discontinuity enhancement function $f^e_{\mathcal{S}}$.

plastic dissipation to be defined, it turns out the inverse of the softening modulus (for strain softening plasticity) must be singular, leading to a regular internal variable [62]. In turn, for the stress $\boldsymbol{\sigma}$ to be regular, its singular part must be zero, which constrains the form of the post-bifurcation, traction-displacement model [8, 47]. In the end, given the enhanced strain field and that the compatible displacement $\tilde{\boldsymbol{u}}^h$ is treated as the total displacement at the

nodes, the enhancement function appears in the stress evolution equation [62], which when integrated is

$$\boldsymbol{\sigma}^h = \boldsymbol{\sigma}^{\mathrm{tr}} - \boldsymbol{c}^e : (\boldsymbol{m} \otimes \boldsymbol{\nabla} f^e_{\mathcal{S}}) \langle \Delta\zeta \rangle \tag{6.8}$$

where $\boldsymbol{\sigma}^{\mathrm{tr}}$ is the trial stress, $\boldsymbol{c}^e$ is the fourth order, linear, isotropic elasticity tensor [60], $\langle \bullet \rangle$ is the Macaulay bracket, $\Delta\zeta = \zeta_{n+1} - \zeta_n$, and $\boldsymbol{m}$ is the direction of the jump displacement as

$$\boldsymbol{m} = \mathrm{sign}(T_{\mathrm{t}}) \cos\psi \boldsymbol{t} + \sin\psi \boldsymbol{n} \tag{6.9}$$

6.4 Weak form of traction-displacement model

6.4.1 Implicit integration of traction-displacement model

For implementation by the embedded strong discontinuity element discussed in this chapter, the traction-displacement model discussed in Sect. 4.1 is integrated here using a Backward Euler scheme.

For cleaner presentation, variables at the current time step $(\bullet)_{n+1}$ do not have the subscript, whereas those at the past time step $(\bullet)_n$ do.

The vector of internal variables $\boldsymbol{q}$ is integrated as

$$\boldsymbol{q} = \boldsymbol{q}_n + \boldsymbol{h}_q \langle \Delta\zeta \rangle \tag{6.10}$$

where

$$\boldsymbol{h}_q = \begin{bmatrix} h_c \\ h_\phi \\ h_\psi \end{bmatrix} = \begin{bmatrix} -\alpha_c(c_p - c_r)\exp[-\alpha_c\gamma_\delta]\cos\psi \\ -\alpha_\phi(\phi_p - \phi_r)\exp[-\alpha_\phi\gamma_\delta]\cos\psi \\ -\alpha_\psi\psi_p \exp[-\alpha_\psi\gamma_\delta]\cos\psi \end{bmatrix} \tag{6.11}$$

and

$$\gamma_\delta = (\gamma_\delta)_n + \cos\psi \, \langle \Delta\zeta \rangle \tag{6.12}$$

Note the Macaulay bracket on $\Delta\zeta$. It is possible numerically that, especially at the onset of localization, just as bifurcation is detected, that during the numerical iteration process, the value of ζ could oscillate slightly, and $\langle \Delta\zeta \rangle$ ensures that ζ is always positive. Once ζ begins to evolve along the discontinuity surface $\mathcal{S}$, the oscillations no longer occur. The direction of jump displacement $[\![\boldsymbol{u}]\!] = \zeta \boldsymbol{m}$ is handled by the direction $\boldsymbol{m}$ as defined in Eq.(6.9).

6.4.2 Method of Weighted Residuals

Taking the traction-displacement model in Sect. 4.1, we can rewrite the yield function as

$$\begin{aligned} F &= (\boldsymbol{\mu}^\phi \otimes \boldsymbol{n}) : \boldsymbol{\sigma} - c = 0 && (6.13) \\ & \boldsymbol{\mu}^\phi = \text{sign}(T_\text{t})\boldsymbol{t} + (\tan\phi)\text{sign}(T_\text{n}^*)\boldsymbol{n} && (6.14) \end{aligned}$$

where

$$\text{sign}(T_\text{n}^*) = \begin{cases} 0 & T_\text{n}^* > 0 \quad \text{tension} \\ 1 & T_\text{n}^* < 0 \quad \text{compression} \end{cases} \tag{6.15}$$

Applying the Method of Weight Residuals to Eq.(6.13), expressing in Galerkin form [27], and dividing by $A_{\mathcal{S}^h}$, we have

$$\frac{1}{A_{\mathcal{S}^h}} \int_{\mathcal{S}^h} \eta^h \left[(\boldsymbol{\mu}^\phi \otimes \boldsymbol{n}) : \boldsymbol{\sigma} - c \right] da = 0 \tag{6.16}$$

If we choose $\hat{\boldsymbol{H}}^h = (\boldsymbol{\mu}^\phi \otimes \boldsymbol{n})$, and we assume η^h is constant over $\mathcal{S}^h$ (which will lead to a constant jump displacement ζ over $\mathcal{S}^h$ [62]), we can write the weak form as

$$\frac{1}{A_{\mathcal{S}^h}} \int_{\mathcal{S}^h} \hat{\boldsymbol{H}}^h : \boldsymbol{\sigma} da \; - \; c \; = 0 \tag{6.17}$$

Recall the orthogonality condition with constant η^h

$$\frac{1}{A_{\mathcal{S}^h}}\int_{\mathcal{S}^h}\hat{\boldsymbol{H}}^h:\boldsymbol{\sigma}^h da=\frac{1}{V^h_{\rm loc}}\int_{\Omega^h_{\rm loc}}\hat{\boldsymbol{H}}^h:\boldsymbol{\sigma}^h dv \tag{6.18}$$

which means we can write the weak form as an integration over the volume of the element, allowing us to use the stresses evaluated at the Gauss points to calculate the traction $\boldsymbol{T}$ along $\mathcal{S}^h$.

In summary, the complete weak form written as residuals is

$$R(\boldsymbol{\sigma}) = \int_{\Omega^h}\boldsymbol{\nabla}\tilde{\boldsymbol{w}}^h:\boldsymbol{\sigma}^h dv-\int_{\Omega^h}\tilde{\boldsymbol{w}}^h\cdot\boldsymbol{b}dv-\int_{\Gamma^h_t}\tilde{\boldsymbol{w}}^h\cdot\boldsymbol{t}^\sigma da=0 \tag{6.19}$$

$$r(\boldsymbol{\sigma},\boldsymbol{q}) = \frac{1}{V^h_{\rm loc}}\int_{\Omega^h_{\rm loc}}\hat{\boldsymbol{H}}^h:\boldsymbol{\sigma}dv\ -\ c=0 \tag{6.20}$$

We will take advantage of the fact that ζ is discontinuous between elements, a result of the assumed enhanced strain implementation, and condense out the Eq.(6.20) when solving for the displacements at the nodes.

6.4.3 Yield check along $\mathcal{S}^h$

We calculate the trial yield value along $\mathcal{S}^h$ by

$$F^{\rm trial} = \frac{1}{V^h_{\rm loc}}\int_{\Omega^h_{\rm loc}}(\hat{\boldsymbol{H}}^h)^{\rm trial}:\boldsymbol{\sigma}^{\rm trial}dv\ -\ c_n \tag{6.21}$$

$$(\hat{\boldsymbol{H}}^h)^{\rm trial}=(\boldsymbol{\mu}^{\phi_n}\otimes\boldsymbol{n}) \tag{6.22}$$

$$\boldsymbol{\mu}^{\phi_n}=\text{sign}(T_{\rm t}^{\rm trial})\boldsymbol{t}+(\tan\phi_n)\text{sign}[(T_{\rm n}^*)^{\rm trial}]\boldsymbol{n} \tag{6.23}$$

If $F^{\rm trial}>0$ then there is yielding along $\mathcal{S}^h$, and ζ will evolve. Otherwise, the internal variables and ζ will be held fixed.

6.5 Linearization of finite element equations

Let's first write Eq.(6.19) in finite element matrix form as

$$\boldsymbol{R}(\boldsymbol{\sigma}) = \int_{\Omega^h} \boldsymbol{B}^T \cdot \boldsymbol{\sigma}^h dv - \int_{\Omega^h} \boldsymbol{N}^T \cdot \boldsymbol{b} dv - \int_{\Gamma_t^h} \boldsymbol{N}^T \cdot \boldsymbol{t}^\sigma da = 0 \tag{6.24}$$

where $\boldsymbol{B}$ is the strain-displacement matrix and $\boldsymbol{N}$ the vector of nodal shape functions [27]. When linearizing the residuals in Eqs.(6.24,6.20) about an iteration state k, we have (leaving off $k+1$ for current iteration)

$$\begin{aligned} \delta\boldsymbol{R}(\boldsymbol{\sigma}) &= \frac{\partial \boldsymbol{R}}{\partial \boldsymbol{\sigma}} \cdot \delta\boldsymbol{\sigma} = -\boldsymbol{R}^k & (6.25)\\ \delta r(\boldsymbol{\sigma}, \boldsymbol{q}) &= \frac{\partial r}{\partial \boldsymbol{\sigma}} \cdot \delta\boldsymbol{\sigma} + \frac{\partial r}{\partial \boldsymbol{q}} \cdot \delta\boldsymbol{q} = -r^k & (6.26) \end{aligned}$$

where

$$\begin{aligned} \delta\boldsymbol{\sigma} &= \frac{\partial \boldsymbol{\sigma}}{\partial \boldsymbol{d}} \cdot \delta\boldsymbol{d} + \frac{\partial \boldsymbol{\sigma}}{\partial \boldsymbol{q}} \cdot \delta\boldsymbol{q} + \frac{\partial \boldsymbol{\sigma}}{\partial \zeta}\delta\zeta & (6.27)\\ \delta\boldsymbol{q} &= \frac{\partial \boldsymbol{h}_q}{\partial \boldsymbol{q}} \cdot \delta\boldsymbol{q} \left\langle \Delta\zeta \right\rangle + \frac{\partial \boldsymbol{q}}{\partial \zeta}\delta\zeta & (6.28) \end{aligned}$$

where $\boldsymbol{d}$ is the vector of nodal displacements. When rearranging Eq.(6.28), we find

$$\begin{aligned} \delta\boldsymbol{q} &= \frac{\partial \boldsymbol{q}}{\partial \zeta}\delta\zeta & (6.29)\\ & \frac{\partial \boldsymbol{q}}{\partial \zeta} = \left(\mathbf{1} - \left\langle \Delta\zeta \right\rangle \frac{\partial \boldsymbol{h}_q}{\partial \boldsymbol{q}}\right)^{-1} \cdot \left(\frac{\partial \boldsymbol{h}_q}{\partial \zeta} \left\langle \Delta\zeta \right\rangle + \boldsymbol{h}_q \left\langle \mathrm{sign}(\Delta\zeta) \right\rangle\right) & (6.30) \end{aligned}$$

Skipping some steps, we end up with

$$\begin{aligned} \frac{\partial \boldsymbol{R}}{\partial \boldsymbol{d}} \cdot \delta\boldsymbol{d} + \frac{\partial \boldsymbol{R}}{\partial \zeta}\delta\zeta &= -\boldsymbol{R}^k & (6.31)\\ \frac{\partial r}{\partial \boldsymbol{d}} \cdot \delta\boldsymbol{d} + \frac{\partial r}{\partial \zeta}\delta\zeta &= -r^k & (6.32) \end{aligned}$$

where

$$\frac{\partial \boldsymbol{R}}{\partial \boldsymbol{d}} = \int_{\Omega^h} \boldsymbol{B}^T \cdot \boldsymbol{D}^e \cdot \boldsymbol{B} dv \tag{6.33}$$

$$\frac{\partial \boldsymbol{R}}{\partial \zeta} = \int_{\Omega^h} \boldsymbol{B}^T \cdot \frac{\partial \boldsymbol{\sigma}}{\partial \zeta} dv \tag{6.34}$$

$$\frac{\partial r}{\partial \boldsymbol{d}} = \frac{1}{V^h_{\text{loc}}} \int_{\Omega^h_{\text{loc}}} (\boldsymbol{\mu}^\phi \otimes \boldsymbol{n}) \cdot \boldsymbol{D}^e \cdot \boldsymbol{B} dv \tag{6.35}$$

$$\frac{\partial r}{\partial \zeta} = \frac{1}{V^h_{\text{loc}}} \int_{\Omega^h_{\text{loc}}} (\boldsymbol{\mu}^\phi \otimes \boldsymbol{n}) : \frac{\partial \boldsymbol{\sigma}}{\partial \zeta} dv + \frac{\partial r}{\partial \boldsymbol{q}} \cdot \frac{\partial \boldsymbol{q}}{\partial \zeta} \tag{6.36}$$

and $\boldsymbol{D}^e$ is the matrix form of the elastic modulus tensor $\boldsymbol{c}^e$. Similar to Eq.(6.32),we can also write as

$$\boldsymbol{K}_{dd} \cdot \delta \boldsymbol{d} + \boldsymbol{K}_{d\zeta} \delta \zeta = -\boldsymbol{R}^k \tag{6.37}$$

$$\boldsymbol{K}_{\zeta d} \cdot \delta \boldsymbol{d} + K_{\zeta\zeta} \delta \zeta = -r^k \tag{6.38}$$

and when statically condensing out $\delta\zeta$, we have the following equation to solve for $\delta \boldsymbol{d}$

$$(\boldsymbol{K}_{dd} - K^{-1}_{\zeta\zeta} \boldsymbol{K}_{d\zeta} \otimes \boldsymbol{K}_{\zeta d}) \cdot \delta \boldsymbol{d} = -\boldsymbol{R}^k + (r^k / K_{\zeta\zeta}) \boldsymbol{K}_{d\zeta} \tag{6.39}$$

and with $\delta \boldsymbol{d}$ we can solve for $\delta\zeta$ as

$$\delta \zeta = -(r^k + \boldsymbol{K}_{\zeta d} \cdot \delta \boldsymbol{d}) / K^{-1}_{\zeta\zeta} \tag{6.40}$$

Using this linearization, we then iterate until we reach convergence $\|\boldsymbol{R}^{k+1}\| / \|\boldsymbol{R}^0\| < tol_R$ and $|r^{k+1}| / |r^0| < tol_r$.

Here, more derivatives for the linearization are provided

$$\frac{\partial \boldsymbol{h}_q}{\partial \boldsymbol{q}} = \left[\begin{array}{ccc} \frac{\partial \boldsymbol{h}_q}{\partial c} & \frac{\partial \boldsymbol{h}_q}{\partial \phi} & \frac{\partial \boldsymbol{h}_q}{\partial \psi} \end{array} \right] = \left[\begin{array}{ccc} 0 & 0 & \frac{\partial \boldsymbol{h}_q}{\partial \psi} \end{array} \right] \tag{6.41}$$

$$\frac{\partial \boldsymbol{h}_q}{\partial \psi} = \left[\begin{array}{ccc} \frac{\partial h_c}{\partial \psi} & \frac{\partial h_\phi}{\partial \psi} & \frac{\partial h_\psi}{\partial \psi} \end{array} \right]^T \tag{6.42}$$

$$\frac{\partial h_c}{\partial \psi} = \alpha_c (c_p - c_r) \sin\psi \exp(-\alpha_c \gamma_\delta)(1 - \alpha_c \cos\psi \left\langle \Delta\zeta \right\rangle) \tag{6.43}$$

$$\frac{\partial h_\phi}{\partial \psi} = \alpha_\phi (\phi_p - \phi_r) \sin\psi \exp(-\alpha_\phi \gamma_\delta)(1 - \alpha_\phi \cos\psi \left\langle \Delta\zeta \right\rangle) \tag{6.44}$$

$$\frac{\partial h_\psi}{\partial \psi} = \alpha_\psi \psi_p \sin\psi \exp(-\alpha_\psi \gamma_\delta)(1 - \alpha_\psi \cos\psi \left\langle \Delta\zeta \right\rangle) \tag{6.45}$$

$$\frac{\partial \boldsymbol{h}_q}{\partial \zeta} = \left[\begin{array}{ccc} \frac{\partial h_c}{\partial \zeta} & \frac{\partial h_\phi}{\partial \zeta} & \frac{\partial h_\psi}{\partial \zeta} \end{array} \right]^T \tag{6.46}$$

$$\frac{\partial h_c}{\partial \zeta} = (\alpha_c \cos\psi)^2 (c_p - c_r) \exp(-\alpha_c \gamma_\delta) \left\langle \text{sign}(\Delta\zeta) \right\rangle) \tag{6.47}$$

$$\frac{\partial h_\phi}{\partial \zeta} = (\alpha_\phi \cos\psi)^2 (\phi_p - \phi_r) \exp(-\alpha_\phi \gamma_\delta) \left\langle \text{sign}(\Delta\zeta) \right\rangle) \tag{6.48}$$

$$\frac{\partial h_\psi}{\partial \zeta} = (\alpha_\psi \cos\psi)^2 \psi_p \exp(-\alpha_\psi \gamma_\delta) \left\langle \text{sign}(\Delta\zeta) \right\rangle) \tag{6.49}$$

$$\frac{\partial r}{\partial \boldsymbol{q}} = \left[\begin{array}{ccc} -1 & P^*_{\mathcal{S}} \sec^2\phi & 0 \end{array} \right]^T \tag{6.50}$$

$$P^*_{\mathcal{S}} = \frac{1}{V^h_{\text{loc}}} \int_{\Omega^h_{\text{loc}}} T^*_{\text{n}} dv \tag{6.51}$$

$$\frac{\partial \boldsymbol{\sigma}}{\partial \zeta} = -\boldsymbol{c}^e : \left[\left(\frac{\partial \boldsymbol{m}}{\partial \boldsymbol{q}} \cdot \frac{\partial \boldsymbol{q}}{\partial \zeta} \left\langle \Delta\zeta \right\rangle + \boldsymbol{m} \left\langle \text{sign}(\Delta\zeta) \right\rangle \right) \otimes \boldsymbol{\nabla} f^e_{\mathcal{S}} \right] \tag{6.52}$$

$$\frac{\partial \boldsymbol{m}}{\partial \boldsymbol{q}} = \left[\begin{array}{ccc} \frac{\partial \boldsymbol{m}}{\partial c} & \frac{\partial \boldsymbol{m}}{\partial \phi} & \frac{\partial \boldsymbol{m}}{\partial \psi} \end{array} \right] = \left[\begin{array}{ccc} 0 & 0 & \frac{\partial \boldsymbol{m}}{\partial \psi} \end{array} \right] \tag{6.53}$$

$$\frac{\partial \boldsymbol{m}}{\partial \psi} = -\text{sign}(T_{\text{t}}) \sin\psi \boldsymbol{t} + \cos\psi \boldsymbol{n} \tag{6.54}$$

6.5.1 Linear softening traction-displacement model

The discussion up to this point has been based on an exponential softening traction-displacement model. Here, we present equations for a linear softening model.

The vector of internal variables $\boldsymbol{q}$ is integrated as

$$\boldsymbol{q} = \boldsymbol{q}_n + \boldsymbol{h}_q \langle \Delta\zeta \rangle \tag{6.55}$$

where

$$\boldsymbol{h}_q = \begin{bmatrix} h_c \\ h_\phi \\ h_\psi \end{bmatrix} = \begin{bmatrix} -\alpha_c \cos\psi \\ -\alpha_\phi \cos\psi \\ -\alpha_\psi \cos\psi \end{bmatrix} \tag{6.56}$$

and

$$\gamma_\delta = (\gamma_\delta)_n + \cos\psi \langle \Delta\zeta \rangle \tag{6.57}$$

The derivatives for linearization then become

$$\frac{\partial \boldsymbol{h}_q}{\partial \boldsymbol{q}} = \begin{bmatrix} 0 & 0 & \frac{\partial \boldsymbol{h}_q}{\partial \psi} \end{bmatrix} \tag{6.58}$$

$$\frac{\partial \boldsymbol{h}_q}{\partial \psi} = \begin{bmatrix} \frac{\partial h_c}{\partial \psi} & \frac{\partial h_\phi}{\partial \psi} & \frac{\partial h_\psi}{\partial \psi} \end{bmatrix}^T \tag{6.59}$$

$$\frac{\partial h_c}{\partial \psi} = \alpha_c \sin\psi \tag{6.60}$$

$$\frac{\partial h_\phi}{\partial \psi} = \alpha_\phi \sin\psi \tag{6.61}$$

$$\frac{\partial h_\psi}{\partial \psi} = \alpha_\psi \sin\psi \tag{6.62}$$

$$\frac{\partial \boldsymbol{h}_q}{\partial \zeta} = \boldsymbol{0} \tag{6.63}$$

Numerical examples will present the use of both exponential and linear softening models.

6.5.2 Continuous stress in time at bifurcation point

In order to ensure that the stress is continuous in time at the point of bifurcation, the peak cohesion c_p is calculated as

Table 6.1. Parameters for plane strain compression: post-bifurcation, exponential softening model. Note that the peak cohesion c_p is calculated from Eq.(6.64) in order to ensure that the stress is continuous in time at the point of bifurcation.

Symbol	Value
c_p	calculated
c_r	0 MPa
ϕ_p	0.5236 rad
ϕ_r	0.0 rad
ψ_p	0.087 rad
α_c	1000 1/m
α_ϕ	100 1/m
α_ψ	100 1/m

$$c_p = \frac{1}{V^e_{\text{loc}}} \int_{\Omega^e_{\text{loc}}} \hat{\boldsymbol{H}}^e : \boldsymbol{\sigma}_n dv \tag{6.64}$$

where V^e_{loc} is the localized element volume, Ω^e_{loc} its domain, $\hat{\boldsymbol{H}}^e$ its enhancement function multiplier, and $\boldsymbol{\sigma}_n$ the converged stress from the past time step t_n.

6.6 Numerical examples

Numerical examples include a 3D plane strain compression verification simulation (out-of-plane displacements are fixed), and a 3D corner shear simulation. More complex simulations will be attempted when the discontinuity tracing algorithm is implemented.

6.6.1 3D plane strain compression

To verify that the post-bifurcation model is working (although there is no analytical solution to conduct a true verification), we reconsider the plane strain compression problem as discussed in Sect. 3.6.4, but for rate-insensitivity $\tau = 0$. Parameters for the exponential post-bifurcation traction-displacement model are given in Table 6.1, and for the linear traction-displacement model in Table 6.2.

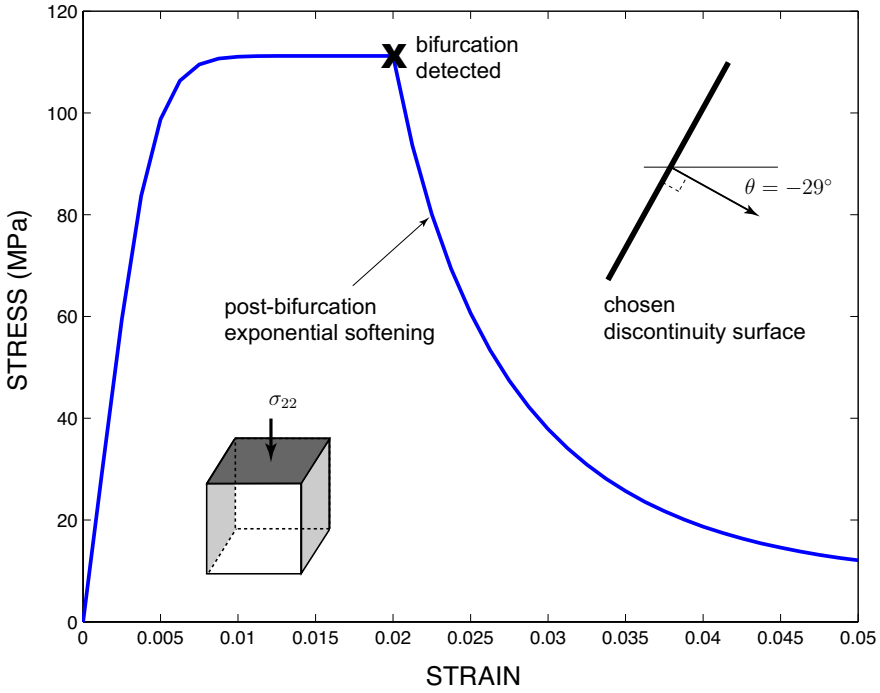

Figure 6.3. Plot of stress versus strain for bifurcation and post-bifurcation analysis (exponential softening) of plane strain compression of Salem Limestone using the Sandia Geomodel. One element 0.04m wide by 0.08m high is used for the simulations. Since there is no asymmetry or inhomogeneity to determine which $\boldsymbol{n}$ to choose as the normal to the discontinuity surface $\mathcal{S}$, we choose the negative angle $-\theta$.

Figure 6.3 demonstrates the post-bifurcation exponential softening for the embedded discontinuity element. Figures 6.4, 6.5, and 6.6 show the cohesion, friction, and dilation exponential softening.

Figure 6.7 demonstrates the post-bifurcation linear softening for the embedded discontinuity element. Figures 6.8, 6.9, and 6.10 show the cohesion, friction, and dilation linear softening.

6.6.2 3D corner shear

For testing the true three-dimensional nature of the embedded discontinuity implementation presented in this chapter, we reconsider the corner shear problem from Sect. 3.6.2. Post-bifurcation, linear softening parameters are given in Table 6.3.

Figure 6.11 demonstrates the post-bifurcation softening for corner shear loading. In this case, only the corner node enhancement function is activated, as indicated in Fig.6.1. This

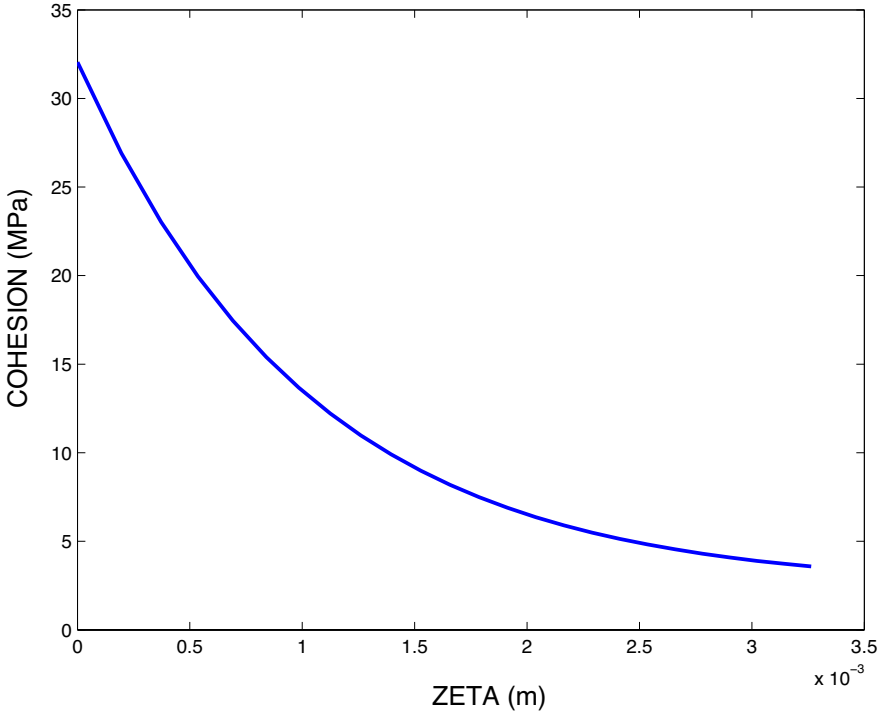

Figure 6.4. Plot of cohesion c versus jump displacement magnitude ζ for bifurcation and post-bifurcation analysis (exponential softening) of plane strain compression of Salem Limestone using the Sandia Geomodel.

Table 6.2. Parameters for plane strain compression: post-bifurcation, linear softening model.

Symbol	Value
c_p	calculated
c_r	0 MPa
ϕ_p	0.5236 rad
ϕ_r	0.0 rad
ψ_p	0.087 rad
α_c	10,000 MPa/m
α_ϕ	100 rad/m
α_ψ	100 rad/m

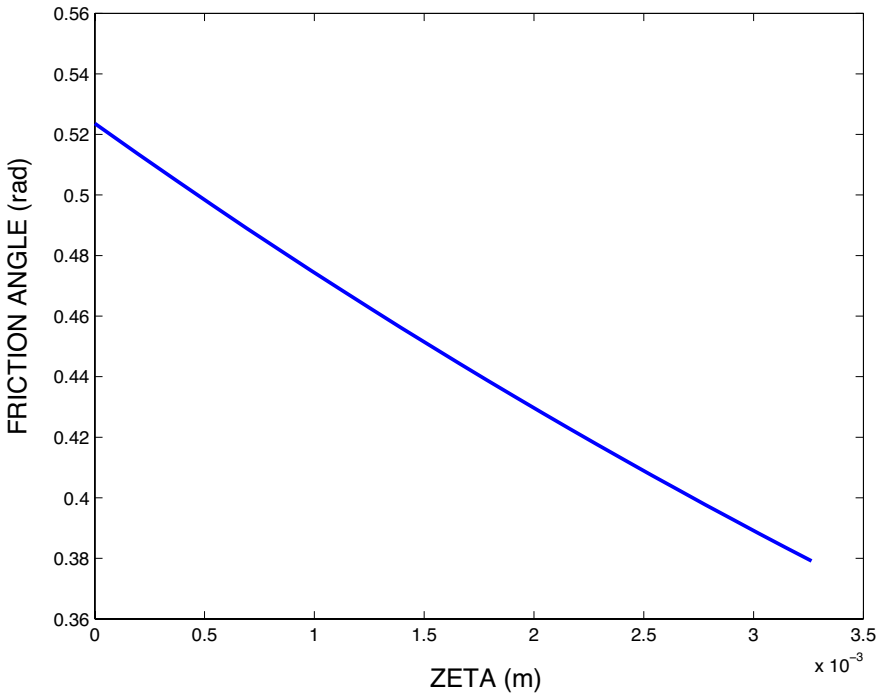

Figure 6.5. Plot of friction angle ϕ versus jump displacement magnitude ζ for bifurcation and post-bifurcation analysis (exponential softening) of plane strain compression of Salem Limestone using the Sandia Geomodel.

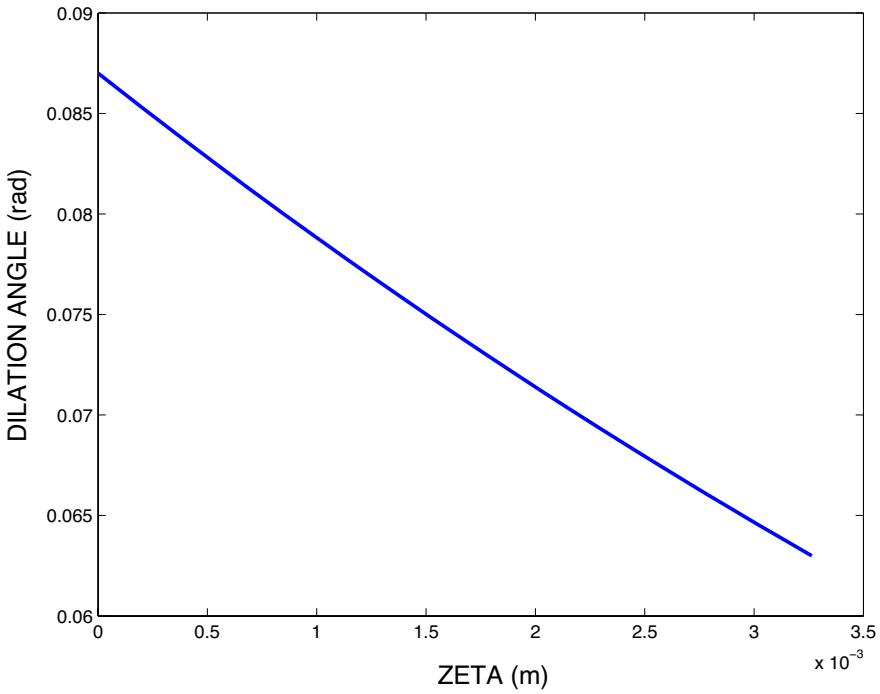

Figure 6.6. Plot of dilation angle ψ versus jump displacement magnitude ζ for bifurcation and post-bifurcation analysis (exponential softening) of plane strain compression of Salem Limestone using the Sandia Geomodel.

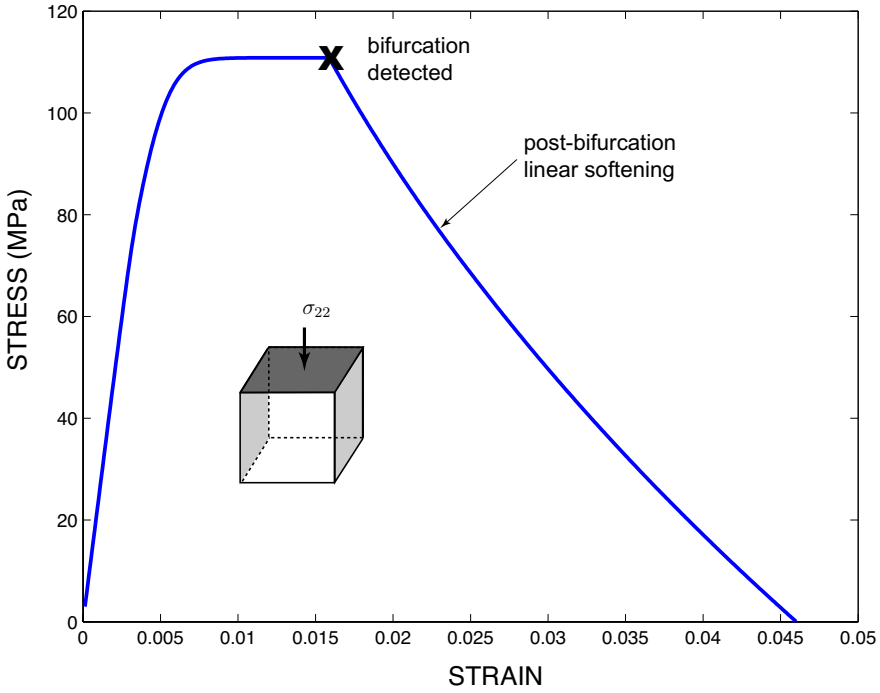

Figure 6.7. Plot of stress versus strain for bifurcation and post-bifurcation analysis (linear softening) of plane strain compression of Salem Limestone using the Sandia Geomodel.

demonstrates a problem that cannot be solved using a 2D plane strain formulation [8].

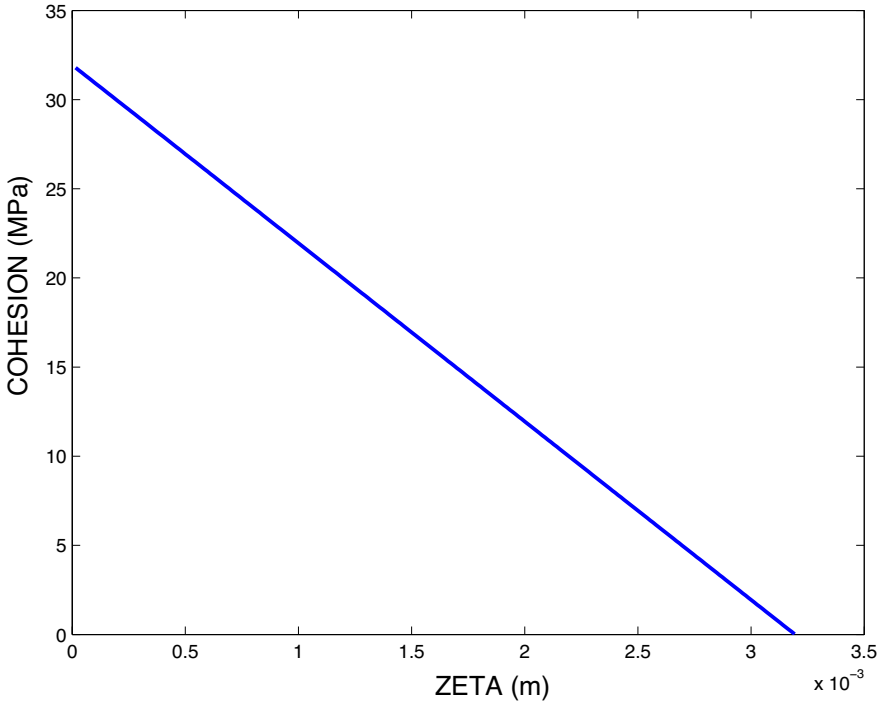

Figure 6.8. Plot of cohesion c versus jump displacement magnitude ζ for bifurcation and post-bifurcation analysis (linear softening) of plane strain compression of Salem Limestone using the Sandia Geomodel.

Table 6.3. Parameters for 3D corner shear: post-bifurcation, linear softening model.

Symbol	Value
c_p	calculated
c_r	0 MPa
ϕ_p	0.5236 rad
ϕ_r	0.0 rad
ψ_p	0.1 rad
α_c	3e8 MPa/m
α_ϕ	1e3 rad/m
α_ψ	1e3 rad/m

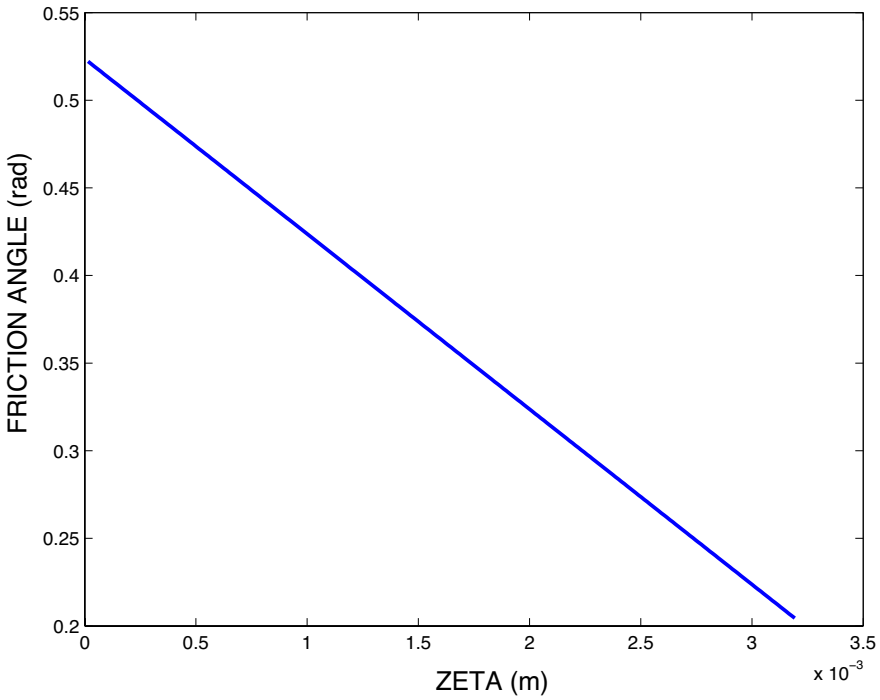

Figure 6.9. Plot of friction angle ϕ versus jump displacement magnitude ζ for bifurcation and post-bifurcation analysis (linear softening) of plane strain compression of Salem Limestone using the Sandia Geomodel.

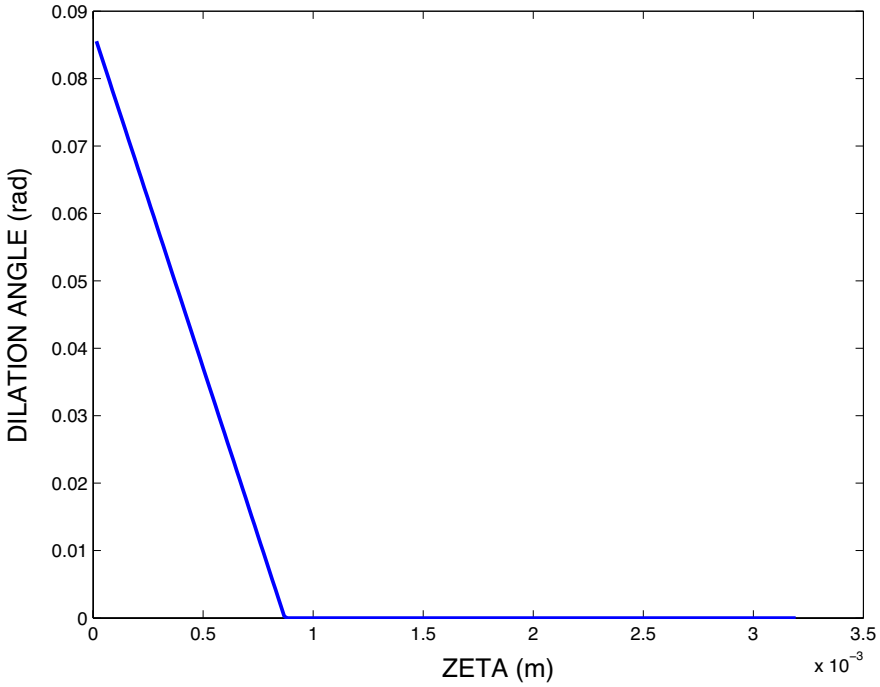

Figure 6.10. Plot of dilation angle ψ versus jump displacement magnitude ζ for bifurcation and post-bifurcation analysis (linear softening) of plane strain compression of Salem Limestone using the Sandia Geomodel.

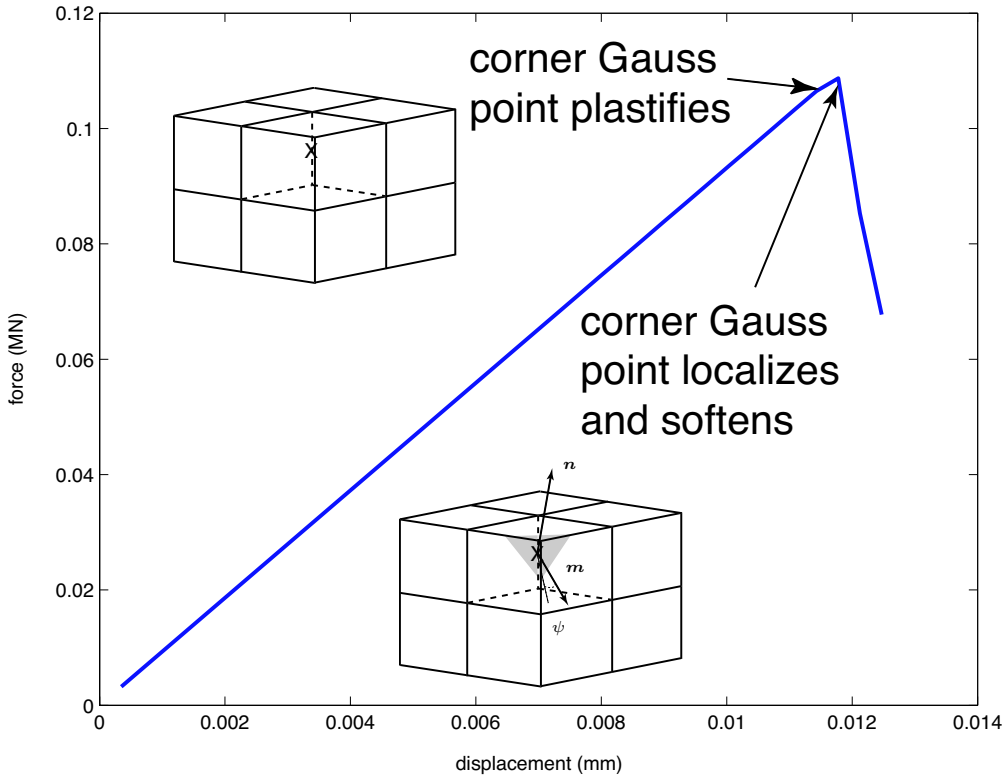

Figure 6.11. Post peak softening in hex for corner shear.

This page intentionally left blank.

Chapter 7

Coupled DEM/FEM

Authors: R.P. Jensen, R.A. Regueiro

7.1 DEM Background

It is appropriate to begin this discussion on the coupling of the finite element method (FEM) and the discrete element method (DEM) with a brief discussion on DEM. The FEM is a well-established, widely utilized numerical simulation technique. In comparison, DEM is not as well known. It is also a much younger numerical technique than FEM. Cundall and Strack published the seminal paper in 1979 [15]. Since that time, DEM has attracted a relatively small community of users. Because of the basic assumption of modeling material using discrete entities, DEM has been widely used to model disaggregated media that occur naturally such as sand, rocks and rock-falls, as well as for modeling material movement in dynamic environments such as the mining industry[13, 46]. It has also been adapted for the modeling of solid geomaterials [45]. The basic underlying assumption of DEM is that material is modeled as an assemblage of distinct, separate bodies that interact through predetermined rules when the bodies come in contact. The bodies are generally assumed to be rigid though there are situations where they can be modeled using deformable bodies. The discrete bodies, often referred to as particles, are generally modeled as disks, in 2D, and as spheres, in 3D, though they can also be modeled as ellipses and ellipsoids or as arbitrary polygons and polyhedrons. When two particles come in contact, the contact interaction in the normal direction is idealized as a spring and dashpot and in the transverse direction, as a spring and dashpot that is active up to the point where sliding between the particles occurs, as can be seen in Fig. 7.1. The particle motion is derived from Newtons law and is as follows:

$$M\ddot{x} + f^{int} = f^{ext} \tag{7.1}$$

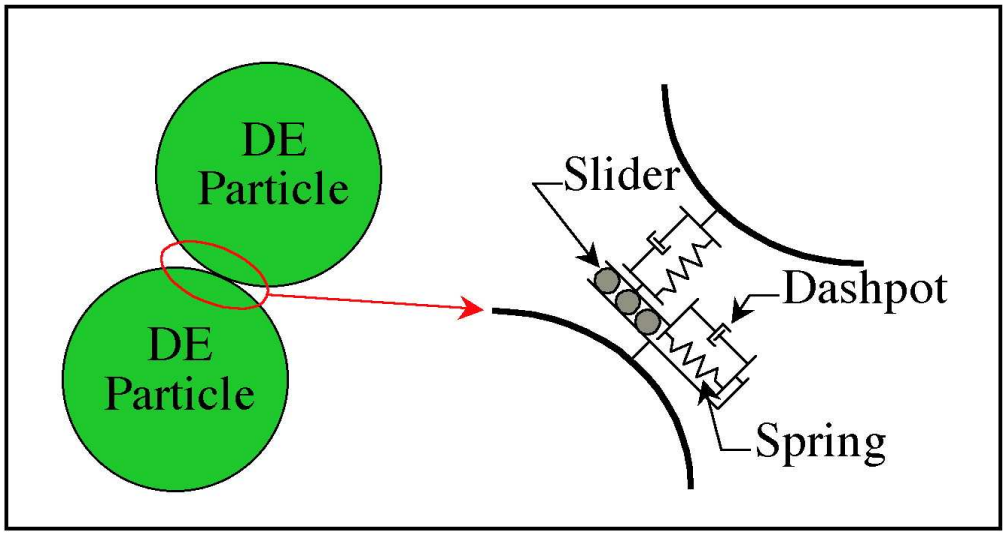

Figure 7.1. Schematic showing the idealized contact between two Discrete Element particles.

where M is the mass of the particle, $\ddot{x}$ is the particle acceleration, f^{int} are the internal forces which include the contact forces, friction forces, attractive forces, viscous forces, etc., and f^{ext} are the external forces which include the particle weight and the far-field tractions. The internal particle contact normal forces are computed as:

$$f_n = K\delta + C\dot{x}_n \tag{7.2}$$

where f_n is the normal force, δ is the inter-particle penetration, C is the damping coefficient, and $\dot{x}_n$ is the relative normal velocity between two particles. The spring constant, K, which derived from the Timoshenko and Goodier [68] relationship for two spheres coming in contact, is defined by:

$$K = \lambda \times \frac{4}{3}\left[\frac{E_1 E_2}{(1+\nu_1^2)E_2 + (1+\nu_2^2)E_1}\right]\left[\frac{R_1 R_2}{R_1 + R_2}\right]^{1/2} \tag{7.3}$$

where K is the spring constant, λ is a constant, E_n are Youngs Moduli for each particle, ν^n are Poissons ratio for each particle and R_n are the particle radii. The transverse forces, f_t, are proportional to the normal forces, f_n, assuming Coulomb friction law to define the friction relationship.

$$f_t \leq \mu f_n \tag{7.4}$$

where μ is the coefficient of friction and f_t is the upper limit of the transverse force.

DEM uses an explicit numerical integration scheme to march through time. Since it is an explicit code, generally speaking, in order to maintain numerical stability, the time step must be quite small. An estimate for the maximum, critical time step, Δt_{cr}, can be found by

$$\Delta t_{cr} = 2\sqrt{\frac{M}{K}} \tag{7.5}$$

where M is the value for the mass of the smallest particle in the simulation and K is the largest value spring constant found above. The critical time step is based on the estimation of the natural frequency of two particles connected by a spring. However, since it is very likely that a particle will be in contact with more than one particle during a time cycle, the actual natural frequency of the particles would be higher which results in a lower critical time step. Generally, an additional factor, on the order of 0.1, is included in the time step estimation in order to account for this difference.

One cycle of computation is as follows. First, determine neighboring particles. Once neighbors are determined, find if there is any contact between particles. This is the lengthiest step. Next, for particles that are touching, compute the contact forces. From the contact forces, the particle accelerations can be computed and the magnitudes of the particle velocities and displacements can be integrated. Then the cycle repeats.

The basic particle-particle contact law is the spring/dashpot model that can be seen in Fig. 7.1. However, depending on the media that is trying to be modeled, the particle-particle contact law can be modified. Simple tensile bonds can be implemented, more elaborate, moment carrying bonds can be implemented, or any other type of internal force relationship that can be numerically modeled can be implemented.

7.2 One-Way FE/DE Coupling

Because DEM uses discrete particles, it is able to naturally characterize materials that undergo large deformations or even dis-aggregation. It is able to do this without any additional or special treatments of the governing equations or controlling algorithms. Additionally, it is very easy to include a high degree of heterogeneity by simply assigning different material

properties to each particle. These are two areas in which continuum based FE modeling techniques falter. However, because of the small critical time step as well as the large number of degrees of freedom, running DEM simulations on any geomechanics problem at a realistic scale would require vast amounts of computer resources and is simply not tractable.

There are two ways to look at FE/DE coupling. The first approach involves tracking material movement, post-failure. As the material fails in one region of the FE mesh and as the material dis-associates from the main body, it is very difficult to track the movement of the material using FEs. The pieces of the mesh that break from the main mesh can easily either become distorted or start out as distorted elements. Also checking all of the potential neighbors and contacts using polygonal shaped objects can require more than one order of magnitude greater computer speeds when compared to a circular or spherical elements. In addition, the contact force calculation for separated polygonal shaped elements is far more complicated than the calculation for circular or spherical discrete elements, in which forces are either normal to or tangential to the element surface. By superimposing DEs over the area of the mesh of the newly separated areas, tracking the movements of the new particle becomes simpler as does checking for all of the potential neighbors and contacts. The second approach calls for the far-field boundary to be modeled with finite elements while the near-field region of interest, where extreme deformations and dis-aggregation are expected, is modeled with discrete elements. During the course of this LDRD, both approaches where investigated. The second approach was successfully accomplished. For the first approach, progress was made but full integration was not achieved. However the major roadblock was related more to database management issues as opposed to theoretical issues. For both cases a modified version of the DEM code DMC (Distinct Motion Code) was used. DMC was developed at Sandia [46].

As mentioned, for the second case, the coupling was not completed. Capability was written in the code that allows for the identification of a separating finite element (FE) and then for the creation of discrete element (DE) particles to be located within the region defined by the boundaries of that FE. Then, the nodal velocities of the FE can be transferred to the newly created DE particles based upon an interpolation of the continuum displacement field of the FE. This interpolation is derived from the FE shape function as will be described shortly. Once the transfer of nodal velocity data from the FE to the DEs, the FE is deleted. All subsequent motions of the DEs are controlled strictly by their individual particle interactions and contact relationships. DMC uses the ExodusII database [57]. One aspect of this database is that it does not allow for an increase of the number of nodes or elements once a calculation has been started. Therefore, in order to fully implement the coupling, described in this second case, in a simulation, a new method for managing the FE/DE model data needs to be implemented. This was not done. Figure 7.2 shows a schematic of what the results of implementing this coupling scheme would look like.

The first approach to coupling FEs with DEs was successfully accomplished. In this ap-

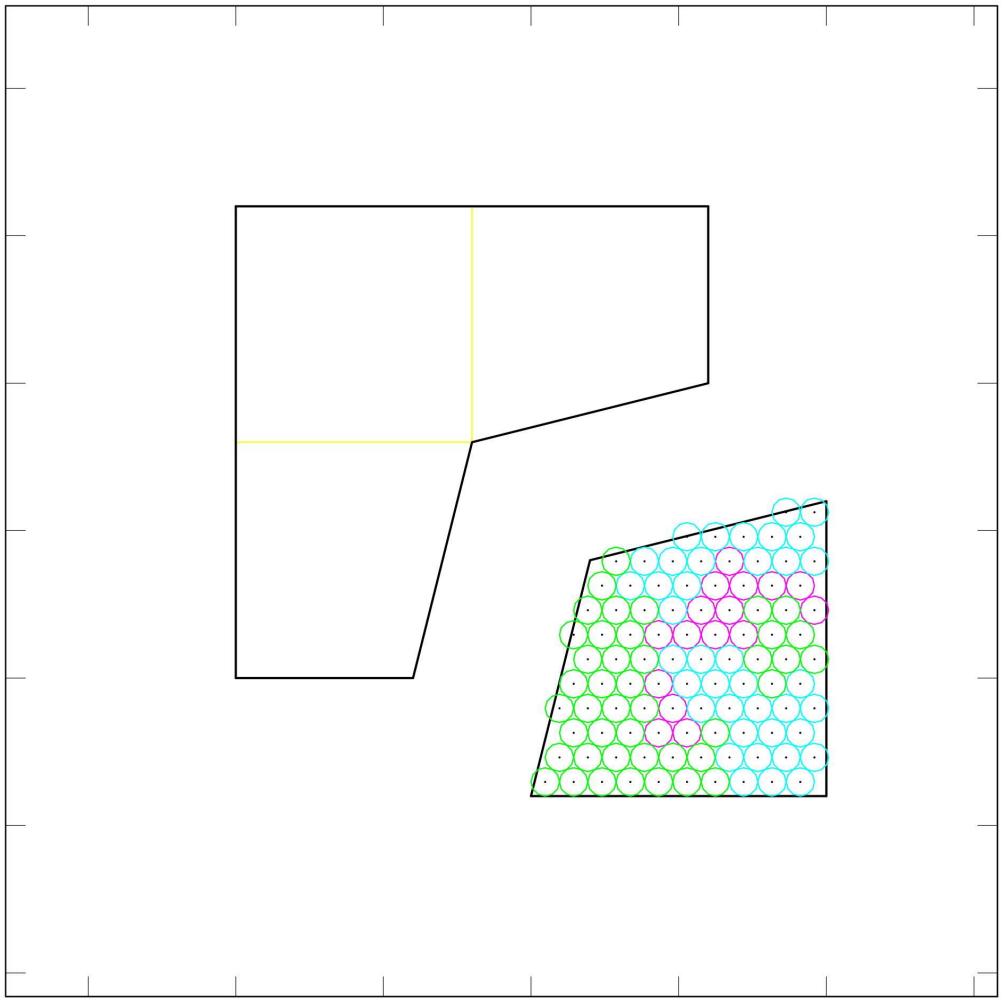

Figure 7.2. Schematic of newly created discrete elements within the boundaries of a newly separated finite element.

proach, the near-field area of interest, where large dis-aggregations and/or extremely large deformations are expected, is modeled with discrete elements. The far-field boundary conditions are modeled using finite elements. Often, deleterious boundary effects can negatively affect the results of a simulation if the boundaries of the simulation are too close to the area of interest. In many geomechanics oriented simulations, the scale of the problem can be in the hundreds of meters. With the present computing capabilities, it is impossible to model such large problems using discrete elements if the area of interest is in the meter range or less. Therefore, by coupling FEs with DEs, the ability to model problems with disparate length scales can be accomplished. For this LDRD, a one-way coupling was accomplished. The basic idea is to model the far-field with finite elements. In the region of interest, discrete elements are modeled. Where the far-field regions interface with the near-field, a region of

overlap is created. Within this region of overlap, discrete elements are super-imposed onto the overlap region of finite elements. The contact/interaction between the super-imposed DEs and the non-super-imposed DEs remains conventional. However, the displacements of the super-imposed DEs are fully prescribed by the nodal displacements of the finite elements occupying the same region. The DE displacements are interpolated from the continuum displacement field of the finite elements. The DE displacement, $\boldsymbol{u}$, can be defined by

$$\boldsymbol{u}(\boldsymbol{x}^{(\alpha)}) = \sum N^{(a)}(\boldsymbol{x}^{(\alpha)})\, \boldsymbol{u}^{(a)} \tag{7.6}$$

where $\boldsymbol{x}^{(\alpha)}$ is the un-deformed position of the DE, $N^{(a)}$ are the shape functions of the finite element and $\boldsymbol{u}^{(a)}$ are the finite element nodal displacements [3]. This results in a one-way coupling between the FE and DE method. The interaction forces between the super-imposed discrete elements and the discrete elements outside the region are not transferred back into the finite element mesh. In order to implement this capability, an explicit finite element solver needed to be added to DMC. Therefore, a very simple, crude FE solver was added. The basis for the solver was adapted from Cook, Malkus, and Plesha[14]. Figure 7.3 shows a simple simulation to demonstrate the one-way coupling effects. The figures show the initial configuration of a cantilevered beam, which has several discrete elements coupled at the end of the beam. A point load is applied at the end of the beam causing it to deflect. As can be seen in right figure of Figure 7.3, as the end of the beam deflects in response to the applied load, the discrete elements accordingly also deflect. This is the expected and correct response for a one-way DE/FE coupling.

To illustrate a potential problem in which this capability might be utilized, a quick sample problem was created. The problem is a tunnel opening in a rock mass. The dimensions of the problem are a rock mass measuring 200 meters by 200 meters. Within the rock mass is a tunnel that is two meters wide by two meters high with an arched ceiling with a radius of one meter. As can be seen in Figure 7.4, the main rock mass was modeled using finite element. The region surrounding the tunnel was modeled using discrete elements. The thickness of the discrete element region was 0.5 meters. The image on the far right of Figure 7.4 shows the overlapping regions of DEs and FEs. This is the region in which the one-way DE/FE coupling takes place. The finite element mesh employed linear elastic bi-linear quadrilateral elements. Within the finite element mesh, there was no mechanism included for failure. For modeling rock, this is probably not the best element to use, however the intent of the sample problem was to demonstrate the coupling between finite elements and discrete elements. The rock material properties were assumed to be similar to a granite with a Youngs modulus, E =75 GPa, Poissons ratio, $\nu = 0.29$, and a unit weight of 2300 kg/m^3. The DEs were modeled with a simple tension bond. The additional material properties of the DEs are a tensile strength of 150 MPa, a compressive strength of 175 MPa, and an internal friction angle of 35°. These values are high and indicate that a better bonding model is needed. In addition, Macro-Particles (see section 7.5) were used to model the DE region. The strength between

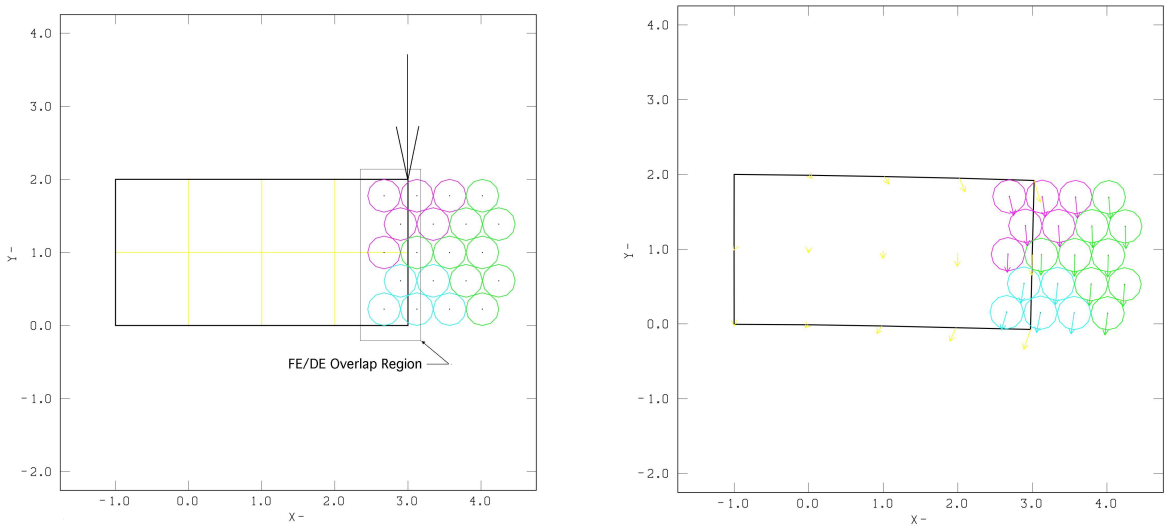

Figure 7.3. Simple cantilever beam, loaded at one end. At the end of the beam, an assemblage of discrete elements is attached. The FE/DE overlap region is highlighted. The arrow indicates the location of the point load. In the right figure, the arrows indicate relative magnitude and direction of the particle displacements.

two macro-particles were reduced by 60 percent. A triangular shaped pulse load was applied to the top of the mass at selected nodes above the location of the tunnel. A horizontal stress of 2.0 MPa was applied to the outer boundary of the model as in situ stresses. The pulse load was applied to the finite element mesh by imposing a velocity profile on selected nodes. The peak load was 16 m/s occurring 0.0005 seconds after initiation, with the velocity going to zero at time 0.003 seconds after initiation. The results of the stress wave propagating past the tunnel can be seen in the Figure 7.5. The image on the left is pre-failure and the image on the right is post-failure. From the post-failure image, the rock can be seen to disaggregate and to do so in manner that has been seen in actual tests. This qualitative behavior gives some confidence that the technique has good potential for modeling post-failure behavior in highly dynamic regions. As was mentioned, there are a number of modeling methodologies and material properties that could be or should be used to improve the FE model such as a better material model, however it is important to keep in mind that the purpose of the simulation was to demonstrate the direct transfer of loads from the FE mesh to the DEs.

The application of one-way DE/FE coupling is fairly limited. The most appropriate application is in the situations described for the second approach where the purpose of the coupling is tracking particles post failure. In cases that are described for the first approach, there are significant loads from the DEs that need to be applied back into the finite element mesh. This is because for this case, the free boundary of the problem is not the finite element boundary but the boundary of the discrete elements. Therefore a preliminary investigation into two-way coupling was conducted to measure the potential for continuation of this work.

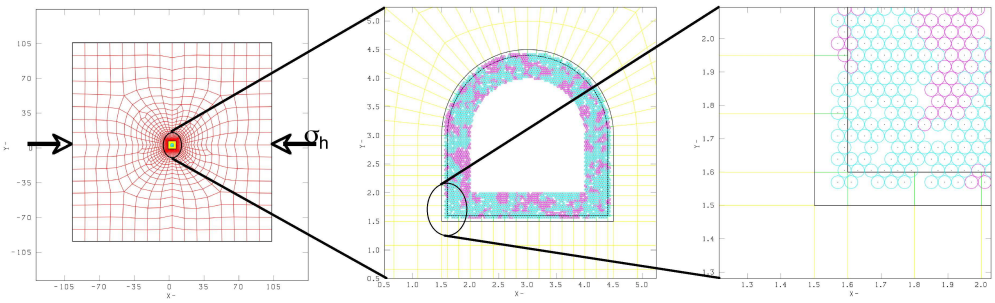

Figure 7.4. This figure shows the coupled FE mesh and DE model used in the example problem. The image on the left shows the entire domain that was modeled. The center image shows the region modeled by the DEs. The image on the right illustrates the FE/DE overlap region.

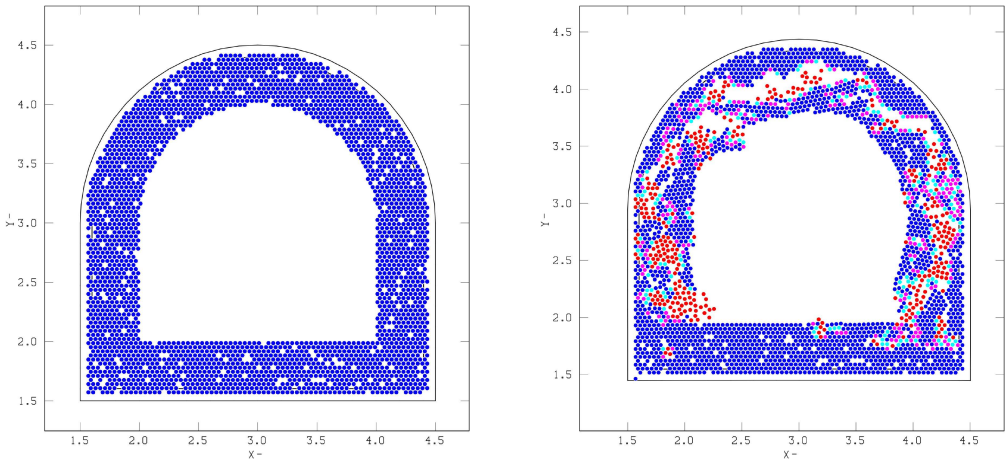

Figure 7.5. These images illustrate the DE region before (image on left) and after (image on right) the stress-wave propagates through the tunnel. The damage to the tunnel can be clearly seen in the figure on the right with large volumes of DEs having separated.

7.3 Two-Way FE/DE Coupling

7.3.1 Overlapping FE/DE domains

The concept of two-way coupling of finite elements and discrete elements could be based on the coupled atomistic-continuum simulation (CACS) approach using arbitrary overlapping domains, developed by Zimmerman et al. [3]. This FE/DE coupling approach will assume that there exists a domain, which includes both FEs and DEs, as seen in Fig. 7.6, where the DE domain intersects the FE domain. The size of this domain will generally be assumed to be only one element deep. Because this overlapping region is the boundary of the FEs but

not of the problem, it is important to transmit the loads stresses and strains in the DEs to the FEs. Adapting the CACS approach to FE/DE should provide a straightforward means of achieving this.

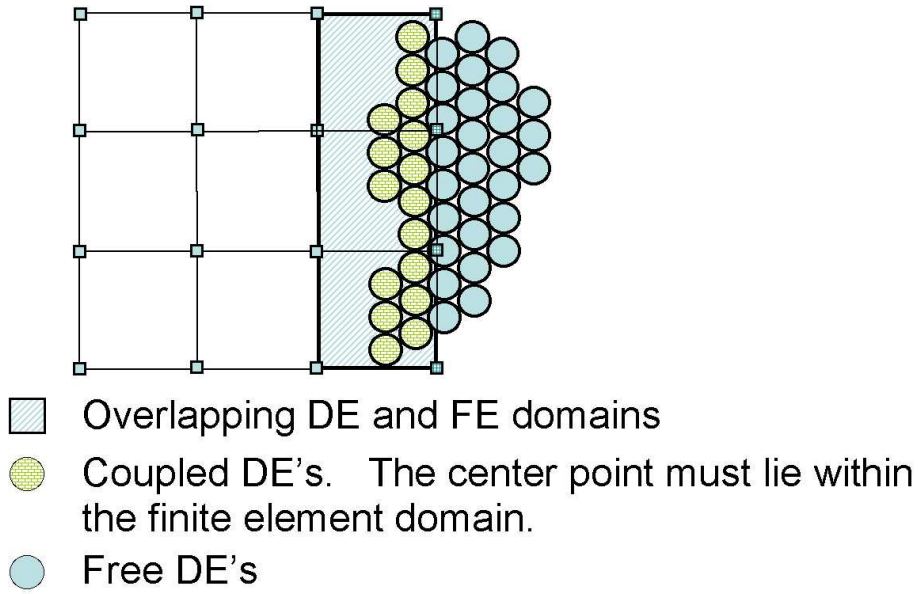

Figure 7.6. Schematic showing the relationship between a DE domain that overlaps a FE domain.

In the overlapping domain, the coupled equilibrium equation, in matrix form, is:

$$\begin{bmatrix} \boldsymbol{K}_{QQ} & \boldsymbol{K}_{QU} \\ \boldsymbol{K}_{UQ} & \boldsymbol{K}_{UU} \end{bmatrix} \begin{Bmatrix} \delta\boldsymbol{Q} \\ \delta\boldsymbol{U} \end{Bmatrix} = \begin{Bmatrix} \boldsymbol{R}_Q \\ \boldsymbol{R}_Q \end{Bmatrix} \tag{7.7}$$

where Q is the domain that includes all of the DEs and U is the domain that includes all of the FE nodes. Here, the symbol $\delta(\bullet)$ is an incremental value within a linearized system of equilibrium equations for solution by iterative algorithm (such as Newton-Raphson). A more thorough treatment of the equilibrium equation can be seen in Zimmerman et al. [3]. The cross terms of the equilibrium equation naturally deals with the coupled influence in the overlap region. In addition, a correction term is also used to account for the double counting of the bond potentials of the DEs in the overlapping domain as well as the bond potentials between DEs in the overlapping domain and DEs outside of the overlapping domain. The force on a node in the overlapping domain is defined by

$$\boldsymbol{f}^{(a)} = \boldsymbol{f}_Q^{(a)} + \boldsymbol{f}_U^{(a)} \tag{7.8}$$

where,

$$\boldsymbol{f}_Q^{(a)} = \boldsymbol{R}_{(i)} \sum N^{(a)} \left(\boldsymbol{X}^{(\beta)} \right) \tag{7.9}$$

is the DE contribution to the nodal forces and

$$\boldsymbol{f}_U^{(a)} = \frac{1}{V_0} \left[\boldsymbol{R} \otimes \boldsymbol{R} \right]_{(i)} \int \rho_{(i)} \frac{\partial N^{(a)}}{\partial \boldsymbol{X}} d\Omega \tag{7.10}$$

is the continuum contribution to the nodal forces with $N^{(a)}$ being the shape functions of the FE evaluated at the DE locations $\boldsymbol{X}^{(\beta)}$, V_0 is the initial element volume, Ω is the volume of the domain, and $\rho_{(i)}$ is the penalty function based on the bond density potential with a range, $0 \leq \rho_{(i)} \leq 1$. A domain with few DEs, few DE bonds, or bonds that are weak with respect to the continuum, would have a $\rho_{(i)}$ that is close to zero.

7.3.2 Macroparticle DE/FE coupling

Another approach to two-way DE/FE coupling is using macroparticles. A macroparticle DEM, grown from seed microparticles, can represent arbitrary polygonal shapes in two dimensions (cf. Figs. 7.7 and 7.8) and arbitrary polyhedral shapes in three dimensions [53]. The interparticle constitutive relations between the microparticles that compose the macroparticle dictate the overall constitutive response of the macroparticle. Such macroparticles could be grown once the continuum bifurcation model and finite element implementation predict fragment dimensions. In essence, the macroparticle composed of microparticles (circles in 2D, and spheres in 3D) would replace the fragments determined by the finite element solution. These macroparticles could then further fragment into sub-macroparticles based on their microparticle interparticle strengths. This could be one approach to a two-way coupled DEM/FEM approach, and potentially more computationally efficient than a two-way approach that would treat each fragment as a discrete element meshed with finite elements, thus relying on the continuum bifurcation model to further fragment a fragment. For the macroparticle approach, choice of seed microparticle size is important, assuming these particle radii are fictitious, i.e. not radii of the inherent microstructural particles that possibly constitute the material (such as sand particles of a sandstone). Also important is treating the contact condition when macroparticles will come into contact with finite elements. Most likely, this contact will be governed by an approach similar to that described in the previous section.

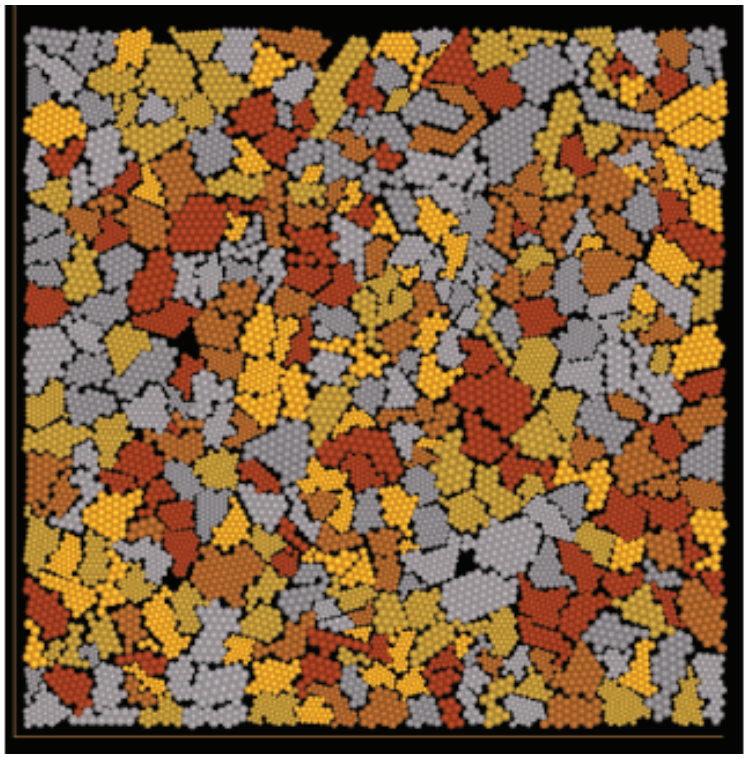

Figure 7.7. Cluster of macroparticles composed of microparticles.

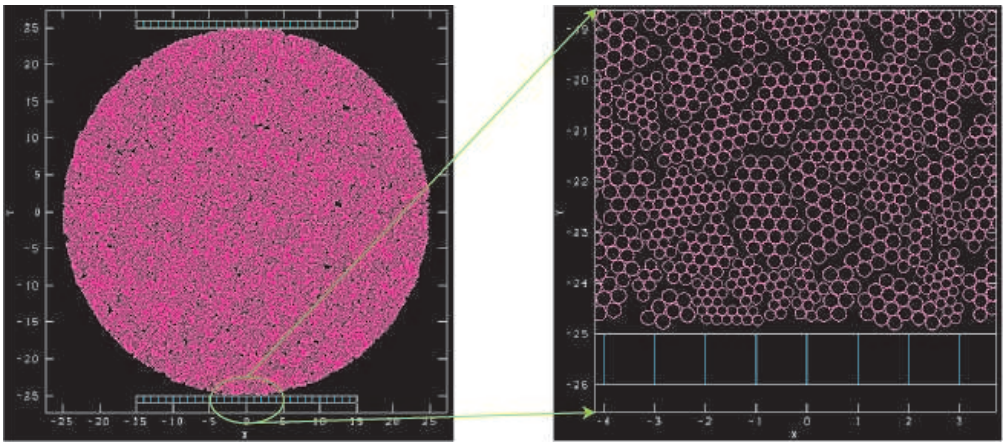

Figure 7.8. Demonstrates the two-dimensional macroparticle algorithm implemented to grow macroparticles from seed microparticles within a 2D shape, a circle.

This page intentionally left blank.

Chapter 8

Conclusions

The project set out to develop a computational modeling capability that could model the transition from continuous to discontinuous deformation in geomaterials, all within a coupled, transient solid-fluid mechanical formulation and 3D finite element implementation, with coupled Discrete Element Method (DEM)/Finite Element Method (FEM) analysis for fragmentation. First, we will summarize briefly what was achieved. The project produced an implicit numerical integration of a simplified version of the Sandia GeoModel [22], a bifurcation analysis of the Sandia GeoModel [49], post-bifurcation geomaterial traction-displacement (cohesive zone) models in Chapt. 4 and implemented using Cohesive Surface Element (CSE) in Chapt. 5 and Embedded Discontinuity Element (EDE) in Chapt. 6, and a strategy for two-way DEM/FEM coupling and implementation of one-way coupling in Chapt. 7. Second, we will summarize briefly what was not achieved. The project did not implement weak discontinuities (jump in strain field), formulate and implement coupled solid-fluid mechanical governing equations with weak and strong discontinuities, nor implement a two-way coupled DEM/FEM capability. Future work is discussed in the next Chapter to address these needs.

The project was successful, however, in outlining and putting into motion a plan to achieve the overall objective as stated in the first sentence of this Chapter. Certain incremental objectives were achieved in the process, giving us confidence that if the overall objective is finally achieved, a unique computational modeling capability will result.

This page intentionally left blank.

Chapter 9

Future work

Some of the original objectives were not achieved in the time frame of the project. Among the more important ones are fully coupled, transient solid-fluid mechanical formulation and 3D finite element implementation with discontinuities, consideration of weak discontinuities (e.g., shear bands), and two-way coupled DEM/FEM, all in three-dimensions. We generate two lists of future work: 1) research that is ongoing and will most likely be achieved without major additional funding, and 2) those research objectives that will require an additional project and appropriate funding to complete.

1. **Near-term research objectives**: "low-hanging fruit"

   (a) **Embedded discontinuity tracing algorithm**: Although more challenging to implement in 3D than in 2D, an initial idea has been formulated, and portions of Tahoe have been identified on which such coding can be based.

   (b) **Locally undrained bifurcation analysis of Sandia Geomodel**: Following [6], we will formulate the Sandia GeoModel for fully-saturated, locally undrained conditions. This means volumetric deformation (elastic and inelastic) is constrained for the constitutive model. An undrained condition implies that the loading is fast enough and the permeability of the material low enough that outflow of pore fluid is restrained [35]. In essence, the pore fluid does not have time to flow out of the pore space, resulting in zero volumetric deformation as the compressibility and dilatancy of the material depends on the ability of the pore volume to change. A globally undrained condition means this condition is applied to the coupled, transient solid-fluid mechanical governing equations, which currently we do not have implemented to account for discontinuities. On the other hand, the locally undrained condition means the volume constraint is applied at a material point at

which the constitutive model governs, thus constraining volumetric deformation for the constitutive model.

(c) Implement the rigid-plastic geomaterial cohesive zone model of Chapt. 5 using Lagrange multipliers rather than a penalty parameter.

2. **Longer-term research objectives**:

(a) **Coupled, transient solid-fluid mechanical governing equations with strong (and/or weak) discontinuities and 3D finite element implementation**: The treatment of discontinuities within a coupled solid-fluid mechanical formulation and the finite element implementation within a three-dimensional setting is an objective that turned out to be beyond the scope of the project. It will be proposed as a future project because the need for such a computational modeling capability still exists.

(b) **Universal bifurcation criterion**: In terms of developing a universal bifurcation criterion for rate-sensitive and insensitive constitutive models, we will investigate the evaluation of cohesive zone yield criteria at various angles at a Gaussian integration point. For rate-sensitive materials, bifurcation to localized deformation is not determined by loss of ellipticity as viscous effects regularize the governing equations (cf. Fig.3.7). Perhaps an embedded cohesive zone yield criterion evaluated at each integration point within a finite element can provide a universal bifurcation criterion for rate-sensitive and insensitive material models. Further thought would need to be given for such a criterion for weak discontinuities. A phenomenological nonlocal or physics-based generalized continuum inelasticity model could serve this role, potentially [71, 10].

(c) **Weak discontinuities and 3D finite element implementation**: It turns out that formulating and implementing hexahedral and tetrahedral finite elements with embedded weak discontinuity leading to mesh independent simulations is a more challenging objective than solely implementing strong discontinuities (which the project ended up doing). The reason for this is that an element would need to account for the weak discontinuity being completely embedded within the element domain, partially embedded, or an element domain falling completely inside the weak discontinuity. This objective is beyond the scope of the project, but will be considered for a future project.

(d) **Simulating defeat of HDBTs and Nuclear Waste Repository failure scenarios**: The eventual goal is to solve, in a mesh-independent manner, these problems of interest to Sandia as described in Chapt. 1. Among solving other geological and geotechnical engineering problems, this goal is of significant interest to the authors and will be pursued as future projects dictate.

Bibliography

[1] A. R. Khoei and A. Bakhshiani and M. Mofid. An implicit algorithm for hypoelasto-plastic and hypoelasto-viscoplastic endochronic theory in finite strain isotropic-kinematic-hardening model. *Int. J. Solids Struct.*, 40:3393–3423, 2003.

[2] F. Armero and K. Garikipati. An analysis of strong discontinuities in multiplicative finite strain plasticity and their relations with the numerical simulation of strain localization in solids. *Int. J. Solids Struct.*, 33:2863–85, 1996.

[3] S. Aubry, D.J. Bamman, J.J. Hoyt, R.E. Jones, C.J. Kimmer, P.A. Klein, G.J. Wagner, E.B. Webb III, and J. Zimmerman. A Robust, Coupled Approach for Atomistic-Continuum Simulation. SAND2004-4778, Sandia National Laboratories, 2004.

[4] T. Belytschko, W. K. Liu, and B. Moran. *Nonlinear Finite Elements for Continua and Structures*. John Wiley & Sons, 2000.

[5] R.I. Borja. Bifurcation of elastoplastic solids to shear band mode at finite strain. *Comp. Meth. App. Mech. Engr.*, 191:5287–5314, 2002.

[6] R.I. Borja. Cam-Clay plasticity. Part V: A mathematical framework for three-phase deformation and strain localization analyses of partially saturated porous media. *Comp. Meth. App. Mech. Engr.*, 193:5301–38, 2004.

[7] R.I. Borja and A. Aydin. Computational modeling of deformation bands in granular media, I: Geological and mathematical framework. *Comp. Meth. App. Mech. Engr.*, 193:2667–98, 2004.

[8] R.I. Borja and R.A. Regueiro. Strain localization in frictional materials exhibiting displacement jumps. *Comp. Meth. App. Mech. Engr.*, 190:2555–80, 2001.

[9] R.I. Borja, K.M. Sama, and P.F. Sanz. On the numerical integration of three-invariant elastoplastic constitutive models. *Comp. Meth. App. Mech. Engr.*, 192:1227–58, 2003.

[10] R. Chambon, D. Caillerie, and C. Tamagnini. A strain space gradient plasticity theory for finite strain. *Comp. Meth. App. Mech. Engr.*, 193(27-29):2797–2826, 1995.

[11] B. D. Coleman and M. E. Gurtin. Thermodynamics with internal state variables. *J. Chem. Phys.*, 47:597–613, 1967.

[12] B. D. Coleman and W. Noll. The thermodynamics of elastic materials with heat conduction and viscosity. *Arch. Ration. Mech. Anal.*, 13:167–178, 1963.

[13] B. Cook and R.P. Jensen. *Discrete Element Methods: Numerical Modeling of Discontinua*. ASCE Geotechnical Special Publication No. 117, Reston, VA, 2002.

[14] R.D. Cook, D.S. Malkus, and M.E. Plesha. *Concepts and Applications of Finite Element Analysis*. John Wiley & Sons, New York, 1989.

[15] P. Cundall and O.D.L. Strack. A discrete numerical model for granular assemblies. *Geotechnique*, 29:47–65, 1979.

[16] J. W. Demmel. *Applied Numerical Linear Algebra*. Society for Industrial and Applied Mathematics, 1997.

[17] A. A. DiGiovanni, J. T. Fredrich, D. J. Holcomb, and W. A. Olsson. Micromechanics of compaction in an analogue reservoir sandstone. In J. Girard, M. Liebman, C. Breeds, and T. Doe, editors, *Pacific Rocks 2000: Rock Around The Rim*, pages 1153–1160. A.A. Balkema, 2000.

[18] G. Duvaut and J.L. Lions. *Les Inequations en Mecanique et en Physique*. Dunod, Paris, 1972.

[19] F. J. Montáns. Implicit multilayer J2-plasticity using Prager's translation rule. *Int. J. Numer. Methods Eng.*, 50:347–375, 2001.

[20] A. F. Fossum and R. M. Brannon. The Sandia Geomodel: Theory and User's Guide. SAND2004-3226, Sandia National Laboratories, 2004.

[21] A. F. Fossum and J. T. Fredrich. Cap plasticity models and compactive and dilatant pre-failure deformation. In J. Girard, M. Liebman, C. Breeds, and T. Doe, editors, *Pacific Rocks 2000: Rock Around The Rim*, pages 1169–1176. A.A. Balkema, 2000.

[22] C.D. Foster, R.A. Regueiro, R.I. Borja, and A.F. Fossum. Implicit integration of a three-invariant, single-surface, isotropic/kinematic hardening, cap plasticity model for geomaterials. *Comp. Meth. App. Mech. Engr.*, 194:5109–5138, 2005.

[23] D. J. Frew, M. J. Forrestal, and W. Chen. A split Hopkinson pressure bar technique to determine compressive stress-strain data for rock materials. *Exp. Mech.*, 41:40–46, 2001.

[24] G.I. Barenblatt. Equilibrium cracks formed during brittle fracture. *Prikl. Mat. Mekh.*, 23(5):1273–1282, 1959.

[25] R. Hill. Acceleration waves in solids. *J. Mech. Phys. Solids*, 10:1–16, 1962.

[26] D. J. Holcomb and J.W.Rudnicki. Inelastic constitutive properties and shear localization in Tennessee marble. *Int. J. Numer. Anal. Methods Geomech.*, 25:109–129, 2001.

[27] T. J. R. Hughes. *The Finite Element Method*. Prentice-Hall: New Jersey, 1987.

[28] I. Doghri. Fully implicit integration and consistent tangent modulus in elasto-plasticity. *Int. J. Numer. Methods Eng.*, 36:3915–3932, 1993.

[29] J. P. G. Sawyer and C. H. Wang and R. Jones. An implicit algorithm using explicit correctors for the kinematic hardening model with multiple back stresses. *Int. J. Numer. Methods Eng.*, 50:2093–2107, 2001.

[30] J.E. Marsden and T.J.R. Hughes. *Mathematical Foundations of Elasticity*. Dover, 1994.

[31] P. A. Klein, J. W. Foulk, E. P. Chen, S. A. Wimmer, and H. J. Gao. Physics-based modeling of brittle fracture: cohesive formulations and the application of meshfree methods. *Theor. Appl. Fract. Mech.*, 37:99–166, 2001.

[32] P.A. Klein, S.X. McFadden, D.J. Bammann, Y. Hammi, J.W. Foulk, and B.R. Antoun. A mechnism-based approach to modeling ductile fracture. SAND2003-8804, Sandia National Laboratories, 2003.

[33] L. Mähler and M. Ekh and K. Runesson. A class of thermo-hyperelastic-viscoplastic models for porous materials: theory and numerics. *Int. J. Plast.*, 17:943–969, 2001.

[34] L. X. Luccioni and J. M. Pestana and R. L. Taylor. Finite element implementation of non-linear elastoplastic constitutive laws using local and global explicit algorithms with automatic error control. *Int. J. Numer. Methods Eng.*, 50:1191–1212, 2001.

[35] T.W. Lambe and R.V. Whitman. *Soil Mechanics*. Wiley, New York, 1969.

[36] M. Kobayashi and N. Ohno. Implementation of cyclic plasticity models based on a general form of kinematic hardening. *Int. J. Numer. Methods Eng.*, 53:2217–2238, 2002.

[37] M. Rouainia and D. Muir Wood. Implicit numerical integration for a kinematic hardening soil plasticity model. *Int. J. Numer. Anal. Methods Geomech.*, 25:1305–1325, 2001.

[38] M. T. Manzari and R. Prachathananukit. On integration of a cyclic soil plasticity model. *Int. J. Numer. Anal. Methods Geomech.*, 25:525–549, 2001.

[39] M.T. Manzari and R.A. Regueiro. Gradient plasticity modeling of geomaterials in a meshfree environment. Part I: Theory and variational formulation. *Mech. Res. Commun.*, 32:536–46, 2005.

[40] N. Moes, A. Gravouiland, and T. Belytschko. Non-planar 3D crack growth by the extended finite element and level setsPart I: Mechanical model. *Int. J. Numer. Methods Eng.*, 53:2549–68, 2002.

[41] A. Needleman. Material rate dependence and mesh sensitivity in localization problems. *Comp. Meth. App. Mech. Engr.*, 67:69–85, 1988.

[42] R. W. Ogden. *Nonlinear Elastic Deformations*. Chicheste, Ellis Horwood, 1984.

[43] M. Ortiz, I. Leroy, and A. Needleman. A finite element method for localized failure analysis. *Comp. Meth. App. Mech. Engr.*, 61:189–214, 1987.

[44] P. E. Senseny and A. F. Fossum and T. W. Pfeifle. Non-associative constitutive laws for low porosity rocks. *Int. J. Numer. Anal. Methods Geomech.*, 7:101–115, 1983.

[45] D. Potyondy and P. Cundall. A bonded-particle model for rock. *Int. J. Rock Mech. Min. Sci.*, 41:1329–64, 2004.

[46] D.S. Preece, B.J. Thorne, M.R. Baer, and J.W. Swegle. Computer Simulation of Rock Blasting: A Summary of Work from 1987 through 1993. SAND94-1027, Sandia National Laboratories, 1994.

[47] R. A. Regueiro and R. I. Borja. Plane strain finite element analysis of pressure sensitive plasticity with strong discontinuity. *Int. J. Solids Struct.*, 38:3647–72, 2001.

[48] R.A. Regueiro, C.D. Foster, and R.I. Borja. Three dimensional modeling of slip surfaces in geomaterials. In *Proceedings of 15th ASCE Engineering Mechanics Conference*, 2002.

[49] R.A. Regueiro, C.D. Foster, A.F. Fossum, and R.I. Borja. Bifurcation analysis of a three-invariant, isotropic/kinematic hardening cap plasticity model for geomaterials. In *ARMA/NARMS 04-520*, 2004.

[50] J.R. Rice and J.W. Rudnicki. A note on some features of the theory of localization of deformation. *Int. J. Solids Struct.*, 16:597–605, 1980.

[51] J.W. Rudnicki and J.R. Rice. Conditions for the localization of deformation in pressure-sensitive dilatant materials. *J. Mech. Phys. Solids*, 23:371–394, 1975.

[52] S. Hartmann and G. Lührs and P. Haupt. An efficient stress algorithm with applications in viscoplasticity and plasticity. *Int. J. Numer. Methods Eng.*, 40:991–1013, 1997.

[53] H. Sakaguchi and H.-B. Muhlhaus. Meshfree modelling of failure and localization in brittle materials. In A. Asaoka, T. Adachi, and F. Oka, editors, *Deformation and Progressive Failure in Geomechanics*, pages 15–21. Pergamon, 1997.

[54] I. S. Sandler, F. L. DiMaggio, and G. Y. Baldi. Generalized cap model for geological materials. *J. Geotech. Eng. Div ASCE*, 103(12):1461, 1977.

[55] I. S. Sandler and D. Rubin. An algorithm and a modular subroutine for the CAP model. *Int. J. Numer. Anal. Methods Geomech.*, 3(2):173–186, 1979.

[56] I.S. Sandler and J.P. Wright. Strain-softening. In S. Nemat-Nasser et al., editor, *Theoretical Foundations for Large Scale Computations of Nonlinear Material Behavior*, pages 285–315. Martinus Nijhoff Pub., The Netherlands, 1976.

[57] L.A. Schoof and V.R. Yarberry. EXODUS II: A Finite Element Data Model. SAND92-2137, Sandia National Laboratories, 1992.

[58] J. C. Simo. Algorithms for static and dynamic multiplicative plasticity that preserve the classical return mapping schemes of the infinitesmal theory. *Comp. Meth. App. Mech. Engr.*, 99:61–112, 1992.

[59] J. C. Simo. Numerical Analysis and Simulation of Plasticity. In P.G. Ciarlet and J.L. Lions, editors, *Handbook of Numerical Analysis*. Elsevier Science, 1998.

[60] J. C. Simo and T. J. R. Hughes. *Computational Inelasticity*. Prentice-Hall: New York, 1998.

[61] J.C. Simo and A. Armero. Geometrically non-linear enhanced strain mixed methods and the method of incompatible modes. *Int. J. Numer. Methods Eng.*, 33:1413–49, 1992.

[62] J.C. Simo, Oliver, and F. Armero. An analysis of strong discontinuities induced by strain-softening in rate-independent inelastic solids. *Comput. Mech.*, 12:277–296, 1993.

[63] J.C. Simo and J. Oliver. A new approach to the analysis and simulation of strain softening in solids. In Z.P. Bažant et al., editor, *Fracture and Damage in Quasibrittle Structures*, pages 25–39. E&FN Spon, 1994.

[64] J.C. Simo and M.S. Rifai. A class of mixed assumed strain methods and the method of incompatible modes. *Int. J. Numer. Methods Eng.*, 29:1595–1638, 1990.

[65] L.J. Sluys and R. de Borst. Wave propagation and localization in a rate-dependent cracked medium: Model formulation and one-dimensional examples. *Int. J. Solids Struct.*, 29:2945–58, 1992.

[66] C. Tamagnini, R. Castellanza, and R. Nova. A Generalized Backward Euler algorithm for the numerical integration of an isotropic hardening elastoplastic model for mechanical and chemical degradation of bonded geomaterials. *Int. J. Numer. Anal. Methods Geomech.*, 26(10):963–1004, 2002.

[67] R.L. Taylor, J.C. Simo, O.C. Zienkiewicz, and A.C.H. Chan. Patch test - A condition for assessing FEM convergence. *Int. J. Numer. Methods Eng.*, 22:39–62, 1986.

[68] S.P. Timoshenko and J.N. Goodier. *Theory of Elasticity, 3rd Edition*. McGraw-Hill, New York, 1970.

[69] I. Vardoulakis and M. Goldschieder. Biaxial apparatus for testing shear bands in soils. In *Soil Mechanics and Foundation Engineering*, pages 819–824. A.A. Balkema, 1981.

[70] I. Vardoulakis, M. Goldschieder, and G. Gudehus. Formation of shear bands in sand bodies as a bifurcation problem. *Int. J. Numer. Anal. Methods Geomech.*, 2:99–128, 1978.

[71] I. Vardoulakis and J. Sulem. *Bifurcation analysis in geomechanics*. Blackie, London, 1995.

Chapter 10

DISTRIBUTION:

3	Prof. R.I. Borja Department of Civil and Environmental Engineering Terman Engineering Center M42 Stanford University Stanford, California 94305-4020
3	Mr. C.D. Foster Department of Civil and Environmental Engineering Terman Engineering Center M42 Stanford University Stanford, California 94305-4020
3	Prof. M.T. Manzari Department of Civil and Environmental Engineering Phillips Hall, Room 643 The Academic Center 801 22nd Street, NW Washington, DC 20052
10	Prof. R.A. Regueiro Department of Civil, Environmental, and Architectural Engineering 1111 Engineering Dr. 428 UCB, ECOT 441 Boulder, CO 80309-0428

1		Dr. P.A. Klein 1149 Munich Street San Francisco, CA 94112
1	MS 0123	D.L. Chavez, 1011
1	MS 0384	H.S. Morgan, 1540
1	MS 0825	C.W. Peterson, 1500
1	MS 0825	W.L. Hermina, 9110
1	MS 0701	P.B. Davies, 6100
1		J.A. Merson,
1	MS 0372	J.E. Bishop, 1527
1	MS 0325	D.J. Frew, 2615
1	MS 1160	V.K. Luk, 5431
1		D.A. Dederman, 5431
1	MS 0847	P.J. Wilson, 1520
1	MS 0370	M.E. Kipp, 1431
1	MS 0378	R.J. Mackinnon, 1431
1		S.J. Petney, 1431
1		R.M. Summers, 1431
1	MS 0750	J.T. Fredrich,
1	MS 0751	T.W. Pfeifle, 6117
1		R.M. Brannon, 6117
1		L.S. Costin,
5		A.F. Fossum, 6117
1		D.J. Holcomb, 6117
5		R.P. Jensen, 6117
1		W.A. Olsson, 6117
1		O.E. Strack, 6117

1	MS 0372	J. Jung,
1		J.T. Ostein,
1	MS 0376	C.M. Stone,
1		J.G. Arguello,
1	MS 0378	P.A. Taylor,
1	MS 0380	A.S. Gullerud,
1		S.W. Key,
1	MS 1156	D.S. Preece,
1	MS 0748	S.P. Burns,
1	MS 0139	P. Yarrington,
1	MS 0893	J. Pott, 9123
1		J.V. Cox, 9123
1		E.D. Reedy, 9123
1		W.M. Scherzinger, 9123
1	MS 9001	M.E. John, 8000 Attn: Director, 8100 Director, 8200 Director, 8300 Director, 8900
1	MS 9409	P.A. Spence, 8774
1		G.J. Wagner, 8752
1	MS 9042	E.P. Chen, 8763
1		D.J. Bammann, 8763
1		A.A. Brown, 8763
1		M.L. Chiesa, 8774
1		J. Crowell, 8774
1		J. Dike, 8774
1		M. Jew, 8774
1		R.E. Jones, 8763
1		C.J. Kimmer, 8763
1		D.M. Kwon, 8774

1		Y. Ohashi, 8774
1		A. Ortega,
1		J.A. Zimmerman, 8763
1	MS 9405	S. Aubry, 8763
1		J.W. Foulk, 8763
1		T.D. Nguyen, 8763
1		E.B. Marin, 8763
1	MS 9161	W.R. Even Jr., 8760
1	MS 9405	K.L. Wilson, 8700
		Attn:
		G.D. Kubiak, 8750, MS 9404
		J.E.M. Goldsmith, 8751, MS 9401
		C.D. Moen, 8752, MS 9409
		G.F. Cardinale, 8753, MS 9401
		J.C.F. Wang, 8773, MS 9403
1	MS 0899	Technical Library, 9616
3	MS 9018	Central Technical Files, 8945-1
1	MS 9021	Classification Office, 8511